COMPLEX ALIGNMENT MECHANISM AND LIFETIMES OF HIGH SPIN STATES IN ^{172}Os AND ^{173}Os

BY
ARI VIRTANEN

Academic Dissertation
for the Degree of
Doctor of Philosophy

Jyväskylä, Finland
December 1989

COMPLEX ALIGNMENT MECHANISM AND LIFETIMES OF HIGH SPIN STATES IN ^{172}Os AND ^{173}Os

BY
ARI VIRTANEN

Academic Dissertation
for the Degree of
Doctor of Philosophy

To be presented, by permission of the
Faculty of Mathematics and Natural Sciences
of the University of Jyväskylä,
for public examination in Auditorium S-212 of the
University of Jyväskylä on December 16, 1989,
at 12 o'clock noon

Jyväskylä, Finland
December 1989

Preface

This work has been carried out during the years 1987-1989 at the Oak Ridge National Laboratory (Oak Ridge, USA) and at the University of Jyväskylä. I wish to express my gratitude to these institutes for providing an excellent working conditions in an inspiring and free athmosphere.

My special thanks go to my supervisors Professor Jorma Hattula and Dr. Noah Johnson, for having time to deal with me and for offering the position of a research assistant. Thanks should indeed go to all my colleagues and friends in the Nuclear Structure Group at ORNL and in the Gamma Group at JYFL for their continuous encouragement along the way to the goal. Among many people whom I am indebted to, my warmest thanks go to Dr. Mark Riley not only for his patient guidance at the laboratory during my stay in USA, but also for offering help when needed away from the office. I would also like to say thank you to Dr. Tom Lönnroth for his valuable comments on the text and on the lay-out during the thesis writing.

The financial support from the Academy of Finland is greatly acknowledged.

Finally, I wish to thank my wife Raija and my son Antti for their unreserved support and patience. To them, I dedicate this thesis.

Jyväskylä, November 1989

Ari Virtanen

Abstract

High spin states in ^{172}Os and ^{173}Os have been investigated by $\gamma - \gamma$ coincidence studies. States were populated by the $^{144}Nd(^{32}S, 4n/3n)$ reactions using 162-MeV ^{32}S ions from the HHIRF tandem accelerator at ORNL. For the spectroscopy study, measurements were made with the Oak Ridge Compton Suppression Spectrometer System incorporated into the Spin Spectrometer. The yrast band in ^{172}Os was observed up through the 30^+ state and four new side bands were deduced. A band identified as belonging to the previously unknown ^{173}Os was also observed. Results were interpreted using average nuclear field calculations which incorporated the deformed Woods-Saxon potential with its "universal" parameterization, a cranking approximation and the Hartree-Fock-Bogolyubov method. A semiquantitative agreement with experiment to explain e.g. the low-frequency anomaly seen in ^{172}Os was obtained. Lifetimes of high spin states in ^{172}Os were measured by the recoil distance technique. The $\gamma - \gamma$ coincidences at 20 different target-stopper distances were recorded between six germanium detectors at 90^0 to the beam direction and a Compton-suppressed Ge detector at 0^0 to record the shifted and unshifted γ-ray peaks. Coincidences allowed the use of versatile gating procedures in the analysis. The extracted lifetimes and quadrupole moments were found to support the conclusions based on the spectroscopical and theoretical studies.

Contents

List of Figures

v

List of Tables

Chapter 1

Introduction

The region of the light platinum, osmium and tungsten nuclei has lately become a region stimulating much activity, both in experimental and theoretical investigations. Recent developments in nuclear structure have brought a considerable focussing on the problems of shape evolution and shape coexistence phenomena. Current emphasis is not only on the geometrical shapes in terms of various forms of the nuclear surface, but maybe more importantly, with an understanding of the underlying microscopic forces from the different single-particle configurations which influence in a dramatical way, the changes in nuclear global properties. One of the reasons centers around a basic prediction[1][2] of the cranked shell model (CSM) which indicates that when the Fermi surface is raised to the middle of the $i_{13/2}$ neutron shell, the triaxial deformation-driving effects of the quasineutrons is toward the collective asymmetry sector $(-\gamma)$. The implication is that the collectivity in the s band, following the rotation alignment of a pair of $i_{13/2}$ neutrons, should remain rather similar to that of the ground band.

Previous spectroscopic studies[3][4] had defined the yrast sequence up to $I = 24^+$, but they provided only very limited information on side bands. Moreover, the yrast sequence of ^{172}Os contains features which provided an additional stimulus for the $\gamma - \gamma$ coincidence measurement of a good statistical quality. Both Durell et al.[3] and Wells et al.[4] reported two anomalies in the yrast sequence moment of inertia below a rotational frequency of $\hbar\omega = 0.27$ MeV. The first of these anomalies occurs at unusually low spin, $I = 8^+$, and at a rotational frequency $\hbar\omega = 0.24$ MeV; the second occurs at $I = 16^+$ and $\hbar\omega = 0.27$ MeV.

1

Oshima et al.[5] and Fewell et al.[6] have carried out lifetime measurements on ytterbium and erbium nuclei, the Fermi surfaces of which lie near the bottom of the shell ($N \sim 90$), and found a rotational-frequency-dependent loss of collectivity in the s band. This feature is consistent with the CSM prediction that these low-Ω quasineutrons drive the prolate shape to one with positive γ deformation corresponding to the less collective structure. The nucleus ^{172}Os with $N = 96$ appeared to be a good case on which to perform lifetime measurements as a further test of these CSM predictions near the middle of the $i_{13/2}$ neutron shell.

The suggestion[3] that a coexistence picture may be applicable to ^{172}Os with a significant jump in deformation at $I = 8^+$, similar to that seen in ^{176}Pt at low spins[7][8], was investigated by Wells et al.[4] through the self-consistent cranked shell-model calculations. However, only a smooth increase of $\Delta\beta_2 = 0.02$ with increasing frequency for the ground configurations was predicted.

Wells et al.[4] explored the possibility that this anomaly at $I = 8^+$ arose from an additional band crossing, a situation consistent with the behaviour of the dynamical moment of inertia, $\mathcal{J}^{(2)}$. Specifically, the possibility that an early alignment of $h_{9/2}[541]1/2$ protons may be contributing was considered. This seemed implausible, however, since the cranking calculations predicted such alignment to occur at much higher frequency, $\hbar\omega = 0.45$ MeV. Interestingly, they[4] were able to produce a very good theoretical fit to the discontinuities in the $\mathcal{J}^{(2)}$ plot through a phenomenological three-band-mixing calculation. In this calculation, the unperturbed second and third bands were assumed to contain 4 and 12 units of intrinsic angular momentum, respectively, these being the same values used[9] in the analysis of ^{172}W, where the possibility of simultaneous alignment of $h_{9/2}$ protons and $i_{13/2}$ neutrons was considered. Recently, Dracoulis et al.[10] also carried out three-band-mixing calculations on ^{172}Os, as well as on ^{170}Os, and concluded that the behavior of the total aligned angular momentum could be fit by invoking the presence of "intruder" band heads at 600 and 1200 keV, respectively.

Interestingly, Hsieh et al.[12] have recently carried out calculations using an IBA plus two quasiparticle modell where they considered the $i_{13/2}$ neutron and $h_{9/2}$ proton orbitals. They applied these to the even osmium nuclei from mass 172 to 180 and concluded that it was necessary to invoke major contributions from the $h_{9/2}$ protons to explain the behaviour in the yrast sequence of ^{172}Os.

Since the works mentioned above have left many interesting and unanswered questions about ^{172}Os, a reinvestigation of the level properties of this nucleus has been done in this thesis. Here, the Compton-suppressed γ-

ray measurements of high statistical quality with the Compton Suppression System (19 suppressed Ge detectors) combined with the Spin Spectrometer are carried out. These measurements have provided new details on the yrast sequence of ^{172}Os and have enabled the construction of four side bands and have offered some information on the previously unstudied nucleus, ^{173}Os.

Further, these new spectroscopy results have appeared to be very valuable in proper analysis of the lifetime experiment, which was done for the ^{172}Os and will be discussed thoroughly in this work. Together with the relative binding energies the measurement of the transition matrix elements extracted from these measured lifetimes are a sensitive indicator of the collective aspects of the wave functions of the states and, thus, provides a key information on the evolving collectivity of ^{172}Os as a function of spin and rotational frequency.

Many methods of measuring lifetimes have been developed since the range of lifetimes of bound levels is extremely broad. In this thesis a Doppler-shift recoil-distance method used for determining lifetimes in the range from below one picosecond to tens of nanoseconds is described. A particularly significant stage in the evolution of Doppler-shift techniques was the development of the high resolution germanium detectors. Progress has been rapid, and good commercially produced detectors now have an efficiency of up to 70% of a $7.5 \times 7.5 cm^2$ NaI crystal and a resolution of about 0.2% (corresponding to 3 keV) for 1.5 MeV γ-ray. Also, the development of accelerators offering a variety of energetic heavy-ion beams as well as enhanced data analysis capabilities with the coincidence technique enabled this method to achieve its present prominence.

Many recoil-distance lifetime measurements have been carried out following heavy-ion Coulomb excitation. The analysis of such data, especially for deformed nuclei where the lifetime of a member in the band, according to the increasing transition energy, very often is shorter than that of the state below it, is accomplished in a relatively simple manner. This is not the case for the data of the compound nucleus reaction. Here the problem is complicated by the fact that a given level often has appreciable side feeding from unobserved transitions from the γ-ray continuum. This can cause ambiguities in the solutions of the equations describing the decay chain. In this thesis a computer program which handles these complexities is described. Also, the program includes an option of making some corrections to the data. These consist of corrections for position- and velocity dependent changes in the solid angle, for the effect of attenuation of alignment and for changes in the line shapes caused by the slowing down effect.

Although this work is monographic, details and results are partly reported in the following papers:

1   J.C. Wells, N.R. Johnson, C. Baktash, I.Y. Lee, F.K. McGowan, M.A. Riley, A. Virtanen and J. Dudek, *High-Spin Studies of* $^{172,173}Os$*: Complex Alignment Mechanism*, Phys. Rev. **C40** (1989) 725
     https://doi.org/10.1103/PhysRevC.40.725

2   A. Virtanen, M.A. Riley, N.R. Johnson, F.K. McGowan, I.Y. Lee, C. Baktash, J. Dudek, J.Y. Zhang, F. Dönau and J.C. Wells, *Lifetimes of High-Spin States in* ^{172}Os, to be published

3   J.C. Wells, A. Virtanen, N.R. Johnson, M. Riley, F.K. McGowan, C. Baktash and I.Y. Lee, *Gamma-Ray Measurements on the High-Spin States of* ^{172}Os, ORNL Physics Division Progress Report (1987) 84

4   J.C. Wells, N.R. Johnson, M.A. Riley, J. Dudek, A. Virtanen, F.K. McGowan, C. Baktash and I.Y. Lee, *High-Spin Studies of* ^{172}Os*: Complex Alignment Mechanism*, ORNL Physics Division Progress Report (1988) 62

5   A. Virtanen, N.R. Johnson, F.K. McGowan, M.A. Riley, I.Y. Lee, C. Baktash, J. Dudek and J.C. Wells, *Investigation of the Evolution of Collectivity in* ^{172}Os *Via Lifetime Measurements*, ORNL Physics Division Progress Report (1988) 65

6   J.C. Wells, N.R. Johnson, A. Virtanen, M.A. Riley, C. Baktash, I.Y. Lee and F.K. McGowan, *Gamma-Ray Measurements on High-Spin States of* ^{172}Os, Bull. Am. Phys. Soc. **33** (1988) 981

7   A. Virtanen, N.R. Johnson, C. Baktash, I.Y. Lee, F.K. McGowan, M.A. Riley, J.C. Wells and J. Dudek, *Lifetimes of High-Spin States in* ^{172}Os, Bull. Am. Phys. Soc. **33** (1988) 1585

Chapter 2

Theory

2.1 Rotations in Deformed Nuclei

2.1.1 Energy Systematics Along the Yrast Line

High spins in nuclei are caused by collective rotations (and/or vibrations) of the nucleus as a whole, by aligning of one or more nucleonic angular momenta or by combining these mechanisms.

Classically, the frequency of an axially symmetric nucleus rotating around the "1"- axis in (X_1, X_2, X_3) coordinates is defined as[1]

$$\omega(I) = \frac{dE_{rot}}{dI_1} \tag{2.1}$$

The rotational energy is

$$E_{rot}(I) = \frac{J^2}{2\mathcal{J}} = \frac{1}{2\mathcal{J}}I(I+1), \tag{2.2}$$

where $\mathcal{J}$ is the moment of inertia and is found to be $\sim 50\%$ of the rigid body value for a real nucleus. Eq. (2.2) defines a rotational band built on the ground state (g-band) of an even-even nucleus, where the nucleons with an angular momentum i fill each orbit with $\pm i$ in pairs, i.e. they are "paired". Because of the invariance with respect to a rotation of π the $I =$odd-values vanish and the spin difference between successive levels within the band is 2 units of angular momentum. Hence, from eq. (2.1), $dE_{rot} = E_\gamma$ and $dI = 2$, which gives $\omega = E_\gamma/2$. Also, the transition energy E_γ between

---

[1] Within this chapter the unit $\hbar = 1$ is used

these successive in-band transitions, from eq. (2.2), is

$$E_\gamma = \frac{1}{\mathcal{J}}(2I - 1), \tag{2.3}$$

which would be seen as a series of equally spaced peaks in a γ-ray spectrum in the case of a constant $\mathcal{J}$.

However, a band built on an aligned two-particle configuration (band head) may cross the g-band and becomes favoured at a critical bandcrossing (backbending) frequency, ω_c. The stretched electric quadrupole transitions of this "s-band" form the yrast sequence, which have transition strengths enhanced by about 100-200 times relative to that for a single-particle transitions. This important property quarantees that once excited into a particular band, the nucleus will normally de-excite by a series of in-band transitions and only begins to decay out-of-band into another configurations near the band head.

At still higher frequencies the s-band can be crossed by a four-quasiparticle configuration built on two pairs of aligned particles. This band structure may be observed until a shape transition "from prolate to oblate" configuration occurs and an irregular single-particle like pattern appears. This results in a very irregular yrast line with transitions of both quadrupole and dipole type and transition strength close to the single particle estimates.

2.1.2 Nuclear Moments of Inertia

From the kinematics of its constituents (mass m_i, position r_i) the angular momentum of a rigid body, rotating about one of its principal axis of inertia, is defined by $I = (\Sigma m_i r_i^2)\omega = \mathcal{J}\omega$. According to this and to eq. (2.1) with $I = I_1$ the nuclear moment of inertia is defined as:

$$\mathcal{J}^{(1)} = \frac{I}{\omega} = I(\frac{dE}{dI})^{-1}, \tag{2.4}$$

and, due to the analogy, is called the "kinematical moment of inertia". The superscript "(1)" comes from the first derivative of E with respect to I.

In addition to this, another quantity related to the second derivative of E vs. I is derived and is termed as the "dynamical moment of inertia":

$$\mathcal{J}^{(2)} = \frac{dI}{d\omega} = (\frac{d^2E}{dI^2})^{-1}. \tag{2.5}$$

In contrast to $\mathcal{J}^{(1)}$, the $\mathcal{J}^{(2)}$ is not directly related to the nuclear inertia, but reflects critical, "dynamical" changes in the rotational spectrum.

From their definitions it is easy to calculate the following differential relation between $\mathcal{J}^{(1)}$ and $\mathcal{J}^{(2)}$:

$$\mathcal{J}^{(2)} = \frac{dI}{d\omega} = \frac{d}{d\omega}(\omega\mathcal{J}^{(1)}) = \mathcal{J}^{(1)} + \omega\frac{d\mathcal{J}^{(1)}}{d\omega}. \qquad (2.6)$$

One notes that, at the limit of $\omega \to 0$; $\mathcal{J}^{(1)} = \mathcal{J}^{(2)}$. The increasing rotation is likely to damage the pairing because of the presence of Coriolis and centrifugal forces, the effect called "Coriolis Anti Pairing" (CAP): At very high ω the pairing totally disappears and the moment of inertia approaches the rigid body value $\mathcal{J}_{rig}$. At $\mathcal{J}^{(1)} \sim \mathcal{J}_{rig}$ the $d\mathcal{J}^{(1)} \sim 0$ in (2.6) and, again; $\mathcal{J}^{(1)} = \mathcal{J}^{(2)}$.

In the analysis we are, in fact, interested in the relative quantities and the ground state of an even-even nucleus is a natural choise for the reference. This is accomplished by systematically fitting e.g. the kinematical moment of inertia of the low-spin members of the ground state band to the Harris' formula[13]

$$\mathcal{J}_{ref}^{(1)} = \mathcal{J}_0^{(1)} + \mathcal{J}_1^{(1)}\omega^2, \qquad (2.7)$$

which makes it equivalent to the VMI model (the Variable Moment of Inertia model[14]). The constants $\mathcal{J}_0^{(1)}$ and $\mathcal{J}_1^{(1)}$ have to be adjusted for each nucleus separately.

An application to the dynamical moment of inertia is obvious (eq. (2.6)):

$$\mathcal{J}_{ref}^{(2)} = \mathcal{J}_0^{(2)} + 3\mathcal{J}_1^{(2)}\omega^2, \qquad (2.8)$$

and can be used as an s-band reference, c.f. Bengtsson et al.[15].

2.1.3   Transformation into the Rotating Frame

For simplicity, the body-fixed coordinates are generally used in theoretical investigations. The transformation of the Hamiltonian from the laboratory (X) to the rotating (X') coordinate system by using a classical treatment is given in *Appendix A*. Quantum mechanically, it can be done by means of the rotation operator $\mathcal{R}(\omega t) = exp(-i\omega t\hat{I}_1)$, where $\hat{I}_1$ denotes the projection of the angular momentum operator on the rotation axis "1". The original time-dependent Schrödinger equation in X is written as

$$i\frac{\partial\Psi}{\partial t} = H\Psi. \qquad (2.9)$$

The wave function Ψ and the Hamiltonian H can be expressed in terms of the body-fixed coordinates as

$$\Psi = \mathcal{R}(\omega t)\Psi' \qquad (2.10)$$

and

$$H = \mathcal{R}(\omega t)H'\mathcal{R}(\omega t)^{-1}, \tag{2.11}$$

respectively. Inserting (2.10) and (2.11) into eq. (2.9) and computing the time derivative yields

$$i\frac{\partial \Psi'}{\partial t} = (H' - \omega \hat{I}_1)\Psi', \tag{2.12}$$

which is exactly the same result as obtained in *Appendix A*, the second term on the right hand side being in analogy to the Coriolis and centrifugal forces in classical mechanics. The term $H^\omega = H' - \omega\hat{I}_1$ is called cranking Hamiltonian.

The nuclear potential in H' is fixed in the rotating frame and thus does not depend on time. Therefore one can separate time dependence in Ψ' assuming a trivial, stationary form:

$$\Psi'(\mathbf{r'}, t) = exp(-iE^\omega t)\Psi'(\mathbf{r'}). \tag{2.13}$$

Inserting this into the eq. (2.12) we obtain the so called time independent cranking equation

$$[H' - \omega\hat{I}_1]\Psi'(\mathbf{r'}) = E^\omega\Psi'(\mathbf{r'}), \tag{2.14}$$

where

$$E^\omega = E' - \omega\hat{I}_1. \tag{2.15}$$

2.2 Single Particle States in Deformed Nuclei

To avoid the complexity of a many-nucleon problem it is assumed that all the nucleons contribute to create an average field which acts independently on the individual nucleons. This is known as the Independent Particle Model (IPM) and is used in theoretical treatments here. However, since the nucleon-nucleon force is such a strong (though short range) force, one might expect residual two-body forces to play some type of role in the one-body potential approximation. One such residual force is the pairing force which will be discussed in subsection 2.2.3.

2.2.1 The Nilsson Model

In calculations of the single particle energy levels Nilsson[16] (in 1955) and later Nilsson et al.[17] (in 1969) used the deformed oscillator potential:

$$V_{osc} = \frac{1}{2}M[\omega_\perp^2(x_1^2 + x_2^2) + \omega_3^2 x_3^2], \tag{2.16}$$

where the quadrupole deformation parameter ϵ is introduced by

$$\omega_3 = \omega_0(\epsilon)(1 - \frac{2}{3}\epsilon) \tag{2.17}$$

and

$$\omega_\perp = \omega_0(\epsilon)(1 + \frac{1}{3}\epsilon). \tag{2.18}$$

Axial symmetry is assured by setting $\omega_1 = \omega_2 = \omega_\perp$. The oscillator frequency ω_0 is often given by

$$\omega_0 = 41 \times A^{-\frac{1}{3}} MeV. \tag{2.19}$$

Moreover, this is sometimes multiplied by $[1 \pm (N - Z)/3A]$ with the plus sign for neutrons and the minus sign for protons.

The single-particle Hamiltonian is written as

$$h_{Nilsson} = -\frac{\nabla^2}{2m} + V_{osc} + C\mathbf{l} \cdot \mathbf{s} + D\mathbf{l}^2. \tag{2.20}$$

In order to reproduce the right magic numbers the strong spin-orbit term $\mathbf{l} \cdot \mathbf{s}$ is added, the quantity C giving the strength of the force. The last term (velocity-dependent term) is to make the nucleonic potential more flat inside the nucleus and more attractive at the surface (i.e. more "square-like"), thereby lowering the energies of the high l-states (D is negative). This effects heavier nuclei more, since they have a higher concentration of high l- (or j-) orbitals near the Fermi surface.

The constants C and D are chosen such a way that the known shell model ordering for zero deformation is obtained. Usually, they are parameterized in the form:

$$C = -2\kappa\omega_0 \tag{2.21}$$

and

$$D = -\kappa\mu\omega_0. \tag{2.22}$$

To get a good fit, different values of the parameters κ and μ for different shells are used, but depend on the nucleus (Z,N) one is interested in. Because of these "modifications" the effective potential is called "Modified Oscillator (MO) potential" or "Nilsson potential".

The single-particle spectra of energy eigenvalues e (usually in units of ω_0) of the Hamiltonian (2.20) are referred to as "Nilsson diagrams": Associated with each level are the quantum numbers N, n_3, Λ and Ω used with the notation $[Nn_3\Lambda]\Omega^\pi$. The π is parity (often omitted as redundant; $\pi = (-1)^l = (-1)^N$), the N is the principle quantum number and n_3 is its

component on the symmetry axis. The Ω and Λ are the total and the orbital single-particle angular-momentum components along the symmetry axis, respectively. Because of the deformation the spherical shell model orbitals with intrinsic angular momentum j are split into $\frac{1}{2}(2j+1)$ energy levels. Each of these is two-fold degenerate with eigenvalues $\pm\Omega$ (i.e. the states $\pm\Omega$ have the same energy). Also, in the deformed, axially symmetric system, the π and Ω are the only good quantum numbers. Hence the ground state spin of a deformed odd-A nucleus would be Ω rather than j as is predicted by the shell model. This was one of the great successes of the Nilsson model solving many "anomalous" ground state spins. At large deformation limit the terms $\mathbf{l}\cdot\mathbf{s}$ and $\mathbf{l}^2$ in (2.20) can be neglected so, that N, n_3, Λ, Ω and π are all conserved and are therefore termed "asymptotic quantum numbers". Nevertheless, also for small deformations, $[Nn_3\Lambda]$ are used to classify the levels.

2.2.2 Cranking Models

Cranking hypothesis is:

> It is assumed that the form of the nuclear Hamiltonian of the rotating nucleus is the same as the form of the nuclear Hamiltonian prior to rotation.

The immediate consequence of this is that we can replace H' by H in eq. (2.14). Also, because of its time-independence we can write $H = \mathcal{R}^{-1}H\mathcal{R}$. Hence, in contrary to H the eigenvalue of H^ω (c.f. eq. (2.15)) is not the total energy, but

$$E^\omega = \langle \Psi'|H^\omega|\Psi'\rangle = \langle \Psi'|\mathcal{R}^{-1}H\mathcal{R}|\Psi'\rangle - \langle \Psi'|\omega\hat{I}_1|\Psi'\rangle = E_{tot} - \omega I_1, \quad (2.23)$$

and is the energy of the system, but in the rotating coordinate frame. What we measure is always E_{tot}. The quantity E^ω (or most often E' in literature[2]) is called a Routhian of the nucleus.

Observing that the total Routhian operator equals the sum of single-particle Routhian operators, we get[3]

$$H' = \sum_i h'_{s.p.}(i) = \sum_i [h_{s.p.}(i) - \omega j_1(i)]. \qquad (2.24)$$

Accordingly, the sums of single-particle Routhians as well as the alignments are

$$E' = \sum_i e'(i) \qquad (2.25)$$

---

[2] We reserve the superscript "comma" for the rotating frame quantities

[3] The way for solving this Hamiltonian is called Hartree-Fock (HF) method

and

$$I_1 = \sum_i j_1(i), \tag{2.26}$$

respectively. Note, that $X_1 = X_1'$ is the rotation axis. Hence, for a certain configuration ν the eigenvalue of h' is

$$e_\nu' = \langle\nu|h'|\nu\rangle = e - \omega j_1, \tag{2.27}$$

and the alignment

$$i_\nu = \langle\nu|j_1|\nu\rangle = -\frac{de_\nu'}{d\omega}. \tag{2.28}$$

For the "ordinary" Schrödinger equation, eq. (2.9), one sees that both "independent" and different solutions $\Psi(\mathbf{r}, t) = e^{\pm i\omega t}\Psi(\mathbf{r})$ are eigenstates to the same energy e. This is because the ordinary Hamiltonian is invariant with respect to time reversal ($h = p^2/2m + V(r)$). This is also why each Nilsson orbital can be occupied by two particles. For the cranking equations this does not apply; the "plus" and "minus" solutions are the eigenstates to the different energies e'. Therefore each single-particle Routhian is occupied by 1 or 0 particles. With pairing they are "something in between" and are therefore called quasiparticles (see subsection 2.2.3). So the important consequence of the rotation is that the two-fold degeneracy of the levels in the Nilsson model is broken.

Another consequence of the violation of the time reversal invariance is that a new conserved quantum number called signature has to be defined. It is related to the properties of nuclear states under rotation of π about the cranking axis. This is the only axis about which j_1 (or H') remains unaffected during the rotation. As is known from subsection 2.1.3, such a rotation can be expressed mathematically using:

$$\mathcal{R}_1 \Psi_\alpha = e^{-i\pi j_1}\Psi_\alpha = e^{-i\pi\alpha}\Psi_\alpha = r\Psi_\alpha, \tag{2.29}$$

where Ψ_α denotes a wave function with signature α for a single-quasiparticle state which can have the values $+\frac{1}{2}$ and $-\frac{1}{2}$. The signature r for the state, an eigenvalue of $\mathcal{R}_1$, may thus take on the two values $+i$ and $-i$. Hence for systems with odd particle number we have

1 $r = -i$, $(\alpha = +\frac{1}{2})$, $I = \frac{1}{2}, \frac{5}{2}, \frac{9}{2}, \cdots$

2 $r = +i$, $(\alpha = -\frac{1}{2})$, $I = \frac{3}{2}, \frac{7}{2}, \frac{11}{2}, \cdots$

while for systems with even particle number

3 $r = +1$, $(\alpha = 0)$, $I = 0, 2, 4, \cdots$

4 $r = -1$, $(\alpha = 1)$, $I = 1, 3, 5, \cdots$

The above four relations can be combined into one expression:

$$I = \alpha \bmod 2. \tag{2.30}$$

Any single-quasiparticle state (i.e. relations **1** and **2**) with $\alpha > 0$ is called a positive signature state and a state with $\alpha < 0$ is called a negative signature state. We obtain in this way a very important result: States which at $\omega = 0$ are degenerate have opposite signatures, a phenomenon called "signature splitting".

The total signature of a multi-quasiparticle configuration is determined by

$$\alpha_{tot} = \sum_i \alpha_i. \tag{2.31}$$

In addition to the signature the parity π remains a good quantum number in the rotating system. For the multi-quasiparticle configuration it is given by

$$\pi_{tot} = \prod_i \pi_i. \tag{2.32}$$

The single-quasiparticle Routhians or, as they are also called, "quasiparticle trajectories" can be denumerated with the help of the good quantum numbers π and α. The convention used for the labelling is shown in table 2.1.

The Nilsson potential, described in subsection 2.2.1, has been very successful in describing many aspects of the single-particle motion in deformed nuclei. However, in references [18] and [19] and also very recently in [20] by Bengtsson et al., it has been shown, that the MO-potential produces certain undesired effects connected with the velocity-dependent term l^2 in the Nilsson Hamiltonian (2.20). Such effects are not present in a more realistic finite potential of e.g. Woods-Saxon type expressed in the form

$$V_c(\mathbf{r}, \hat{\beta}) = \frac{V_0}{1 + exp[\mathbf{dist}(\mathbf{r}, \hat{\beta}, R_s)/a]}, \tag{2.33}$$

where the subscript "c" refers to the central part of a more general potential formula. Its dependence on r in spherical limit is plotted in figure 2.1. For comparison, also the V_{osc}-potential from eq. (2.16) is shown. The term $\mathbf{dist}(\mathbf{r}, \hat{\beta}, R_s)$ in (2.33) represents the distance from a point $\mathbf{r}$ to the nuclear surface.

Table 2.1: Convention used for the labelling the quasiparticle trajectories. The subscript n indicates that the trajectory is the nth trajectory for a particular set of quantum numbers (π, α).

$(\pi, \alpha)_n$	Label	
	Quasineutrons	Quasiprotons
$(+, +\frac{1}{2})_1$	A	a
$(+, -\frac{1}{2})_1$	B	b
$(+, +\frac{1}{2})_2$	C	c
$(+, -\frac{1}{2})_2$	D	d
$(-, +\frac{1}{2})_1$	E	e
$(-, -\frac{1}{2})_1$	F	f
$(-, +\frac{1}{2})_2$	G	g
$(-, -\frac{1}{2})_2$	H	h
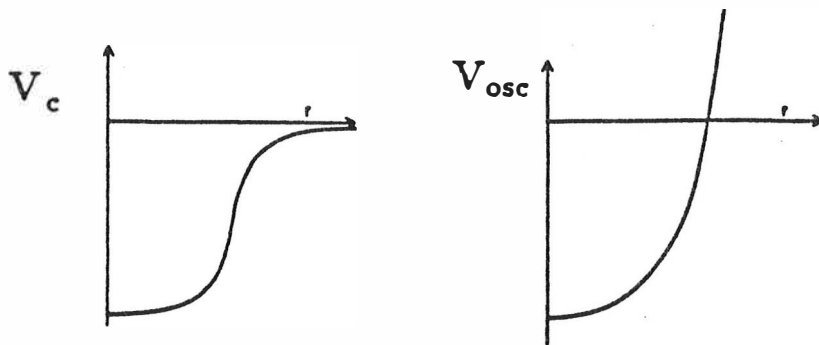
Figure 2.1: Comparison of two one-body potentials used in nuclear structure calculations: Woods-Saxon (V_c) and harmonic oscillator (V_{osc}).

The general form of the Woods-Saxon formula with its parameters is evaluated in *Appendix B*. In the systematical studies of the deformed nuclei for A > 40 [21][22] it has been found that these parameters vary smoothly with N and Z (c.f. terms κ and μ in Nilsson model). Nevertheless, a single set of parameter values for wide range of deformed nuclei has been developed by Dudek et al.[23]. Their so called "universal" parameterization in calculations of the computer code "WSBETA"[24] will be used in theoretical examinations of this work. In addition to *Appendix B* for a more extensive treatment of the Nilsson- and Woods-Saxon potentials, we refer to [25] (Appendix A on p. 1028) and to references therein.

2.2.3   Pairing Correlations

Although the two preceding "independent particle" models can predict the experimental level schemes fairly well there are still questions they cannot explain, namely;

1   Why the ground state spin of an even-even nucleus is always 0^+?

2   Why there exists an energy gap between the ground- and the first excited state in the intrinsic spectrum of an even-even nucleus?

3   Why the rotational moment of inertia is lower by about 50% than that of the rigid body value?

These are explained by means of the pairing force: In the ground state of an even-even nucleus, each pair of nucleons moves in the time reversed orbits i.e. the angular momenta are antiparallel. Hence, $I_{gs}^\pi = 0^+$ (**1**). Because the force is effective when these two interactions per orbit period are acting and almost ineffective otherwise the range of the force is short (compared to the nuclear size). The force is also attractive because the even-even nuclei are bound more strongly than their odd neighbours. This produces an energy gap Δ (**2**). Moreover, based on the first order perturbation theory it can be shown (e.g. [26] p.131) that the pairing-type interaction can cause a decrease in the moment of inertia (**3**).

In a deformed system there is a decrease in both the average level spacing and in the degeneracy of each level. Thus, the scattering of pairs of particles from one pair of time reversed orbits to another is easier to achieve and results in the diffuseness of the Fermi surface. The scattering of a pair of particles can be described by using second-quantization language, where the pairing force is given in the form

$$V_{pairing} = -G \sum_{\nu\mu} a_\nu^\dagger a_{\bar\nu}^\dagger a_\mu a_{\bar\mu} = -G \sum_{\nu\mu} \hat{P}_\nu^\dagger \hat{P}_\mu. \qquad (2.34)$$

Here, the $\hat{P}_\mu$ takes care of the annihilation of two particles from the state μ and $\hat{P}_\nu^\dagger$ creates two new ones onto the state ν. The $\bar{\nu}$ denotes a time-reversed state of ν, and G is the strength of the force. Calculations are simplified if the constant value of G is used which means that it only acts on states lying near the Fermi surface (see the discussion on monopole and quadrupole pairing below).

Nuclei in their ground states are then in specific configurations: Some pairs of nucleons are above the Fermi level, some states below the Fermi level are empty. One then needs to know the probabilities of a given level, with the squares of the amplitudes U^2 and V^2, to be unoccupied or occupied, respectively. Normalisation requires $U^2 + V^2 = 1$. This also leads to the general transformation of Bogolyubov[27][28] from the "old" particle wave functions Ψ to the "new" quasiparticle ones ϕ:

$$\phi_k = \sum_l (U_{lk}\Psi_l + V_{lk}\Psi_l). \tag{2.35}$$

In this way the problem reduces to finding the coefficients U_{lk} and V_{lk}. This can be done by using the BCS theory[29] developed to explain superconductivity in metals by Bardeen, Cooper and Schrieffer[30] in 1957:

The BCS trial wave function for the ground state is given by

$$\phi_0^{BCS} = \prod_\nu (U_\nu + V_\nu a_\nu^\dagger a_{\bar{\nu}}^\dagger)|0\rangle, \tag{2.36}$$

where $|0\rangle$ represents the wave function containing "zero quasiparticles" (vacuum state or seniority $\upsilon = 0$ state). Also, one usually requires that the expectation value of the particle number operator, $\langle\phi_0^{BCS}|\hat{N}|\phi_0^{BCS}\rangle$, equals to the proton or neutron number, considered. The minimisation of the total energy, $\langle\phi_0^{BCS}|H|\phi_0^{BCS}\rangle = min$, leads to the relations for U_ν and V_ν,

$$U_\nu^2 = \frac{1}{2}(1 + \frac{e_\nu - \lambda}{E_\nu}) \tag{2.37}$$

and

$$V_\nu^2 = \frac{1}{2}(1 - \frac{e_\nu - \lambda}{E_\nu}), \tag{2.38}$$

with e_ν and λ being the single-particle energy and the Fermi level, respectively. E_ν is the quasiparticle energy of the state ν relative to the ground state and is given by

$$E_\nu = \sqrt{(e_\nu - \lambda)^2 + \Delta^2}. \tag{2.39}$$

Here λ is the chemical potential (average Fermi level), corresponding to the proper particle number. The pairing gap parameter Δ is defined by

$$\Delta = G_0 \sum_\nu U_\nu V_\nu. \tag{2.40}$$

For an even-even nucleus, where, at the first excited state, there are at least "two quasiparticles" present (seniority $\upsilon = 2$) the pairing gap is $\geq 2\Delta$. In the odd-A nuclei the lowest excited states are the "one quasiparticle" states (seniority $\upsilon = 1$ states). The term G_0 in eq. (2.40) is the monopole pairing coupling constant indicating that the time-reversed pairs are scattering into states with time-reversed pairs only.

In order to interpret certain effects (e.g. [31] and [32]), it is necessary to include higher order terms into the pairing field. When the quadrupole term is included the pairing gap becomes

$$\Delta_\nu = G_0 \sum_\mu U_\mu V_\mu + G_2 q_2(\nu) \sum_{\mu \neq \nu} q_2(\mu) U_\mu V_\mu, \qquad (2.41)$$

which is configuration dependent through the quadrupole moment term, $q_2(\nu)$, of the state ν. The quadrupole coupling constant, G_2, is approximately one third of that of the monopole coupling constant value G_0.

Now, the Hartree-Fock-Bogolyubov (HFB) (c.f. footnote 3 on page 10) Routhian reads[4]

$$h' = h_{s.p} - \Delta(\hat{P}^\dagger + \hat{P}) - \lambda \hat{N} - \omega j_1, \qquad (2.42)$$

and its eigenvalue, called "quasiparticle Routhian" (c.f. eq. (2.27)) is

$$e'_\nu = \sqrt{(e_\nu - \lambda)^2 + \Delta^2} - \omega j_1. \qquad (2.43)$$

Figure 2.2 summarizes the effects of different terms in eq. (2.42) on single particle spectrum[33].

2.2.4   Interpretation of the Level Scheme

According to subsection 2.1.2 and eq. (2.7) the reference angular momentum of the rotating core is

$$I_1^{ref} = \mathcal{J}_{ref}^{(1)}\omega = \mathcal{J}_0^{(1)}\omega + \mathcal{J}_1^{(1)}\omega^3. \qquad (2.44)$$

From eq. (2.23) one sees that $I_1 = -dE'/d\omega$. Integrating I_1^{ref} with respect to ω yields the energy of the core in the rotating frame

$$E'_{ref} = -\int I_1^{ref}(\omega)d\omega = -\frac{\omega^2}{2}\mathcal{J}_0 - \frac{\omega^4}{4}\mathcal{J}_1 + \frac{1}{8\mathcal{J}_0}, \qquad (2.45)$$

---

[4]This approach is often called the self-consistent Hartree-Fock-Bogolyubov-Cranking (HFBC) model
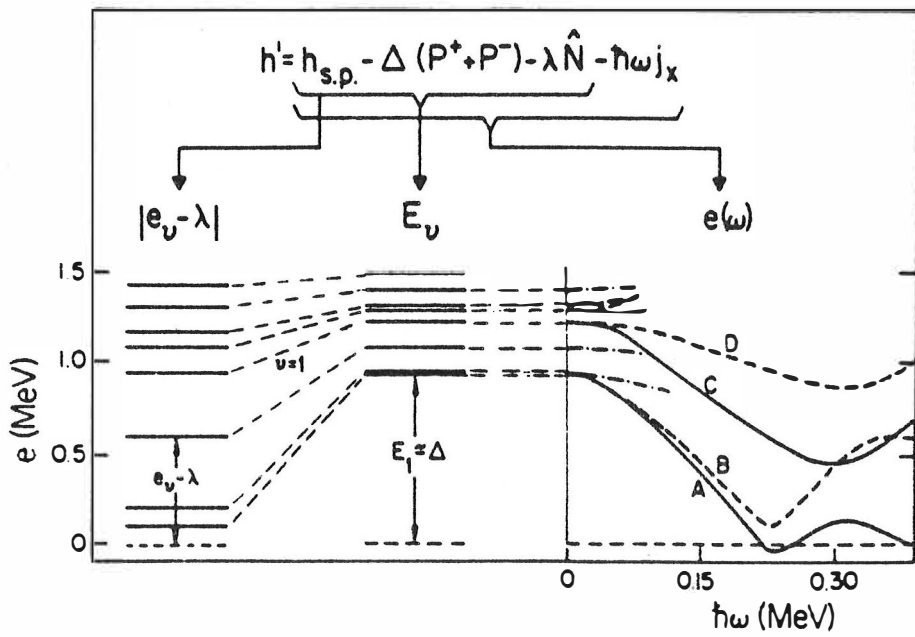
Figure 2.2: Single particle spectrum of Nilsson states (left), quasiparticle energies, E_ν, including pair correlations (center) and quasiparticle Routhians describing the effects of pair correlations and rotation on the quasiparticle orbitals (right).

where the term $1/8\mathcal{J}_0$ is a constant of integration and has been added so that $E'_{ref} \sim 0$ at $I = 0$ [2].

The single-particle energy (single-particle Routhian) and the single-particle angular momentum can be extracted from the level scheme by defining

$$e'(\omega) = E'(\omega) - E'_{ref}(\omega) \qquad\qquad (2.46)$$

and

$$i_1(\omega) = I_1(\omega) - I_1^{ref}(\omega), \qquad\qquad (2.47)$$

respectively. For an odd-A nucleus, the even-odd mass difference, denoted by Δ_{e-o}, has to be added to the right hand side of eq. (2.46), where, in contrast to the zero quasiparticle ground state in even system, the excitation energy is measured relative to the lowest single-quasiparticle state. This allows a direct comparison between the excited quasiparticle energies of the odd and even systems. The quantities e' and i_1 are, by definition, analogues to the theoretical quasiparticle Routhian e'_ν and alignment i_ν of a configuration ν in eq.'s (2.43) (or (2.27) without pairing) and (2.28), respectively. The alignment i is, in fact, a measure of the aligned spin of the broken pair of particles at a first bandcrossing between the g and s bands. A similar procedure will yield the gain in alignment at a second bandcrossing but this time the reference band is the s band.

If the interaction strength between the two crossing bands is weak, a sharp backbending is observed but if it is strong a gradual upbend over a wide range of spin and frequency values occurs. The third type of bandcrossing with moderate interaction is called a vertical upbend[15]. In practice, alignment plots are good indicators of these different types of bandcrossings. Also, eq. (2.28) says that the slope in the Routhian plot (i.e. e' vs. ω plot) of the single-particle is equal to the alignment with reversed sign. The intersection of the crossing bands (or their continuations) gives the critical frequency at which the crossing happens and is thus used to determine ω_c.

Chapter 3

Doppler-shift Recoil-distance Method

The range of lifetimes covered by different experimental methods is divided into direct methods, which measure the lifetimes τ of the levels, and into indirect methods, which measure the level widths Γ. The quantities are related by $\Gamma\tau = \hbar$. The methods have been treated e.g. in the reference [34] (and in references therein). The most basic and favourable direct methods are the electronic timing (capable to measure lifetimes ≥ 1 ns), the **R**ecoil-**D**istance Method (1 ps $- 1$ ns), used in this work, and the Doppler-Shift Attenuation Method (0.1 ps $- 1$ ps).

3.1 Principles of RDM

3.1.1 The Idea of the Method

The idea of the Doppler-shift recoil-distance lifetime experiment is to relate the lifetime τ of a nuclear state to the time T, which recoiling nuclei at a velocity v need to travel a certain distance D in vacuum. The γ-rays emitted before the time T give a Doppler-shifted peak in a γ-ray spectrum and those emitted after the time T give an unshifted peak. The decay of nuclei is described by the relation

$$\frac{dN(t)}{dt} = -\lambda N_0 e^{-\lambda t},\tag{3.1}$$

where $N(t) =$ number of nuclei in particular excited state at time t, $N_0 = N(0)$ and $\lambda = 1/\tau =$ transition rate, or the decay constant. Equation (3.1)

19

gives, for the numbers of nuclei decayed before ($S \equiv$ shifted) and after ($U \equiv$ unshifted) time T, the following relations:

$$S = N_0(1 - e^{-\lambda T}) \tag{3.2}$$

and

$$U = N_0 e^{-\lambda T}. \tag{3.3}$$

Further, we can define the quantity R from the above equations as

$$R = \frac{U}{U + S} = e^{-\lambda T}, \tag{3.4}$$

from which

$$\ln R = -\lambda T. \tag{3.5}$$

The slope of $\ln R$ vs. T yields the transition rate and, hence, the lifetime of the state under consideration, provided that we know the time T. The situation is the same in eq.'s (3.2) and (3.3), except we need to know N_0, too.

The experimental arrangement of the recoil-distance technique to find out T is shown in figure 3.1. A beam hits a target, which is so thin that the recoiling time of the excited nuclei in the target is much shorter than the lifetime τ to be measured. After the flight in vacuum the recoils are stopped by a stopper made of material with a high stopping power (heavy metal). The nuclei which decay in flight (and have a Doppler-shift in energy) and in the stopper are separated by a germanium detector placed at an angle θ with respect to the beam direction. The energy difference gives the recoil velocity v and hence the flight time T via the relation $T = D/v$.

3.1.2   The Doppler Effect

We discuss our experimental arrangement above with a reaction $M_2(m_1, m_3)M_4^*$, where M_2 and m_1 are the target nucleus and the projectile as well as M_4^* and m_3 are the recoiling excited nucleus and the light reaction product, respectively. The observed γ-ray energy of the de-exciting M_4^* is given by[35]

$$E_\gamma = \frac{1}{2}(E_i - E_f)(1 + \frac{E_f}{E_i})\frac{[1 - (v/c)^2]^{1/2}}{1 - (v/c)\cos\theta}, \tag{3.6}$$

where E_i is the total energy of M_4^*, E_f the total energy of M_4 and v its velocity. Further, θ is the laboratory angle between **v** and the detector and
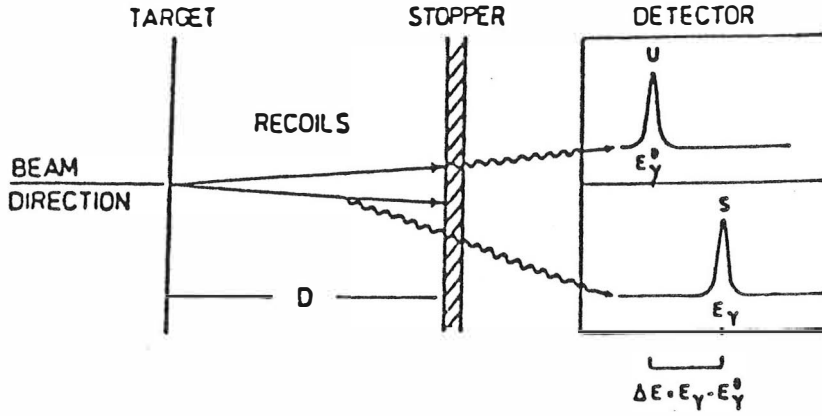
Figure 3.1: A schematic representation of the recoil-distance method for the case where the γ-rays are detected at zero angle with respect to the beam axis.

c is the velocity of light. If we denote the excitation energy $E_i - E_f$ as E_0, giving $E_f/E_i = 1 - E_0/E_i$, we get

$$\frac{1}{2}(E_i - E_f)(1 + \frac{E_f}{E_i}) = E_0 - \frac{E_0^2}{2M_4^* c^2} = E_\gamma^0.$$

Here, E_γ^0 is the observed γ-ray energy, and the term $E_0^2/2M_4^* c^2$ represents the loss of energy due to the extra recoil given to M_4. Using this and the notation $\beta = v/c$, eq. (3.6) becomes

$$E_\gamma(\theta) = E_\gamma^0 \frac{(1 - \beta^2)^{1/2}}{1 - \beta \cos \theta}. \tag{3.7}$$

Further, with the approximation $\beta \ll 1$, which is valid in most experiments, and expanding this as a power series in β, eq. (3.7) becomes

$$E_\gamma(\theta) \approx E_\gamma^0(1 + \beta \cos \theta + \beta^2 \cos^2 \theta - \frac{1}{2}\beta^2 + \cdots). \tag{3.8}$$

Omitting terms of order β^2 or higher because of small β values, one gets an useful formula to solve the recoil velocity v:

$$E_\gamma(\theta) = E_\gamma^0(1 + \frac{v}{c} \cos \theta). \tag{3.9}$$

3.1.3 Reaction Kinematics

The reaction in the RDM experiment has to be chosen so that the nuclei recoil in a narrow cone centered on the beam direction with a small spread

in velocity.

The z-component of the recoil velocity of M_4^* in the laboratory is[36]

$$\beta_z = \beta_{CM}(1 + C\cos\theta_{CM}), \tag{3.10}$$

where β_{CM} is the velocity of the center of mass in the laboratory system, $\beta_{CM} = (2m_1 E_1)^{\frac{1}{2}}/(m_1 + M_2)$, and θ_{CM} is the recoil angle of M_4^* in the CM. Further, the quantity C in eq. (3.10) is the ratio of the speed of M_4^* in the CM to the speed of the CM, and is given by

$$C = [\frac{M_2 m_3}{m_1 M_4^*}(1 + \frac{m_1 + M_2}{M_2}\frac{Q}{E_1})]^{\frac{1}{2}}. \tag{3.11}$$

In this expression $Q = Q_0 - E_x$, where Q_0 is the Q-value to the ground state and E_x is the energy of the excited state of interest.

We have two different ways to satisfy our narrow cone condition: to minimize $C\cos\theta_{CM}$, thus to use approximation $\beta_z = \beta_{CM}$ in eq. (3.10), or to fix the θ_{CM} so, that the recoil velocity in the laboratory is known. This latter condition is satisfied if we detect the outgoing particle m_3 and use the coincidence requirement with the γ-radiation. However, the loss of intensity is remarkable. The minimization of $C\cos\theta_{CM}$ may be achieved by either minimising C or making the average value of $\cos\theta_{CM}$ zero. The following two ways to minimise C are the most important:

1   With the endothermic reaction $(Q < 0)$ by choosing $E_1 = -Q(m_1 + M_2)/M_2$.

2   With the inverse reaction $(M_2 \ll m_1)$ by making $M_2 m_3/m_1 M_4^*$ small.

The average value of $\cos\theta_{CM}$ will be zero if the emission of outgoing particles is symmetric about 90^0 in the center of mass system. The compound nucleus (CN) reaction as a statistical process satisfies this condition, but elastic scattering does not.

Thus, for CN-reactions, initial velocities can be calculated from the eq. (3.10) by using the approximation

$$\beta_z = \beta_{CM} = 0.04635\frac{\sqrt{A_{m_1} E_1}}{A_{m_1} + A_{M_2}}, \tag{3.12}$$

where E_1 is in MeV and the relation $1u = 931$ MeV has been used.

3.2 Perturbing Effects

3.2.1 Recoil Velocity Distribution

As mentioned above, there exists a spread in recoil velocity followed by the reaction. This is due to an energy straggling and a multiple scattering of the beam in target and of the recoiling ions escaping from the target foil.

If the velocity distribution width is a significant fraction of the average velocity, the observed decay curve is no longer a simple exponential, but a sum of exponentials with different decay distances and weights of the velocity components determined by the distribution. This has been studied e.g. by Jones et al.[37]; in analyzing lifetime data they have taken this effect into account by expressing the ratio R in eq. (3.4) in the following series

$$R \approx \sum_{n=1}^{m} a_n e^{-\lambda \frac{D}{v_n}},$$

where $\sum_{n=1}^{m} a_n = 1$. The zeroth order theory gives $R(D) = exp[-\lambda(D - D_0)/v]$, where D_0 is the position of the target. In the previous discussion D_0 has been taken equal to zero. In practice, the real target position is not known and must be inferred from the data. Now, $R(D)$ can be written

$$R(D) = \sum_{n=1}^{m} a_n e^{-\lambda \frac{(D-D_0)}{v_n}}.$$

By keeping D_0 as a variable parameter during the lifetime fit the error arising from the velocity spread can be decreased. If possible, however, by choosing the target thin enough one gets rid off the effect almost completely.

3.2.2 Positional Dependence on the Solid Angle

According to the set-up in fig. 3.1 the solid angle of the detector is larger for unshifted γ-rays than for the shifted ones, for which the solid angle varies from a minimum value at the target to a maximum at the stopper. In the limit of a small velocity and if the nucleus moves along the beam axis the detector solid angle is given by

$$\Delta\Omega_0 = \int_0^{2\pi} d\phi \int_0^{\theta_0(t)} \sin\theta d\theta = 2\pi[1 - \cos\theta_0(t)], \qquad (3.13)$$

where $\theta_0(t)$ is the maximum half-angle of the detector as a function of the flight time. The time dependence of the $\cos\theta_0$ can be given by the relation

$$\cos\theta_0(t) = \frac{d - vt}{[(d - vt)^2 + r^2]^{\frac{1}{2}}}. \qquad (3.14)$$
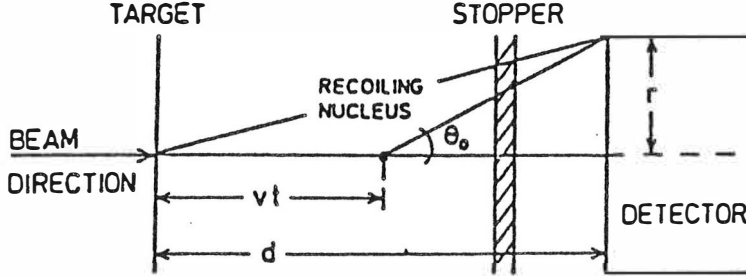
Figure 3.2: The positional dependence of the detector solid angle for the shifted and unshifted components.

Here, d is the target-detector distance, r is the detector radius and v the recoil velocity. This is shown schematically in figure 3.2.

Replacing t by the target-stopper flight time T the solid angle for the unshifted component is obtained.

3.2.3   Velocity Dependence on the Solid Angle

In addition to the static case above the most important relativistic correction is the solid angle aberration. This means, that since the recoils are forward peaked in the laboratory system, the solid angle of the detector is bigger for γ-rays emitted by moving nuclei relative to that for γ-rays emitted by the stopped nuclei. The transformation of the angles, θ_{CM} and θ_0, between a moving and a static system is given by[38]

$$\cos \theta_{CM} = \frac{\cos \theta_0 - \beta}{1 - \beta \cos \theta_0},$$

(3.15)

Thus, the effective solid angle for a system moving with a velocity v, obtained by replacing $\cos \theta_0$ by $\cos \theta_{CM}$ in eq. (3.13), is

$$\Delta\Omega(v,t) = \Delta\Omega_0 \frac{1+\beta}{1-\beta \cos \theta_0(t)} = \Delta\Omega_0(1+\chi).$$

(3.16)

Here, the quantity $(1 + \chi) = (1 + \beta)/(1 - \beta \cos \theta_0)$[39]. Since usually $cos\theta_0 \approx 1$ and $\beta \ll 1$ (or $\beta^2 \approx 0$), we have $(1 + \chi) \approx 1 + 2\beta$.

3.2.4 Alignment Attenuation

Especially after a highly aligning heavy-ion reaction the nuclear spin alignment can be considerably perturbed when the atom recoils into the vacuum. This perturbation arises from the hyperfine field due to the excited atomic electrons and causes a time dependent variation in the probability of γ-ray emission to a given detector angle. The angular distribution of the observed γ-ray intensity at an angle of θ with respect to the beam direction is given by

$$W(\theta) = 1 + \sum_k A_k Q_k G_k P_k(\cos\theta), \qquad (3.17)$$

where P_k are Legendre polynomials, $k = 2$ for dipole and $k = 2, 4$ for quadrupole radiation. The A_k's are the anisotropies which would be observed in the absence of attenuation, see e.g. [40]. The Q_k is the geometric attenuation coefficient due to the finite solid angle of the detector and G_k specifies the hyperfine attenuation and is restricted to $0 \leq G_k \leq 1$. It is clear that the attenuation is strongest for the unshifted γ-rays because of the longer flight time of the recoils which reach the stopper.

The attenuation effect is not well understood and it has been examined in many papers, see e.g. [39][38][34] and references therein. One illustrative treatment has been done by Sturm and Guidry[41], who concluded that it is sufficient to consider the problem by means of the Abragam-Pound[42] formalism which predicts an exponential attenuation

$$G_k(t) = e^{-t/\tau_k}. \qquad (3.18)$$

Here, τ_k is a k'th-order relaxation constant determined by the magnitude and form of the perturbation.

3.2.5 Lineshape Correction

The slowdown of the recoiling nuclei in the stopper does not occur suddenly but during a finite time range of about $5 \times 10^{-12} - 5 \times 10^{-13}$ seconds. In this period the recoil velocity gradually decreases causing energy broadening of the stopped component. This part of the unshifted peak area usually is lost into the background between the shifted and unshifted peaks (figure 3.3).

The calculation of the correction requires either a line shape analysis of the stopped peak and an intensity estimate of the unseen part or a computation of the shifted intensity of the stopped component. This last way is generally used in the RDM measurements. To do this one needs to know the slowing down time t_S in the stopper. This can be determined by using the stopping

UNSHIFTED REGION

SHIFTED REGION

U

APPARENT
BACKGROUND

S

I

TRUE BACKGROUND

SLOWING DOWN REGION
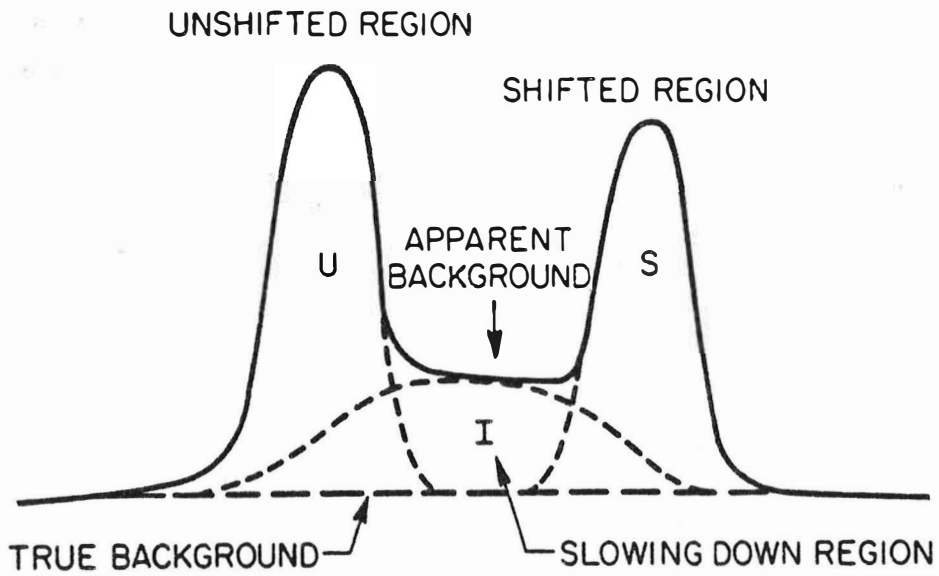
Figure 3.3: Schematic spectrum showing shifted and unshifted photopeaks, and the region between them due to γ-rays emitted while the recoil nucleus is slowing down. This intermediate intensity is included in the unshifted intensity.

power theories and values calculated for different combinations of stopper materials and recoiling nuclei, see e.g. [43][44][45]. The correction is made by multiplying the fitted unshifted intensity by the ratio $U(t_F)/U(t_F + t_S)$, where t_F is the flight time of the recoils from the target to the front surface of the stopper.

3.3 Analyzing Method

The time dependence of any decay curve is determined by the lifetime of the initial state of the observed transition and by the time structure of the transitions feeding this state. Clearly, if the decay function of each feeding transition can be measured, all the lifetimes can be obtained. Unfortunately, in most of the cases this is not possible because of unresolved feeding transitions. Only assumptions on the time structure of this unresolved feeding can be made. More complications will be encountered if a direct population of the observed levels is also present. However, this is very unusual in the reactions used in the RDM experiments. So in this case we refer to [35] where the effect of direct population on the decay function is considered thoroughly.

3.3.1 Bateman's Equation

We will apply the exponential laws which govern the decay and growth of the radioactive nuclei to the decay of the excited nuclear states. The general form of the decay and growth equations was formulated already in 1910 by Bateman[46].

In eq. (3.1) a decay relation of a state populated directly in the reaction and depopulated by a transition to a certain lower energy state was given. By writing it in an alternative form for a two cascade chain $A \to B \to C$, with transition rates λ_A and λ_B, the decay rate of the state B is[47][35]

$$\frac{dB}{dt} = A\lambda_A - B\lambda_B,$$ (3.19)

and its solution

$$B = A_0 \frac{\lambda_A}{\lambda_B - \lambda_A}(e^{-\lambda_A t} - e^{-\lambda_B t}).$$ (3.20)

Equation (3.19) can be generalized for a N-cascade chain and for a state i by

$$\frac{dP_i}{dt} = \sum_{j=i+1}^{N} P_j(t)\lambda_{ji} - P_i(t)\sum_{j=1}^{i-1}\lambda_{ij}.$$ (3.21)

Here λ_{ij} denotes the probability of the transition from the level i into the level j. The lifetime τ_i of the level is given by $\tau_i = (\sum_{j=1}^{i-1} \lambda_{ij})^{-1}$. The first summation term in eq. (3.21) takes care of the feeding into the level i while the second term describes its decay. Further, from (3.20) one can "guess" the solution of (3.21). In its most general form it can be presented as[41]

$$P_i(t) = P_i(0)e^{-\lambda_i t} + \sum_j P_j(0) \sum_{k=j}^{i} C_{jk} e^{-\lambda_k t}, \qquad (3.22)$$

where

$$C_{jk} = \frac{\prod_{l=j}^{i-1} \lambda_l}{\prod_{l=j}^{i} (\lambda_l - \lambda_k)},$$

when $l \neq k$. Expression (3.22) is Bateman's equation in its general form.

3.3.2   Analyzing Program LIFETIME

For the analysis of the experimental RDM data the program LIFETIME[48] is used in this work. As a starting point for LIFETIME was the program MASTER supplied to Oak Ridge National Laboratory from GSI, Darmstadt, by Hans Emling[49]. It performs a least squares fit to the data and incorporates the program MINUIT, which includes the function minimization and parameter error analysis developed at CERN by F.James and M. Roos[50]. The modification of LIFETIME from a PERKIN-ELMER version to one suitable for VAX computers has been made by the author. Only a brief introduction is given here. A more detailed treatment can be found from [48] and *Appendix C*.

In the program the population of each level as a function of time is determined by Bateman's equation, and the calculated values of shifted and unshifted intensities are obtained. The program allows a simultaneous description of the time dependence of moving and stopped components. It makes a least squares fit to their intensities with initial level populations and transition probabilities being treated as variable parameters.

For the unknown side-feeding transitions there is a possibility to define additional levels from which feeding transitions occur. Also, a rotational band can be modelled to feed a particular level. The modelled quadrupole moment and the initial population of the highest level in the band are variables. Experimental values for transition energies and initial and final spin values may be used.

The possible systematic error in the target-stopper distance is considered by subtracting a correction term D_0 from each flight distance. During the least squares fit the quantity D_0 can be treated as a varying parameter.

Parameters mentioned above should be included into the parameter file. When the number of levels is very large it is not practical to vary all parameters simultaneously. The advantage of the program is that one can divide the levels into different groups and perform the fitting procedure group by group from the top to the bottom along the level scheme.

The second file one must construct is the data file. It includes the needed information from the measurement; data from the nucleus and the levels to be used in the fit. Information from the possible rotational band(s) and branching ratio(s) as well as data from the stopper material and the dimensions of the detector. The program needs the distances used and for each of them the shifted and/or unshifted intensities of the transitions. Finally, it needs the energies and the initial and final spins of the transitions studied.

The third file in the input data is the velocity file. It allows the program to calculate the recoil velocity. The program needs only the energy calibration coefficients, the desired transitions and the centroids of the shifted and unshifted peaks for each distance. During the run one can determine whether it will use this value or the own one given in the data file.

In *Appendix C* the five most important subroutines and calculation methods are explained.

3.3.3 Matrix Elements and Transition Probabilities

If $\mathcal{M}(L\mu)$ denotes the electromagnetic multipole operator, multipolarity L with components $\mu = L, L - 1, ..., -L$, one gets the amplitudes of transitions from the initial state I_i to the final state I_f by means of the matrix elements[5][25]

$$\langle \Psi^{I_f}_{K_f,M_f} | \mathcal{M}(L\mu) | \Psi^{I_i}_{K_i M_i} \rangle = \frac{\langle I_i M_i L\mu | I_f M_f \rangle}{\sqrt{2I_f + 1}} \langle I_f K_f \parallel \mathcal{M}(L) \parallel I_i K_i \rangle. \quad (3.23)$$

This leads one to define the reduced transition probability, independent on M_i, as[25][51]

$$B(L; I_i K_i \rightarrow I_f K_f) \equiv \sum_{\mu, M_f} |\langle \Psi^{I_f}_{K_f, M_f} | \mathcal{M}(L\mu) | \Psi^{I_i}_{K_i, M_i} \rangle|^2$$

$$= \frac{1}{2I_i + 1} |\langle I_f K_f \parallel \mathcal{M}(L) \parallel I_i K_i \rangle|^2, \quad (3.24)$$

---

[5]Non-diagonal elements define the so called transitional moments. The "static" moments are defined by the diagonal elements of (3.23)

where $B(L)$'s are in units of $e^2(fm)^{2L}$ and $(e\hbar/2Mc)^2(fm)^{2L-2}$ for electric and magnetic transitions, respectively. The term $(e\hbar/2Mc) = \mu_0$ is the nuclear magneton with M as a mass of a proton.

By means of this the transition probability of a γ-transition, with multipolarity L and transition energy E_γ, is given by[26]

$$\lambda(L) = \frac{8\pi(L+1)}{[L(2L+1)!!]^2}(\frac{1}{\hbar})(\frac{E_\gamma}{\hbar c})^{2L+1}B(L). \tag{3.25}$$

If the lifetime $\tau = 1/\lambda$ is known this gives the "experimental" reduced transition probability.

The electric (E) and magnetic (M) multipole operators are given by[52][53][25]

$$\mathcal{M}(E,L,\mu) = \sum_{q=1}^{A} e(q)r_q^L Y_{L\mu}(\theta_q,\phi_q) \tag{3.26}$$

$$\mathcal{M}(M,L,\mu) = \sum_{q=1}^{A} \{g_s(q)\mathbf{s}_q + \frac{2g_l(q)}{L+1}\mathbf{l}_q\}\nabla_q[r_q^L Y_{L\mu}(\theta_q,\phi_q)]\mu_0.$$

In these equations $\mu = 0, \pm1, \pm2, ..., \pm L$. The $e(q)$ is an effective charge of a qth nucleon outside the core, r_q is its radial coordinate and $g_s(q)$ and $g_l(q)$ are its spin and orbital g-factors. For neutrons $g_l = 0$ and $g_s = -3.826$ and for protons $g_l = 1$ and $g_s = 5.585$. Their expectation values give the charge/current distributions (shapes/s.p.-motions) in nuclei.

As an example we treat the electric quadrupole operator $\mathcal{M}(E,2)$:

The intrinsic electric quadrupole moment Q_0 yields the static properties of intrinsic nuclear states ϕ, and is defined by

$$eQ_0(K) = \sqrt{\frac{16\pi}{5}}\langle\phi_K|\mathcal{M}(E,L=2,\mu=0)|\phi_K\rangle. \tag{3.27}$$

Especially, by choosing $r^2 Y_{20} = \sqrt{\frac{5}{16\pi}}(3z^2 - \mathbf{r}^2)$ in (3.26) we have restricted us to axial symmetry. Transforming $\mathcal{M}$ into the intrinsic frame we obtain the relation between the static laboratory and intrinsic moments as[54][55]

$$Q(I) = \frac{3K^2 - I(I+1)}{(I+1)(2I+3)}eQ_0(K). \tag{3.28}$$

The reduced transition probability is

$$B(E2;I,0 \rightarrow I-2,0) = \frac{5}{16\pi}\langle I020|I-2,0\rangle^2[eQ_0]^2 \tag{3.29}$$

with

$$\langle I020|I-2,0\rangle^2 = \frac{3I(I-1)}{2(2I-1)(2I+1)}.\tag{3.30}$$

These have been made valid for the ground- and s-bands of even-even nuclei ($K = 0, I_f = I_i - 2$). Also, this "rotational modelling" defines a reduced transition quadrupole moment Q_t (in eb) as $Q_t = eQ_0$.

By solving eq. (3.25) with respect to $B(L)$ one obtains

$$B(2; I,0 \to I-2,0) = 0.082\frac{\lambda(E2)}{(E_\gamma)^5(1+\alpha)}[e^2b^2],\tag{3.31}$$

where λ is in $(ps)^{-1}$ and E_γ in MeV. Also, α is the total conversion coefficient, which is important for low γ-energies and heavy elements. Combining eq.'s (3.29) and (3.31) we obtain

$$\lambda(E2) = 1.22\langle I020|I-2,0\rangle^2 Q_t^2 E_\gamma^5(1+\alpha)[(ps)^{-1}],\tag{3.32}$$

from which the Q_t value is extracted and is used as an "experimental" result in comparisons with predicted values.

An "estimate" for Q_t can be achieved by using so called Hill-Wheeler[56] coordinates β and γ (model-dependent quantities). This parameterization gives

$$Q_t = \frac{3}{\sqrt{5\pi}}ZeR_0^2\beta_2\frac{\cos(30^0 + \gamma)}{\cos 30^0}.\tag{3.33}$$

The mean nuclear radius R_0 is assumed to have a mass dependence of $R_0 = r_0A^{1/3}$ and Ze is the nuclear charge. Further, β_2 and γ come from the nuclear surface expansion represented in the body-fixed coordinates for the shapes of a quadrupole type, as

$$R(\theta', \phi') = R_0\{1 + \alpha_{20}Y_{20}(\theta', \phi') + \alpha_{22}[Y_{22}(\theta', \phi') + Y_{2-2}(\theta', \phi')]\}\tag{3.34}$$

with the definitions

$$\begin{aligned}\alpha_{20} &= \beta_2\cos\gamma\\ \alpha_{22} &= \frac{1}{\sqrt{2}}\beta_2\sin\gamma.\end{aligned}$$

In this convention $\gamma = +60(-60)$ corresponds to a rotation of an oblate nucleus about an axis parallel (perpendicular) to the symmetry axis. $\gamma = 0$ describes the rotation of a prolate nucleus about an axis perpendicular to the symmetry axis. For the definitions of the three semi-axes of the triaxial nucleus the reader is referred to [26] (p.8). Instead of the β_2 the "surface" parameter $\epsilon \approx 0.95\beta_2$ is also widely used (c.f. subsection 2.2.1, eq.'s (2.17) and (2.18)).

Also, extending (3.33) up to the second order in β_2, Q_t can be given by[54][57]

$$Q_t = 2\sqrt{\frac{3}{5\pi}} Z e R_0^2 \beta_2 (1 + 0.360\beta_2) \cos(30^0 + \gamma). \qquad (3.35)$$

Finally, in order to have a simpler unit for comparison with experimental transition rates the so called Weisskopf units[58] is often used (W.u.'s are defined in reference [51], p.389, too). In calculations there, a nuclear radius constant of 1.2 fm is used giving e.g.

$$B(E2)_{sp} = 0.05940 A^{4/3} [e^2 (fm)^4]. \qquad (3.36)$$

Chapter 4

Experiments and Results

4.1 Experimental Techniques

4.1.1 Spectroscopy Experiment

Excited states in the nucleus ^{172}Os were produced via the reaction ^{144}Nd(^{32}S,4n)^{172}Os at a beam energy of 162 MeV. The beam was provided by the Holifield Heavy Ion Research Facility at Oak Ridge National Laboratory. The thickness of the enriched ^{144}Nd target was 1 mg/cm^2. Yield functions measured at the bombarding energies 155, 162 and 171 MeV showed that the 4n-reaction channel was optimized at a beam energy of 162 MeV. The intensities of the 232 keV and 484 keV transitions for these three bombarding energies are shown in the figure 4.1a). Also shown are the intensities of the 228 keV and 378 keV transitions in ^{172}Os. From the figure one can see that both γ rays from ^{172}Os, which is formed by a four particle evaporation process, have more or less equal intensities at the bombarding energies of 155 MeV and 162 MeV and starts to fall off at a 171 MeV energy. Therefore, the 232 keV and 484 keV γ rays, whose intensities are already falling off between 155 MeV and 162 MeV, are most likely from a nuclide formed by a three particle evaporation process, assigned to ^{173}Os later (see subsection 4.2.2). The calculations made with the fusion evaporation code Julian-PACE[59] for the ^{144}Nd-^{32}S combination are in the agreement with this observation. This can be seen from the figure 4.1b), where the statistical calculations for different reaction channels as a function of the beam energy are shown.

The spectroscopy measurements were made with the Oak Ridge Compton Suppression Spectrometer System. This system was incorporated into the
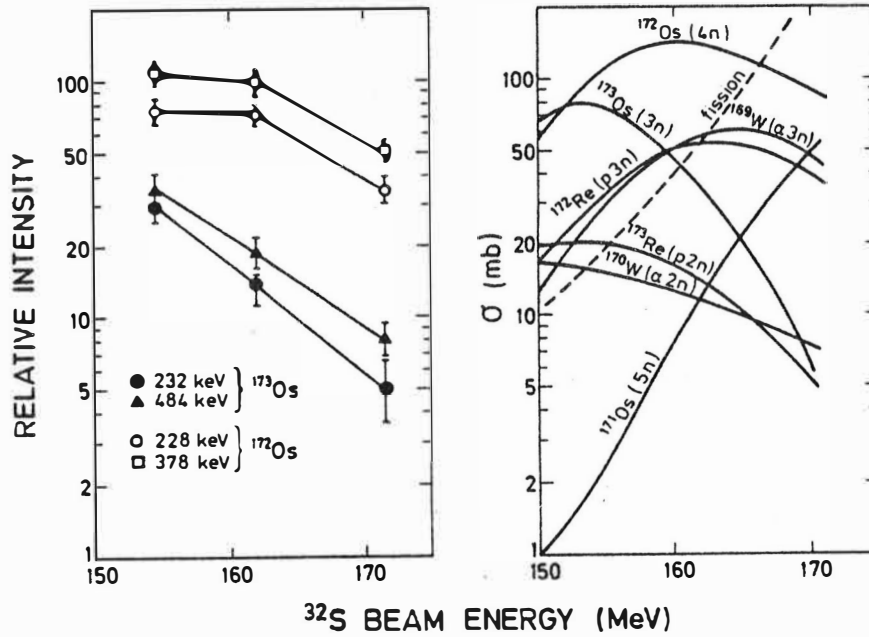
Figure 4.1: a) The measured yield functions for γ rays from ^{172}Os (4n channel) and from ^{173}Os (3n channel). b) Statistical yield function calculations for different reaction channels.

Spin Spectrometer (for a detailed description of the Spin Spectrometer, see [60]), a 4π array of 72 NaI detectors, by replacing 19 of the NaI units with the Compton-suppressed Ge units. In the present experiment 12 BGO and 7 NaI(Tl) anti-Compton shields were used. The Compton-suppressed Ge units were positioned at angles 0^0(1 unit), 24^0(3), 63^0(4), 87^0(3), 93^0(1), 116^0(4) and 156^0(3) to the beam direction. In this way, 56 million $\gamma - \gamma$ coincidence events were collected. Also, the associated total energy and γ ray multiplicity were recorded. Since the target was thin, the reaction products recoiled from the target and decayed in the flight, and hence, the γ rays were fully Doppler shifted.

The γ ray spectra from the 19 Ge detectors were gain-matched and a 4096×4096-channel coincidence matrix was generated using coincidences between all possible pairs of detectors. The γ energies were measured in a separate experiment by using a Pb-backed target which stopped the recoiling nuclei and eliminated the problem of correcting for the Doppler shift. A standard ^{152}Eu source was used for the energy calibration. This source and a ^{182}Ta source were used to obtain the efficiency calibration for summed spectra from all 19 detectors.

By using the Ge detectors located at 24^0 and 87^0 (and at 156^0 and 93^0) it was possible to extract the angular correlation information from the $\gamma - \gamma$ coincidence data. The standard directional correlation was utilized from the oriented states (DCO) relationship[61] of the form

$$R = \frac{W(\theta_1 = 24^0, \theta_2 = 87^0)}{W(\theta_1 = 87^0, \theta_2 = 24^0)}, \tag{4.1}$$

where $W(\theta_1, \theta_2)$ is the angular correlation function and θ_1 and θ_2 are the angles at which two coincident γ rays are observed with respect to the beam direction. The γ rays at 24^0 (or at 87^0) were detected in coincidence with the known stretched E2 reference transitions at 87^0 (or at 24^0). For fully aligned nuclei, the ratio of these intensities $I(87^0, 24^0)/I(24^0, 87^0)$ is approximately a factor of two larger for stretched quadrupole transitions than for stretched dipole transitions. The multipolarity of transitions with a spin change of two units were assumed to be E2.

4.1.2 Lifetime Experiment

For the lifetime experiment, the beam, the beam energy and the reaction were same as for the spectroscopic experiment. In this case the thickness of the enriched, self-supporting ^{144}Nd target was 1.35 mg/cm^2. The metallic neodynium also provided an electrical contact with the target cone. The flatness of the target was obtained by stretching it over the conical frame of
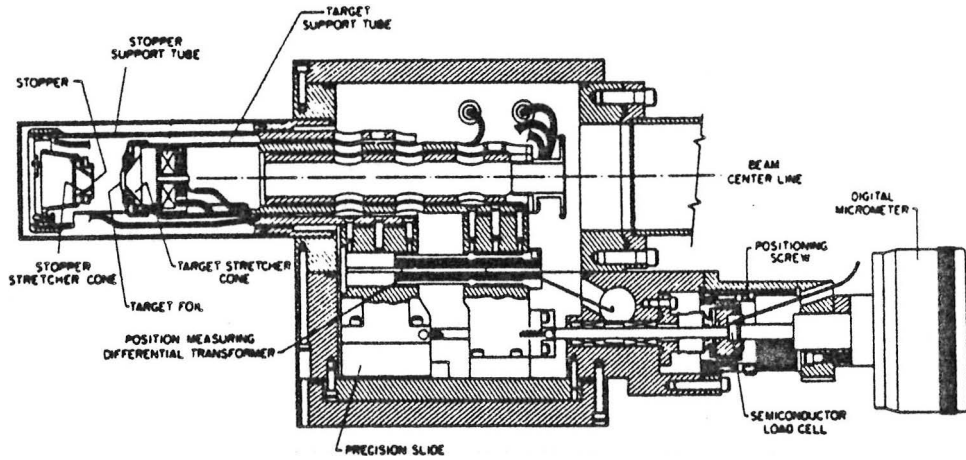
Figure 4.2: A schematic drawing of the Doppler-shift recoil-distance device

the Doppler-shift recoil-distance device[62][63]. A schematic drawing of the device is shown in figure 4.2. The tubes supporting the target and the stopper and all connecting elements in the positioning mechanism were made from appropriate combinations of Invar, stainless steel and aluminium. This was done to minimize any change in the target-stopper separation as a result of thermal expansion. The tube supporting the target foil is fixed while that supporting the stopper is movable and attaches to an assembly which connects to the core element of a position measuring differential transformer and the movable stage of a precision slide. The movement of the slide, with a corresponding change in the target-stopper separation, is accomplished by means of an external positioning drive screw mechanism. Once the desired target-stopper separation is achieved, determined by the differential transformer readout, the high-precision digital micrometer is contacted to the semiconductor load cell until a load of 150 g is attained, and the micrometer reading provides the final value for the target-stopper separation. The stopping medium for the recoiling nuclei consisted of 34 mg/cm^2 lead evaporated onto a 0.2 mm nickel foil which was stretched over a stopper cone. The stopper cone orientation was controlled by three differential screws. Parallelism between the target and the stopper was achieved by requiring a laser beam reflected from the stretched nickel foils (placed at the target and stopper positions) to reach the same spot.
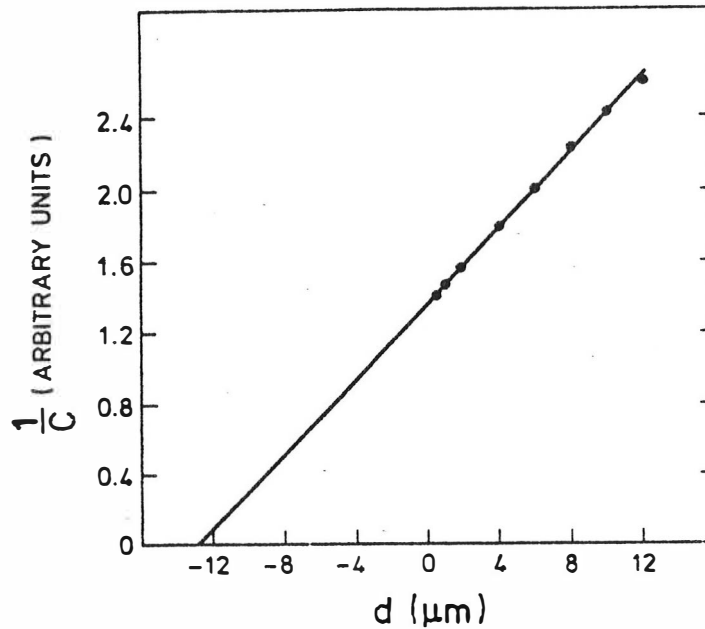
Figure 4.3: The measurement of the target to the stopper capacitance to determine the zero distance. The offset distance is $-12.8 \pm 0.2\mu$m.

At close distances, the zero distance determination was done by using the standard capacitance technique[64], where the inverse proportionality of the capacitance between the target and the stopper foils to the target-stopper distance is used. Pulses of 1 kHz with a constant amplitude were sent to the capacitance and the height of the pulses coupled through the capacitance were converted to the digital readings in the multichannel analyzer to determine the target-stopper separation. The inverse pulse height vs. micrometer reading data were fitted with a straight line. The least squares fit to the close distance readings gave the offset distance of $-12.8 \pm 0.2\mu$m and is shown in the figure 4.3. This was done under "beam on" conditions to avoid possible temperature dependent effects.

In figure 4.4 the schematic drawing of the experimental setup is shown. The γ-rays were recorded in seven high resolution Ge-detectors. The separable shifted and unshifted lines were detected in the detector placed at 0^0 and 9.7 cm from the target. This detector was surrounded by a bismuth germanate (BGO) anti-Compton shield. In addition, an annular BGO detector ("catcher") was located behind the Ge detector to intercept the photons Compton scattered in the forward direction, thus leading to improvement
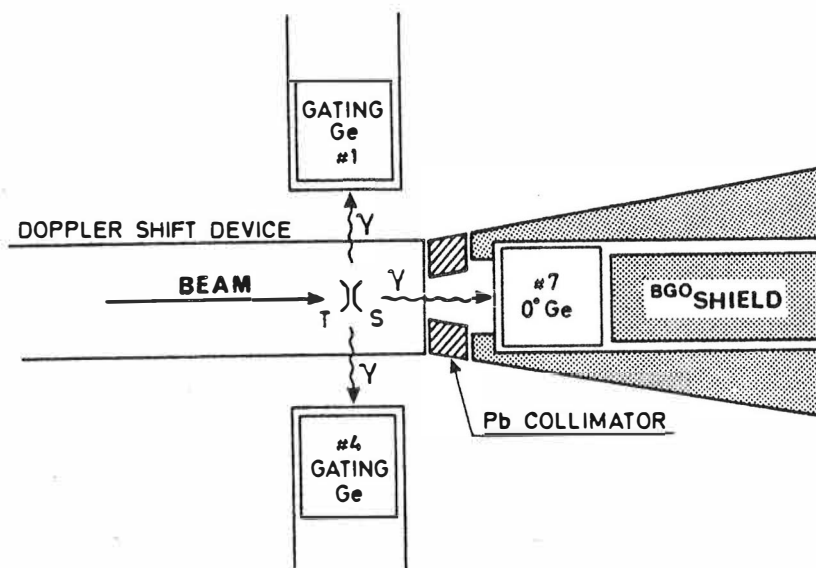
Figure 4.4: An illustrative diagram of the plunger-detector arrangement for the present experiment. Six Ge detectors are arranged at 90^0 to the beam axis and a Ge detector placed at 0^0 is surrounded by the anti-compton (BGO) shield.

in the low-energy region of the γ-ray spectrum recorded. When measured with a ^{60}Co source, these shields provided an average Compton suppression factor of 5.3 with a peak-to-total ratio of 51.4%. A lead collimator located in front of the BGO shield prevented it receiving direct hits by γ-rays, and it collimated γ-rays to the center of the Ge detector. A copper-cadmium combination was used as an absorber for this detector. The other six Ge detectors were placed in a ring perpendicular to the beam axis. These 90^0 detectors with the Ta-Sn-Cu absorbers were located at a distance of 5.9 cm from the target.

Figure 4.5 shows a block diagram of the electronics setup used for the experiment. The coincidence counts between any of the 90^0 detectors and the 0^0 detector were recorded on the magnetic tape for 20 different target-stopper distances ranging from 0 to 2.0128 mm. A lead backed target was used for the absolute zero distance measurement. The pulse height for the capacitance readings were also stored on the tape for each event.

For each distance a 4096 $\times$ 4096 channel matrix was built from the $\gamma - \gamma$ coincidence events after the gains of all the 90^0 detectors were matched. The
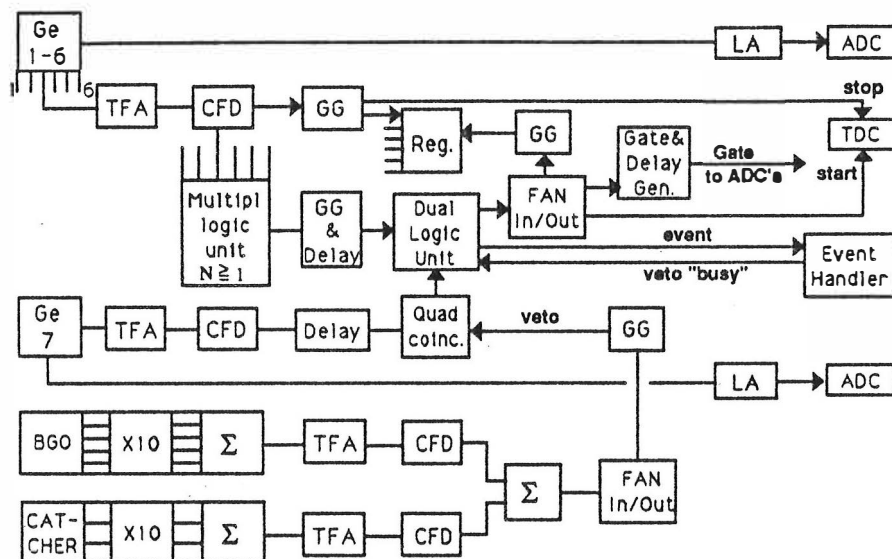
Figure 4.5: A block diagram of the electronic setup used in the lifetime experiment.

counts in the total projected coincidence spectra changed from $\sim 26 \times 10^6$ counts for the zero distance spectrum to $\sim 5 \times 10^6$ counts for the largest distance spectrum. The recoil velocity of the ^{172}Os nuclei, deduced from the energy difference of the shifted and unshifted peaks of the yrast 2^+, 4^+ and 6^+ transitions, was 4.767 ± 0.060 μm/ps which corresponds to 1.59% of the velocity of light.

4.2   Results of Spectroscopy Experiment

4.2.1   Data Analysis and Results for ^{172}Os

A spectrum gated on the sum of transitions de-exciting yrast states from 2^+ to 10^+, showing the prominent transitions and the overall quality of the data, is displayed in figure 4.6.

The energies, relative γ ray intensities, DCO ratios and the proposed spin-parity assignments for transitions in ^{172}Os are given in table 4.1. In this subsection figures 4.6 − 4.12 represent data and the level scheme is given in figure 4.13.

Yrast band: Figure 4.7 shows a spectrum gated on γ rays de-exciting yrast sequence states from 14^+ to 26^+. It reveals the higher spin members of the yrast sequence up to spin 30^+.

The DCO ratios used to establish the spin assignments in the yrast sequence are shown in figure 4.8. The ratios of the intensities $I(87^0, 24^0)/I(24^0, 87^0)$, eq. (4.1), have been normalized so that the mean for expected stretched E2 transitions is unity. Clearly, the 8^+ and higher transitions in this band are of stretched E2 character. It is observed, however, that the $2^+ \rightarrow 0^+$, $4^+ \rightarrow 2^+$ and $6^+ \rightarrow 4^+$ transitions show reduced DCO ratios. This is a general feature of lower spin transitions and results from the attenuation of alignment.

The 471 keV γ ray, which appears in the yrast sequence, was established as a doublet since it also occurs in the 1050, 602 and 924 keV gates (see the level scheme, figure 4.13). Also, from these it was determined that the $8^+ \rightarrow 6^+$ transition in the yrast sequence has an intensity of 65.8 units and the weaker transition of 6.4 units. The less intense member of this doublet was placed in the same sequence with the 476 keV γ ray by observing that in the 471 keV gate, the ratio of the intensity of the 471 keV γ ray to that of the 476 keV γ ray was 0.51. This was further confirmed by observing that the ratio of the intensity of the 476 keV γ ray to that of the 429 keV γ ray in the 471 keV gate was significantly larger than the same ratio in the 228 keV gate.

Band 1: The spectra obtained by gating on 635 keV and 624 keV transitions confirmed that these and the 687 keV transition are members of the extension beyond the backbend of the ground band up to spin 18^+. Although speculative, there is also some evidence for the 20^+ and 22^+ members of this band extension.
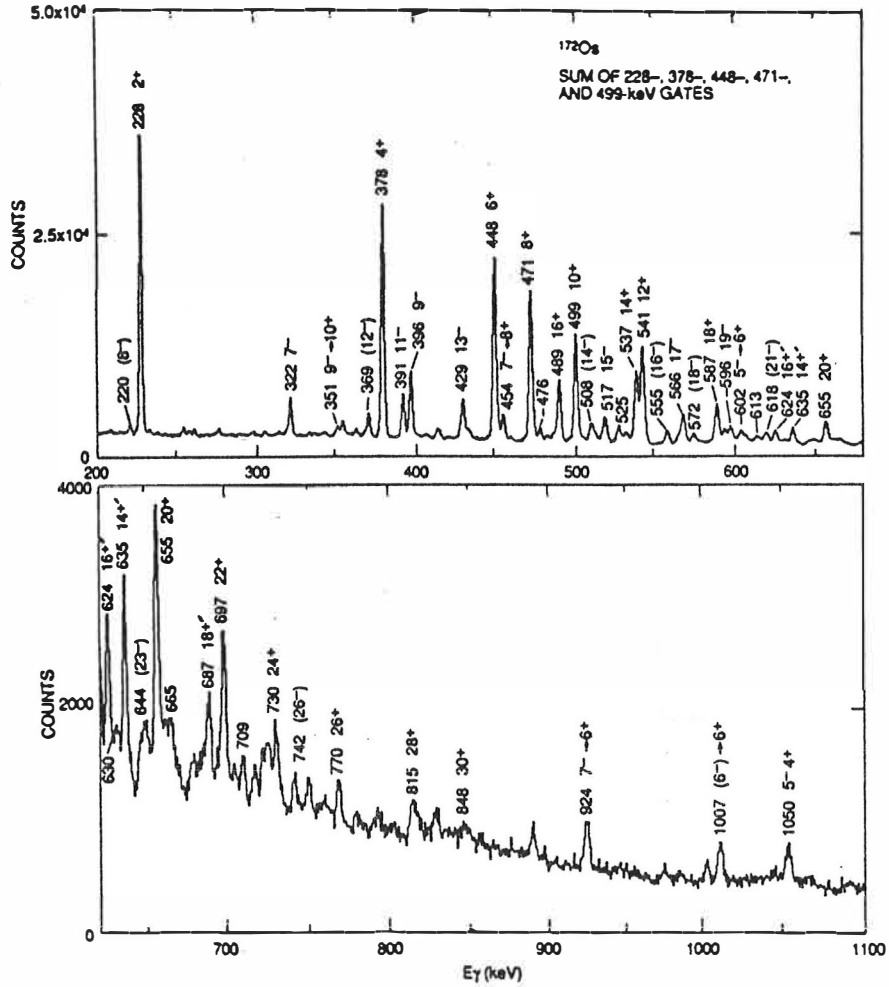
Figure 4.6: A spectrum of γ rays in coincidence with the transitions from 2^+ to 10^+ in ^{172}Os. Gamma rays from ^{172}Os are labeled with the energy in keV and the initial spin and parity.

Table 4.1: Transition energies, relative γ ray intensities, directional correlation ratios and spin-parity assignments for transitions in ^{172}Os.

E_γ(keV)[a]	I_γ[b]	DCO[c]	I_i^π	I_f^π
128.0±0.3	2.0±1.0			13^-
220.3	2.9±0.4		(8^-)	(6^-)
227.8	82.1±1.5[d]	0.65±0.03	2^+	0^+
261.2±0.3	1.5±0.3		(10^-)	9^-
322.0	15.0±0.6	0.87±0.11	7^-	5^-
350.8±0.2	2.5±0.4		9^-	10^+
353.7	2.7±0.5		(10^-)	(8^-)
369.4	8.3±0.5		(12^-)	(10^-)
378.4	100.0±1.3	0.81±0.03	4^+	2^+
391.2	19.3±0.7	1.09±0.21	11^-	9^-
396.2	28.5±0.8	1.01±0.19	9^-	7^-
405.0±0.3	2.9±0.6		(6^-)	5^-
428.7	20.8±1.0	0.99±0.13	13^-	11^-
439.8±0.3	0.9±0.5		(12^-)	12^+
448.4	88.9±1.8	0.92±0.03	6^+	4^+
453.5	12.3±0.9	0.63±0.13	7^-	8^+
470.5	65.8±1.8	1.00±0.03	8^+	6^+
471.2	6.4±0.9			9^-
476.1	6.9±0.8			
488.5	24.7±1.1	1.05±0.07	16^+	14^+
498.9	54.8±1.5	0.98±0.04	10^+	8^+
508.3	12.4±0.9		(14^-)	(12^-)
516.9	18.1±1.1	1.17±0.25	15^-	13^-
525.4	10.9±0.9			
536.7	35.2±1.3	0.99±0.04	14^+	12^+
540.6	47.6±1.5	0.98±0.03	12^+	10^+
555.1	9.3±0.6		(16^-)	(14^-)
556.3±0.3	4.2±1.0			11^-
564.9±0.2	6.6±0.8			
565.6	18.4±0.8	0.98±0.13	17^-	15^-
572.0	7.5±0.6		(18^-)	(16^-)
586.8	24.0±0.8	1.32±0.08	18^+	16^+
591.5±0.3	9.0±0.6			
595.6	14.0±0.7	0.89±0.12	19^-	17^-
601.7	11.2±0.7	0.53±0.10	5^-	6^+

Table 4.1: Continued

605.0	5.9±0.6		(20^-)	(18^-)
611.6±0.3	2.1±1.0		(10^-)	9^-
612.6	5.4±0.5			21^-
618.1	10.7±0.5		21^-	19^-
623.9	9.7±0.5		$16^{+\prime}$	$14^{+\prime}$
630.0±0.3	3.5±0.4			
634.9	10.4±0.5		$14^{+\prime}$	$12^{+\prime}$
644.4±0.2	3.2±0.4		(23^-)	21^-
647.4	4.3±0.4		(22^-)	(20^-)
655.1	15.6±0.5	1.17±0.10	20^+	18^+
664.6±0.3	5.2±0.5			
684.2	2.5±0.5		(25^-)	(23^-)
687.4	5.5±0.4		$18^{+\prime}$	$16^{+\prime}$
692.3	3.0±0.5		(24^-)	(22^-)
696.6	9.4±0.5	1.08±0.12	22^+	20^+
709.1±0.2	2.7±0.4			
723.9±0.3	3.0±0.5		$(20^{+\prime})$	$18^{+\prime}$
730.3	4.4±0.4		24^+	22^+
741.8±0.3	2.0±0.5		(26^-)	(24^-)
742.5	1.7±0.4			
751±1	3.5±0.5		$(22^{+\prime})$	$(20^{+\prime})$
769.5	2.3±0.4		26^+	24^+
792.5±0.3	2.9±0.6		(28^-)	(26^-)
814.6±0.2	1.4±0.5		28^+	26^+
847.5±0.3	1.7±0.5		30^+	28^+
924.1±0.2	5.0±0.4	0.74±0.15	7^-	6^+
1006.6±0.3	4.3±0.4		(6^-)	6^+
1049.8±0.2	8.0±0.5	0.50±0.30	5^-	4^+

[a] Uncertainty in transition energies is 0.1 keV unless otherwise stated.
[b] Relative γ ray intensities are normalized to the intensity of the $4^+ \rightarrow 2^+$ transition (=100).
[c] The DCO ratios are defined by eq. 4.1 in the text. Ratios are normalized to unity for stretched E2 transitions in the yrast sequence.
[d] Not corrected for coincidence efficiency.
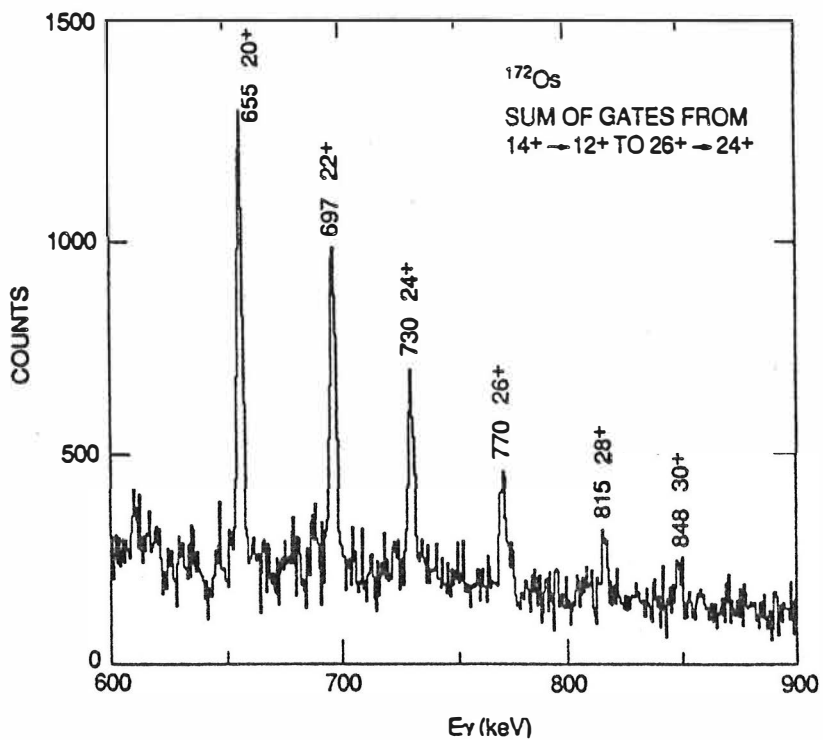
Figure 4.7: A spectrum of γ rays in coincidence with 14^+ to 26^+ transitions, showing the high spin transitions in the yrast band. The transitions are labeled with energies in keV and initial spin and parity.
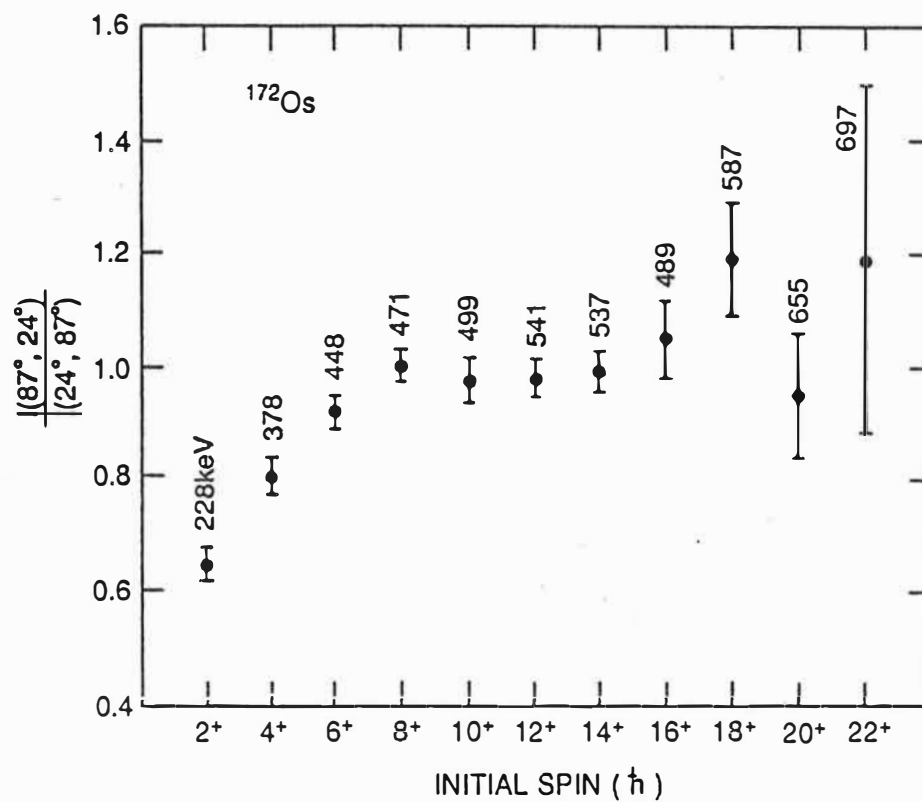
Figure 4.8: The DCO ratios for members of the yrast sequence in ^{172}Os. The ratios for stretched E2 transitions are normalized to unity.
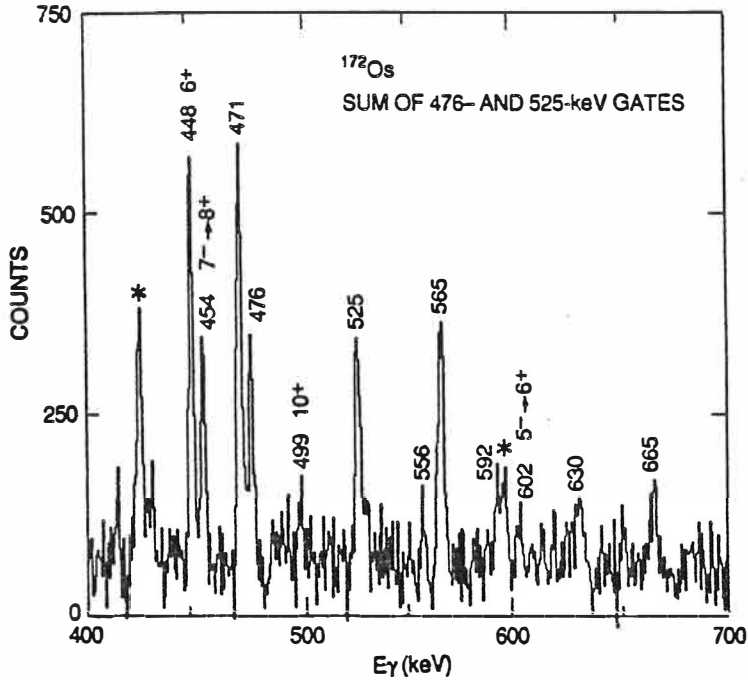
Figure 4.9: Spectrum of γ rays in coincidence with the 476 keV and 525 keV transitions, showing high spin transitions of band 2. Peaks labeled with (*) are contaminants from unidentified nuclei.

Band 2: This band is established through coincidence relationships seen in the 396 keV, 476 keV and 525 keV gates. A spectrum gated on the 476 keV and 525 keV transitions, showing all of the transitions in this band, is displayed in figure 4.9. The transitions in the band were ordered by intensity and energy systematics.

Based on the branching ratios, approximately 30% of the 471 keV peak intensity in figure 4.9 can be assigned to the $8^+ \rightarrow 6^+$ transition in the ground band. In addition, the 565 keV transition is also part of a doublet, the other member being the 566 keV transition in band 3. The data show that the 391 keV and 476 keV transitions are in coincidence with each other, indicating that there is an 80 keV transition between the 2846 keV level of the band 2 and the 2766 keV level of the band 3. This low energy transition was not observed. The starred peaks in the figure 4.9 are from coincidences in one of the unidentified bands having transitions of the same energy as those in our gates.

Band 3: Figure 4.10 shows a spectrum gated on the transitions of energy 429 keV, 517 keV and 596 keV. This spectrum reveals the γ rays which
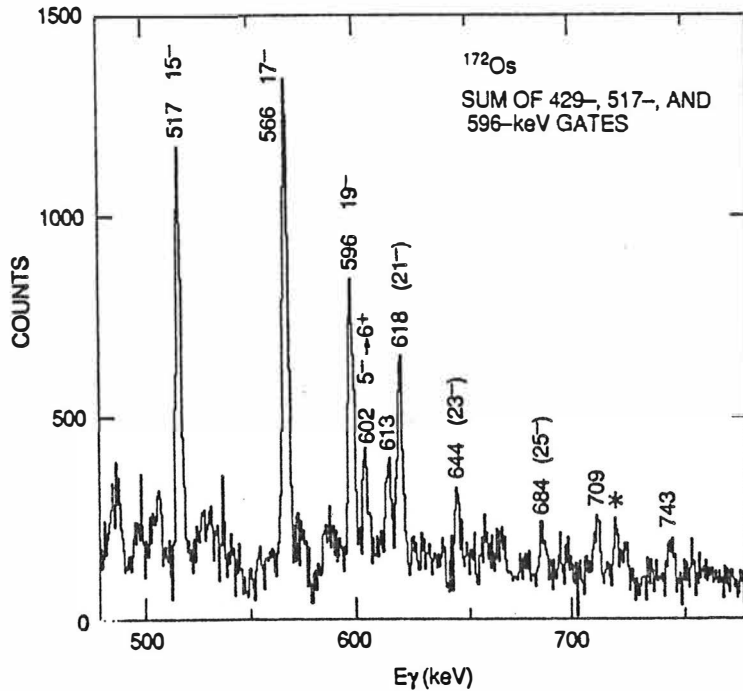
Figure 4.10: A spectrum of the transitions in coincidence with the 429, 517 and 596 keV γ rays, indicating high spin states in the odd-spin negative-parity band (band 3) and those transitions feeding into the (21^-) level of this band. The peak labelled with $(\ast)$ is a contaminant from an unidentified nucleus.

were assigned to the higher spin members of a band and to the transitions from another band feeding into the 5491 keV level. The starred peak in this spectrum is from an unidentified impurity.

The transitions in this band show DCO ratios characteristic of streched quadrupole transitions as can be seen in figure 4.11. Typical values are $\sim 0.8 - 1.2$ for $L = 2$- and ~ 0.6 for $L = 1$ transitions.

Further, the 454, 602, 924 and 1050 keV interband transitions appear to be stretched dipole transitions, since their DCO ratios are all significantly less than unity. Based on the features of the band 3 and known systematics, it is concluded that this band has $(\pi, \alpha) = (-, 1)$, commonly called the AE band (see the discussion later). Therefore, it follows that the dipole transitions between this and the ground band are E1 in nature. In addition, it is pointed out that the assignment of states as a continuation of the band 3 beyond the 5491 keV level and those as a side band feeding in at this point presented some difficulty. All five transitions above the 5491 keV level were
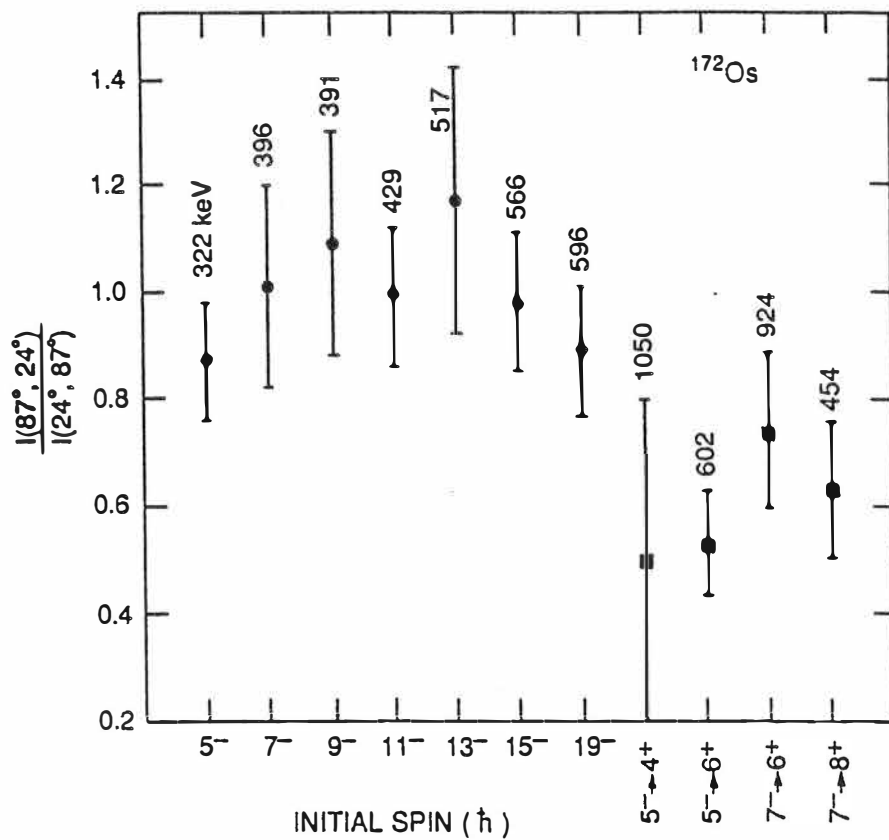
Figure 4.11: The DCO ratios for members of the band 3 and for the inter-band transitions between this band and the ground state band. The ratios for the stretched E2 transitions are normalized to unity.
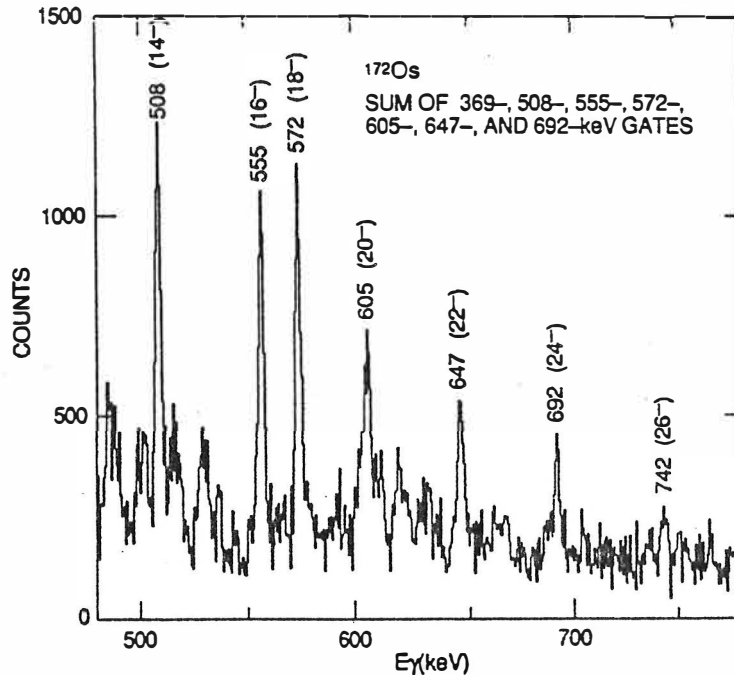
Figure 4.12: A spectrum of the γ rays in coincidence with the transitions of 369, 508, 555, 572, 605, 647 and 692 keV, showing the high spin transitions of band 4.

in coincidence with a gate set at 618 keV. The problem is that these five transitions are quite weak and, thus, the spectra generated by gating on each one individually are not of good statistical quality. They do lead one to conclude, however, that there are two cascades feeding into the 5491 keV level. Based on the aligned angular momentum in the signature partner of the band 3 (band 4) and on the systematics of $(-, 1)$ bands, it is assumed that the 644 keV and 685 keV transitions are members of the $(-, 1)$ band of ^{172}Os.

Band 4: The members of band 4 are shown in figure 4.12, a spectrum in coincidence with the transitions of energy of 369, 508, 555, 572, 605, 647 and 692 keV. These γ rays all show strong coincidence relationships with the 448, 378 and 228 keV transitions in the yrast sequence, and weaker coincidence relationships with the 396 keV and 322 keV transitions in the odd-spin band.

From the coincidence data, one finds that a 998.8 keV γ ray feeds into the 10^+ state, implying a level at 3023 keV. The data also indicate that 889.6 keV and 828.9 keV transitions probably feed the 8^+ state and originate

from the levels at 2415 keV and 2354 keV, respectively. However, because of their questionable nature these three levels are not shown in the level scheme:

The level scheme for ^{172}Os, as deduced from the coincidence data discussed above is shown in figure 4.13. The γ rays have been grouped into these five bands. The levels up to the spin value of 24^+ in the yrast band have been reported previously in [3] and [4]. The ordering of the γ rays in the level scheme is based on the observed coincidence relationships, on intensity arguments and on systematics.

4.2.2 Data Analysis and Results for ^{173}Os

Also, γ−rays belonging to other reaction channels besides the $4n$ channel which leads to the ^{172}Os have been identified. In addition to the ^{169}W and ^{170}W from the $\alpha 3n$ and $\alpha 2n$ reaction channels, respectively, five other distinct bands can be observed, which, based on the x-ray spectra and energies, are probably Re and odd-mass Os isotopes.

One of these bands has been identified as being that of the ^{173}Os. A spectrum gated on the 232 keV γ−ray of this band is shown in the Figure 4.14. The identification of Z=76 was based on the x-rays in coincidence with the members of this band. The identification of A=173 was made by means of excitation function results mentioned before and shown in figure 4.1.

The energies and intensities are given in table 4.2 and the level scheme is shown in figure 4.15.

For the spins and the parities of this band the tentative values are based on the assumption that this is a rotational band with stretched E2 transitions. The band head spin and parity value $13/2^+$ is expected from the systematics of odd-neutron nuclei in this region, i.e. the $i_{13/2}$ neutron orbital is near the Fermi surface in this mass region. Since we are probably dealing with the low-Ω projections in the $i_{13/2}$ shell, a spin $13/2$ could not present the ground state of ^{173}Os. By the same token, the level energies shown are only relative values.
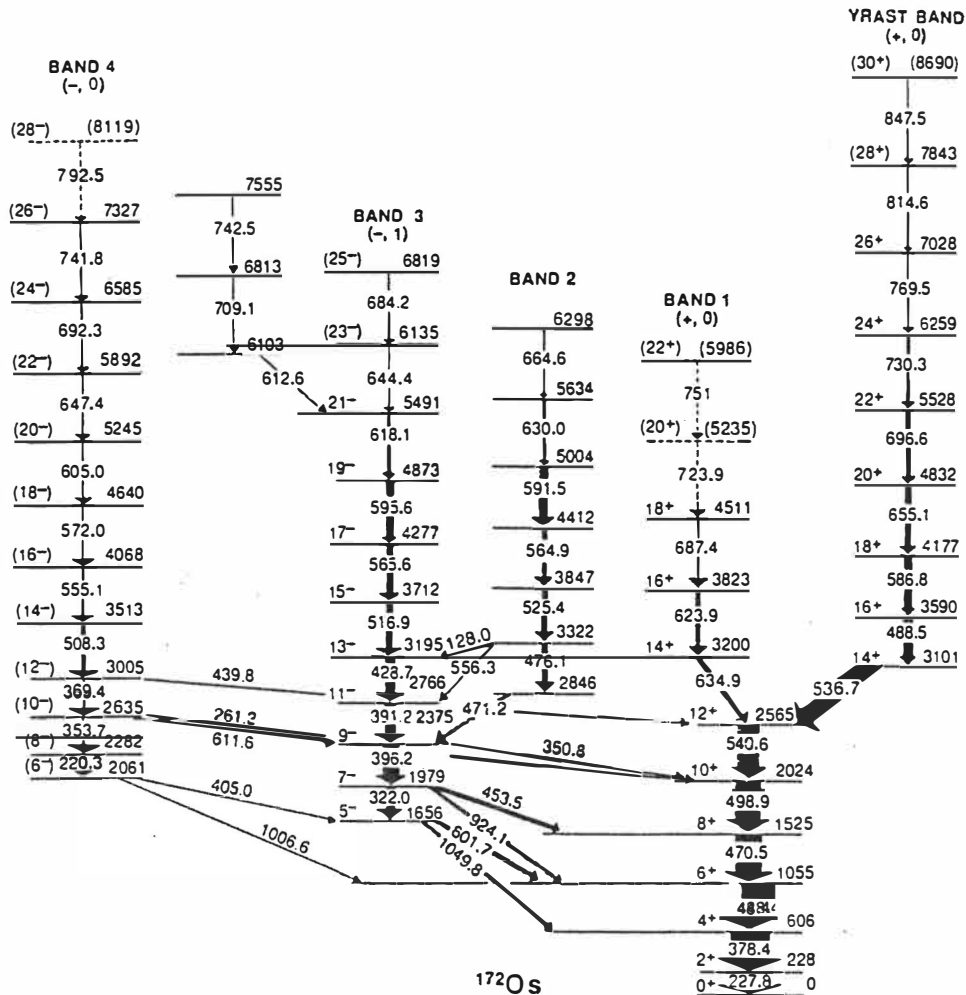
Figure 4.13: The level scheme of ^{172}Os. The energies are in keV. The relative transition intensities are indicated by the widths of the arrows. The parentheses and dashes indicate tentative assignments.

Table 4.2: Transition energies, relative intensities and spin-parity values for the γ rays from ^{173}Os.

$E_\gamma(\text{keV})^{a)}$	$I_\gamma^{b)}$	$I_i^{\pi c)}$	$I_f^{\pi c)}$
232.4		$(17/2^+)$	$(13/2^+)$
389.5	100 ± 8	$(21/2^+)$	$(17/2^+)$
484.1	88 ± 8	$(25/2^+)$	$(21/2^+)$
535.5	79 ± 8	$(29/2^+)$	$(25/2^+)$
572.2	59 ± 6	$(33/2^+)$	$(29/2^+)$
608.6	50 ± 6	$(37/2^+)$	$(33/2^+)$
645.7	45 ± 5	$(41/2^+)$	$(37/2^+)$
687.7 ± 0.2	32 ± 5	$(45/2^+)$	$(41/2^+)$
735.5 ± 0.2	22 ± 5	$(49/2^+)$	$(45/2^+)$
781.0 ± 0.2	19 ± 4	$(53/2^+)$	$(49/2^+)$
819.4 ± 0.3	11 ± 4	$(57/2^+)$	$(53/2^+)$

[a]Uncertainty in transition energies is 0.1 keV unless otherwise stated.
[b]Relative $\gamma-$ray intensities are normalized to the intensity of the 389.5 keV transition (=100).
[c]Based on the assumption that the band head spin and parity are $13/2^+$.
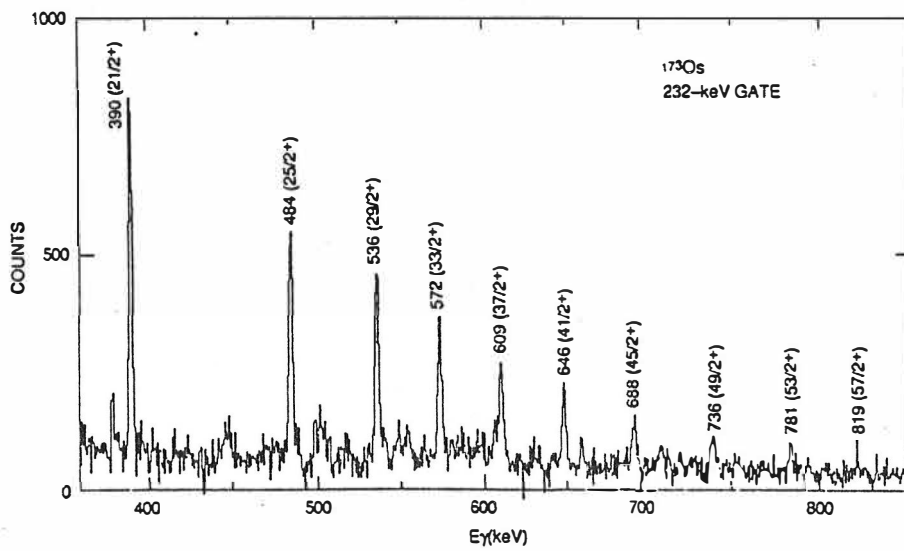
Figure 4.14: A spectrum of γ rays in coincidence with the 232 keV transition in ^{173}Os. The spin and parity assignments are based on the assumption of $I = 13/2^+$ for the band head.
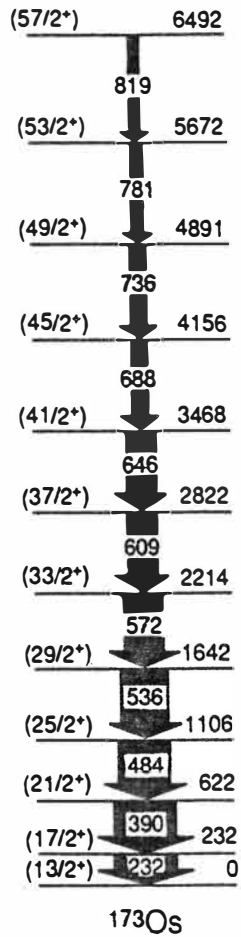
Figure 4.15: The level scheme of ^{173}Os. The energies are in keV. Relative intensities are indicated by the widths of the arrows. The spin assignments are based on the assumption that the band head spin is $13/2^+$.

4.3 Results of Lifetime Experiment

4.3.1 About the Data Analysis

As stated before, a given state may be populated by the side feeding as well as by the cascades of higher members of the band. The side-feeding problem can be eliminated by gating on the band members higher than the transition of interest and the coincidence spectra generated in this manner are referred to as "Gated Above Data" (GAD). This is done at some cost in the statistical quality of the data, especially for the higher spin states. Nevertheless, this type of gating is often hightly advantageous, especially in those cases where the side-feeding has a longer effective lifetime than the state of interest.

Although the sidefeeding problem is not removed, the total projected co-incidence spectrum often produces the best data for extracting lifetimes because of its good statistical quality. Data extracted from such a spectrum is noted as "Total Projected Data" (TPD). The problem here is that the γ rays present in the spectrum from the different reaction channels cause difficulty in the analysis. For illustrative purposes, we show in figure 4.16 a portion of the total projected spectra at four different distances. From the figure one can clearly see the variation of the shifted and unshifted components as a function of the plunger distance. One can also see the broadening of the flight peaks as a function of the energy. This behavior is caused by the velocity distribution due to the energy straggling and multiple scattering of the beam and of the recoiling ions escaping from the target foil as well as by the angular variation of the direction of the γ rays (c.f. section 3.2). So, when the energy resolution of the unshifted peaks ranged from 1.3 keV to 1.6 keV for the 2^+ (228 keV) and 20^+ (656 keV) states, respectively, the corresponding range for the shifted components was from 1.6 keV to 3.3 keV.

The spectra generated by gating on γ rays below the transition of interest offer another excellent avenue for the data analyses. Such data are noted as "Gated Below Data" (GBD). Decay curves obtained from such coincident data include essentially the same fraction of side-feeding as the ones obtained from the total projected spectrum.

Because the peaks in the 90^0 spectra are Doppler broadened, it was necessary to set the gates fairly wide; from 4.2 keV to 9.0 keV for $2^+ \rightarrow 4^+$ and $20^+ \rightarrow 18^+$ transitions, respectively. Hence, it is especially important to check carefully for interfering transitions in the gates from nuclei produced by the other reaction channels. To illustrate this point, we show in
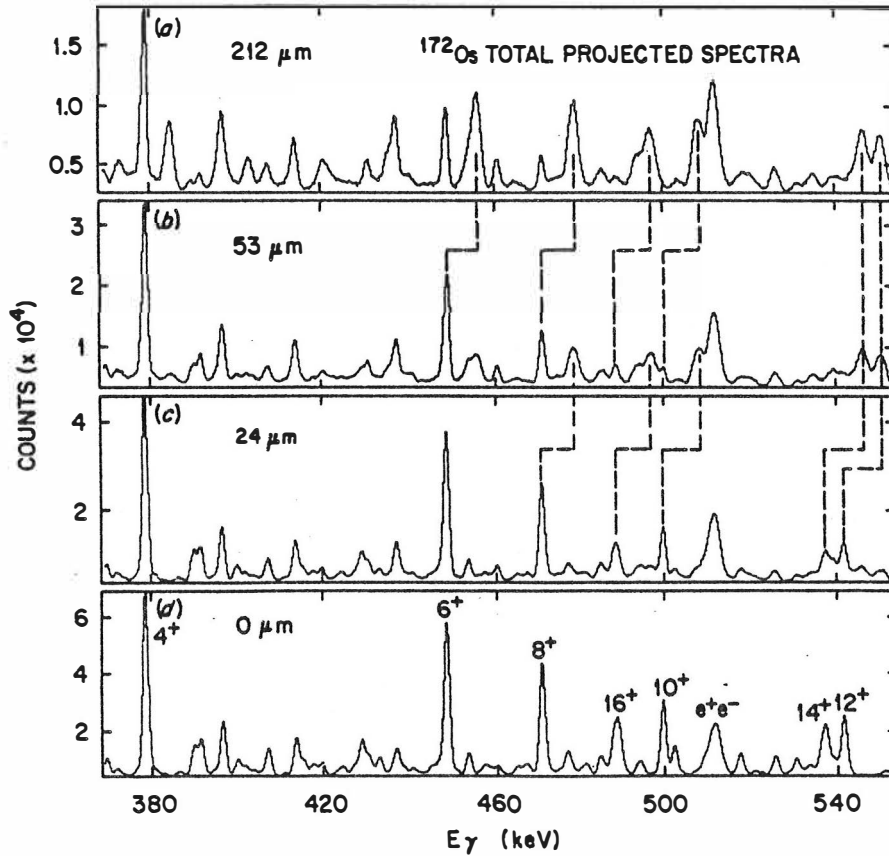
Figure 4.16: Partial total projection coincidence spectra covering the yrast E2 transitions from states 4^+, ..., 16^+ of ^{172}Os. Spectra have been measured at the indicated distances.
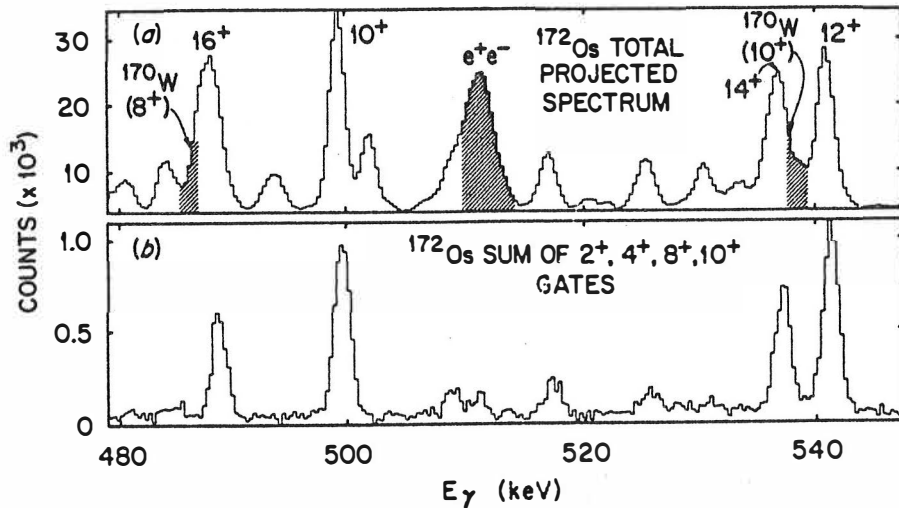
Figure 4.17: a) Total projected spectrum and b) the spectrum gated by the transitions from states 2^+, 4^+, 8^+ and 10^+. From the figure one can see how the gating cleans the spectrum and makes the intensity analysis easier. In addition to the annihilation peak the two contaminating transitions from ^{170}W are indicated.

figure 4.17 a region of the total projected spectrum and the corresponding region of the spectrum gated by the transitions $2^+ \rightarrow 0^+$, $4^+ \rightarrow 2^+$, $8^+ \rightarrow 6^+$ and $10^+ \rightarrow 8^+$ (background subtracted). In the total projected spectrum the strong yrast 8^+ and 10^+ peaks of ^{170}W (see the hatched regions in the figure) cause difficulties in the analysis of the 16^+, 14^+ and 12^+ intensities. Especially, it was difficult to obtain a reliable fit of the 12^+-14^+ peaks in the total projected spectrum. We excluded the 6^+ state in our gate. This is because the ^{170}W yrast 14^+ transition is located at the same energy.

The γ-ray peaks in the spectra were fitted by standard techniques to obtain the areas. Only the peak heighs were free parameters. Response functions for the peak shapes were determined by fitting the most prominent peaks in the spectra. Peak positions and widths were predetermined and in the spectrum analysis procedure, these two parameters were allowed to vary only within prescribed limits. In the fits of the shifted components an asymmetrical peak shape was used. The intensities were corrected with

respect to the detection efficiency (different for the unshifted and shifted components), solid angle, aberration and lineshape (see section 3.2). In addition, the obvious corrections for the internal conversion and for the coincidence efficiency were applied. The normalization of the data from each target-stopper distances to compensate the different amount of integrated beam current was based on the three strongest peaks i.e. on the yrast $2^+ \rightarrow 0^+$, $4^+ \rightarrow 2^+$ and $6^+ \rightarrow 4^+$ transitions of ^{172}Os.

The extracted decay curves were analyzed with the computer program LIFETIME (see section 3.3.2). The shifted and unshifted intensities were fitted separately to determine the best values of the lifetimes, rather than by fitting the ratio of unshifted to total intensity, as is often done. Two step cascades were chosen for the side feeding. The side feeding intensity needed for the intensity balance at each level was assigned to the top member of the cascade and the two transition rates were calculated by using the known transition energies and spin values. The quadrupole moment value $eQ_0 = 6eb$ was chosen in each case as a starting value for the modelled rotational bands.

The χ^2-function calculated by the main program LIFETIME was analyzed by the subprogram MINUIT with the three minimization routines explained in *Appendix C*. The corrections to the data mentioned earlier were applied after every minimization. Parameter error analysis was produced by the subroutine MINOS with the condition of one-standard-deviation confidence interval of 68%.

4.3.2 Treatment of Side Feeding

As mentioned above, the two-step cascade model was provided for the unseen sidefeeding. Since the observed levels are not near the top of the cascade, one expects the sidefeeding rate to be zero at $t = 0$ and to rise to some maximum value at $t = t_m$ before falling off. This results in the sidefeeding into each level being described by three parameters; the initial population of the upper level of the sidefeeding cascade and the two lifetimes. The notation A indicates the side feeder which decays into a lower level, noted as B, which then decays directly into the yrast state under consideration (see subsection 3.3.1). The differential of B, in eq. (3.20), with respect to time is zero when

$$\lambda_A e^{-\lambda_A t_m} = \lambda_B e^{-\lambda_B t_m},$$

from which it follows that the time t_m of maximum feeding rate, which coincides with the peak in the population of level B, can be written in

terms of the lifetimes[47]

$$t_m = \frac{1}{\lambda_B - \lambda_A} \ln \frac{\lambda_B}{\lambda_A} = \frac{\tau_A \tau_B}{\tau_A - \tau_B} \ln \frac{\tau_A}{\tau_B}. \qquad (4.2)$$

Hence, t_m is positive and real for either $^{1)}\tau_A > \tau_B$ or $^{2)}\tau_B > \tau_A$. It can be emphasized that when $0 < t < t_m$ the activity of the level A always exceeds the activity of level B, that is, dB/dt is positive. This provides for the short time behaviour of the decay of transition studied. Conversely, when $t > t_m$ the activity of B exceeds the activity of A i.e. dB/dt is negative. This large time part, e.g. long-lived component of the decay, is dominated by either the decay of A or B depending on which of the relations $^{1)}$ or $^{2)}$ holds.

As can be seen from eq. (4.2) a maximum feeding at a lifetime τ occurs farthest from $t = 0$ when both levels have lifetimes equal to τ. No physical case is known for which $^{3)}\tau_A = \tau_B$, but if the two lifetimes are nearly equal we may write an approximation $\tau_A \sim \tau_B(1 + \delta)$, $\delta \ll 1$. Making use of the expansion of the logarithm, $\ln(1 + \delta) \sim (\delta - \frac{\delta^2}{2} + \frac{\delta^3}{3} - \cdots)$, one gets

$$\begin{aligned} t_m &= \tau_B \frac{1 + \delta}{\delta} (\delta - \frac{\delta^2}{2} + \cdots) \\ &\sim \tau_B(1 + \frac{\delta}{2}) \sim \tau_B \sqrt{\frac{\tau_A}{\tau_B}} \\ &= \sqrt{\tau_A \tau_B}. \end{aligned} \qquad (4.3)$$

This provides for the irregular behaviour of the decay function especially at "long" feeding times:

In two cases, the 6^+ and 8^+ transitions in GBD, a two level sidefeeding cascade was found to be inadequate. Hence it was necessary to add a third level to the feeding cascade to obtain a feeding rate which peaked later than could be obtained with a two level cascade with the appropriate behaviour at large times. However, as has been pointed out also in earlier lifetime measurements[6] at ORNL, the extracted lifetimes of the levels of interest seemed not to be very sensitive to the number of levels in the sidefeeding cascades.

4.3.3 Results for the Yrast Band

Decay curves were obtained for all yrast transitions up to spin 20^+. The transitions were analyzed first by using the total projected data, TPD. Sample decay curves of the states 12^+, 16^+ and 20^+ extracted from the TPD are shown in figure 4.18. The points represent the experimental data

with application of the corrections described earlier. The solid curves are the fitted results from the program LIFETIME. The ordinate is the intensity of the shifted and/or unshifted components. The abscissa shows the flight times of the recoils in ps. Because of the ^{170}W-contamination of the $12^+ \rightarrow 10^+$ and $14^+ \rightarrow 12^+$ transition pair (see Figure 4.17) the fit was done in three parts: first the transitions $2^+ \rightarrow 0^+, \cdots, 10^+ \rightarrow 8^+$ and $16^+ \rightarrow 14^+$, $\cdots, 20^+ \rightarrow 18^+$ were fitted separately and finally all the transitions from $2^+ \rightarrow 0^+$ up to the $20^+ \rightarrow 18^+$ transition were fitted together. A four-state rotational band and a five-state rotational band was used to model the side feedings of the highest member of the cascade studied and of the 12^+ state, respectively. This was done according to the level scheme information, figure 4.13. Otherwise, a two step cascade was used. A MINOS analysis was performed for all of the yrast transitions studied. From the results of these three fitting approaches, average values of the lifetimes τ were calculated and are shown with their MINOS errors in column 3 of table 4.3.

The yrast transitions $12^+ \rightarrow 10^+$, $14^+ \rightarrow 12^+$ and $16^+ \rightarrow 14^+$ were also analyzed from the GBD results. First, a spectrum from the sum of the gates on the transitions from the $2^+,4^+,8^+$ and 10^+ states was generated. The $6^+ \rightarrow 4^+$ transition was omitted because of the ^{170}W contaminant in this peak. However, for better statistics, the sum of gates on the $2^+,\cdots,16^+$ transitions was also used to determine the lifetimes of the 18^+ and 20^+ states. Further, the lifetimes of the states $6^+, \cdots, 16^+$ were analyzed from the spectrum produced by summing the gates on the $2^+ \rightarrow 0^+$ and $4^+ \rightarrow 2^+$ transitions. Unweighted arithmetic average values from these GBD fits are shown in column 5 of table 4.3. Decay curves of states 10^+, 14^+ and 18^+ extracted from the GBD are shown in figure 4.18.

Note that the yrast band lifetime values in columns 3 and 5 of table 4.3 were determined by using our standard modelling described above. As will be discussed below, we were also able to extract the lifetimes for several of the E2 transitions in the $(-,1)$ sideband and to determine the partial lifetimes and B(E1) values for several of the transitions between this band and the yrast band. With this sideband information available, we proceeded one step further in our fit to the yrast states. New fits to the TPD for the 2^+ through 10^+ and to the GBD for the 6^+ through 10^+, analyzed from the sum of spectra gates set on 2^+ and 4^+ transitions, were performed where the standard modelling plus the information from the $(-,1)$ sideband were used in the fitting parameter space. In this fit, the lifetimes of the sideband states and the interband branching ratios were permitted to vary within their established error limits. The results from this fit of the yrast band are shown in column 4 of table 4.3 for TPD and in column 6 for GBD. We describe this detailed fitting procedure and the results of it because of the very interest result: Inspection of the lifetime results from these two fitting
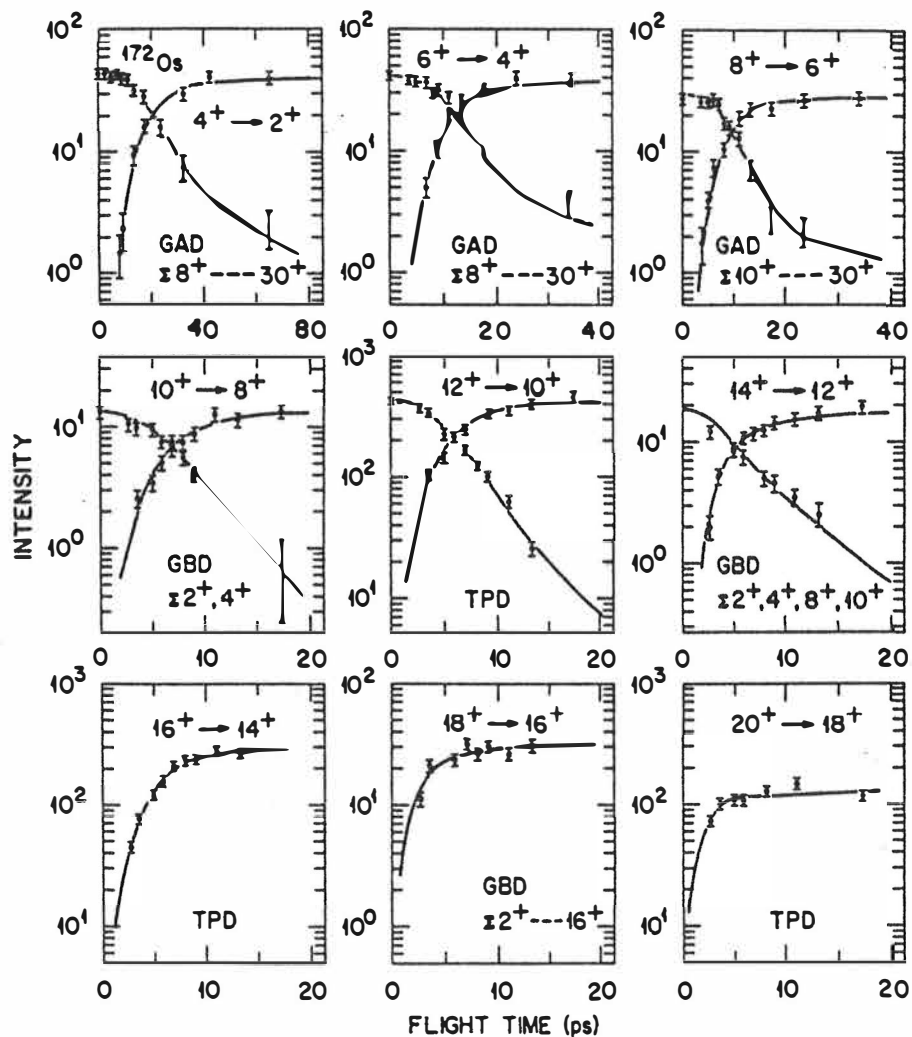
Figure 4.18: Decay curves for some members of the yrast sequence in ^{172}Os obtained from the total projected data (TPD), gated below data (GBD) and gated above data (GAD). See text for explanations.

Table 4.3: Lifetimes of the yrast states obtained from the total projected data (TPD) and gated below data (GBD). Results from the fits without and with the measured $(-,1)$ sideband transitions are compared.

J_i^π	E_γ(keV)	TPD		GBD	
		Standard modeling[a]	Standard modeling plus (-,1) sideband feeding[b]	Standard modeling[a]	Standard modeling plus (-,1) sideband feeding[b]
		τ(ps)[c]	τ(ps)[c]	τ(ps)[c]	τ(ps)[c]
2^+	227.8	163^{+7}_{-9}	165^{+5}_{-6}		
4^+	378.4	$11.2^{+1.3}_{-0.9}$	$10.5^{+1.0}_{-0.8}$		
6^+	448.4	$2.4^{+0.2}_{-0.2}$	$2.2^{+0.2}_{-0.2}$	$3.3^{+0.7}_{-0.7}$	$3.1^{+0.7}_{-0.6}$
8^+	470.5	$1.9^{+0.3}_{-0.2}$	$1.7^{+0.1}_{-0.2}$	$1.5^{+0.4}_{-0.3}$	$1.2^{+0.4}_{-0.3}$
10^+	498.9	$1.7^{+0.2}_{-0.2}$	$1.5^{+0.2}_{-0.2}$	$1.9^{+0.3}_{-0.6}$	$2.0^{+0.5}_{-0.3}$
12^+	540.6	$0.9^{+0.1}_{-0.2}$		$1.3^{+0.3}_{-0.4}$	
14^+	536.7	$0.5^{+0.4}_{-0.4}$		$1.1^{+0.4}_{-0.4}$	
16^+	488.5	$2.7^{+0.5}_{-0.9}$		$4.4^{+0.4}_{-0.5}$	
18^+	586.8	$1.5^{+0.5}_{-0.7}$		$1.7^{+1.9}_{-0.5}$	
20^+	655.1	< 1.9		< 0.7	

[a]The standard modelling involves two-state cascade (except for 6^+ and 8^+ in GBD three-state cascade, see text) side feeding to each level and a four-state rotational band built on the highest member of the cascade.
[b]Decay curve fits done with the standard modeling plus the measured information extracted on the E2 transitions in the (-,1) band and the E1 transitions between the (-,1) band and the yrast band.
[c]The errors are those determined by the subroutine MINOS discussed in *Appendix C.*

Table 4.4: The lifetimes of yrast states obtained from the total projected data (TPD), gated below data (GBD) and gated above data (GAD).

J_i^π	TPD[a) $\tau(\text{ps})$[c)	GBD[a) $\tau(\text{ps})$[c)	GAD[b) $\tau(\text{ps})$[c)
2^+	164^{+6}_{-7}		173^{+16}_{-16}
4^+	$10.9^{+1.2}_{-0.9}$		$9.4^{+1.0}_{-0.9}$
6^+	$2.3^{+0.2}_{-0.2}$	$3.2^{+0.7}_{-0.7}$	$2.4^{+0.4}_{-0.4}$
8^+	$1.8^{+0.2}_{-0.2}$	$1.4^{+0.4}_{-0.3}$	$2.4^{+1.6}_{-1.9}$
10^+	$1.6^{+0.2}_{-0.2}$	$2.0^{+0.4}_{-0.5}$	
12^+	$0.9^{+0.1}_{-0.2}$	$1.3^{+0.3}_{-0.4}$	
14^+	$0.5^{+0.4}_{-0.4}$	$1.1^{+0.4}_{-0.4}$	
16^+	$2.7^{+0.5}_{-0.9}$	$4.4^{+0.4}_{-0.5}$	
18^+	$1.5^{+0.5}_{-0.7}$	$1.7^{+1.9}_{-0.5}$	
20^+	< 1.9	< 0.7	

[a)]See footnotes [a)] and [b)] in table 4.3. Results are unweighted averages of the two columns discussed there.
[b)]Unweighted averages of the results determined from the sum of spectra gated by the transitions above that of interest. See text for discussion.
[c)]See footnote [c)] in table 4.3.

procedures reveals that the standard modelling alone was obviously able to account for the yrast fits in a satisfactory manner. For our accepted final lifetime values for the TPD and GBD on the yrast sequence, a normal average of these two sets of results was taken and these are shown in columns 2 and 3 of table 4.4, respectively.

In the analyses of the yrast band from gates set on transitions above those of interest, we have taken three different sums of gates: the 8^+, 10^+, $\cdots$, 30^+; the 10^+, 12^+, $\cdots$, 30^+; and, the 12^+, 14^+, $\cdots$, 30^+ transitions. These three different sets of GAD were used to analyze the lifetimes of states from 2^+ to 8^+. The 2^+, 4^+ and 6^+ states were analyzed in the sum of gates from 8^+ to 30^+ and the 2^+ through 8^+ states from the sum of 10^+ to 30^+ states. Although the GAD does not have a direct perturbation from side feeding into the states of interest, there still remains a side feeding in the gating transitions. This secondary effect is most bothersome when fitting the decay for the transition just below the first gate. To avoid this

problem, the transitions 2^+, 4^+, 6^+ and 8^+ were also fitted in the sum of gates from 12^+ to 30^+. However, this secondary effect was taken into account by modelling the two-step side feeding into the top member of the cascade studied. Of course, no other side feeding was allowed. In the figure 4.18 sample decay curves of the states 4^+, 6^+ and 8^+, based on GAD, are shown. Again, the normal average values from the results of these three sets of GAD were calculated and were used as final results for gated above analyses. They are shown in column 4 of table 4.4.

Finally, weighted means of the lifetime results between TPD and GAD as well as GBD and GAD and unweighted averages between TPD and GBD results have been taken. Here, because of the different side feeding effect, the results from GAD were considered independent of those from TPD and GBD. These values are shown in column 2 of table 4.5. Column 3 lists the corresponding transition quadrupole moments Q_t obtained from the reduced transition probabilities according to the eq.'s $3.29 - 3.32$ given in subsection 3.3.3. These, the accepted Q_t values for the yrast sequence, are shown as a function of spin in figure 4.19 (filled circles).

Table 4.5 also presents a summary of the lifetimes and intensities of the sidefeeding transitions to the yrast states determined from the TPD and GBD. Recall eq.'s (4.2) and (4.3) and relations [1], [2] and [3] there: In most cases the two sidefeedings behaved according to the relation [1] and usually so that the time of maximum rate t_m (see eq. (4.2)) was reached rapidly after $t = 0$. The situation was similar for the cases corresponding to the relation [2]. However, longer-lived components are dominating in both cases and were used as a sidefeeding time for a particular yrast transition. The sidefeeding intensities are the percentages of the fitted feeding intensity to the intensity of the depopulating γ ray. They represent initial populations. From eq. (4.3) one can see, when relation [3] is valid, that the maximum activity of B occurs after one mean life it has begun. In three level case it happens after two lifetimes etc... Average values of these almost equal lifetimes were used as sidefeeding times for the 6^+ and 8^+ transitions in GBD, as mentioned before. Although there are some inconsistencies in the sidefeeding lifetimes as determined in the two sets of coincidence data, TPD and GBD, it can be seen from table 4.4 that the extracted lifetimes of the yrast transitions are not affected appreciably by these differencies. This is probably due to the fact that the side feeding intensities are generally small compared to the direct feeding from higher spin yrast states. One may also notice, that the side feeding lifetimes are seen to be comparable to the lifetimes of yrast states indicating that the side feeding proceeds through pathways with similar collectivity.

Table 4.5: Final results of the yrast transitions. Lifetimes and quadrupole moments as well as sidefeeding times and intensities from TPD and GBD are given.

J_i^π	$\tau^{a)}$(ps)	$Q_t^{a)}$(eb)	TPD		GBD	
			$\tau_{feed}^{b)}$(ps)	$I_{feed}^{c)}$(%)	$\tau_{feed}^{b)}$(ps)	$I_{feed}^{c)}$(%)
2^+	165_{-6}^{+6}	$5.8_{-0.1}^{+0.2}$	91	5	-	-
4^+	$10.3_{-0.6}^{+0.8}$	$5.9_{-0.2}^{+0.2}$	25	14	-	-
6^+	$2.6_{-0.3}^{+0.3}$	$7.4_{-0.4}^{+0.5}$	140	23	80	16
8^+	$1.6_{-0.3}^{+0.4}$	$8.2_{-0.8}^{+1.0}$	24	35	19	26
10^+	$1.8_{-0.4}^{+0.3}$	$6.6_{-0.5}^{+0.7}$	6	8	5	14
12^+	$1.1_{-0.3}^{+0.2}$	$7.0_{-0.6}^{+1.0}$	1	13	1	23
14^+	$1.1_{-0.4}^{+0.4}$	$7.3_{-1.1}^{+1.6}$	$d)$	-	7	19
16^+	$3.6_{-0.7}^{+0.5}$	$5.0_{-0.4}^{+0.8}$	2	29	$d)$	-
18^+	$1.6_{-0.6}^{+1.2}$	$4.6_{-1.0}^{+1.3}$	1	39	5	34
20^+	< 1.3	> 4.2	$e)$	-	$e)$	-

$a)$For the 2^+ and 4^+ states the results are weighted means from the TPD and GAD fits and for the 10^+ to 20^+ states unweighted arithmetic averages from the TPD and GBD fits. For the 6^+ and 8^+ states the results represent weighted averages of two values where the first is an unweighted average of the results of TPD and GBD and the second is an unweighted average of GAD results (c.f. text).

$b)$The uncertaitities in the feeding times are about 50%.

$c)$Intensities are the precentages of the unobserved feeding intensity to the intensity of the yrast transition.

$d)$The program was unable to produce a satisfactory fit for this side feeding transition.

$e)$Modelled by the rotational band as well as the feeding cascade (for details, see the text).
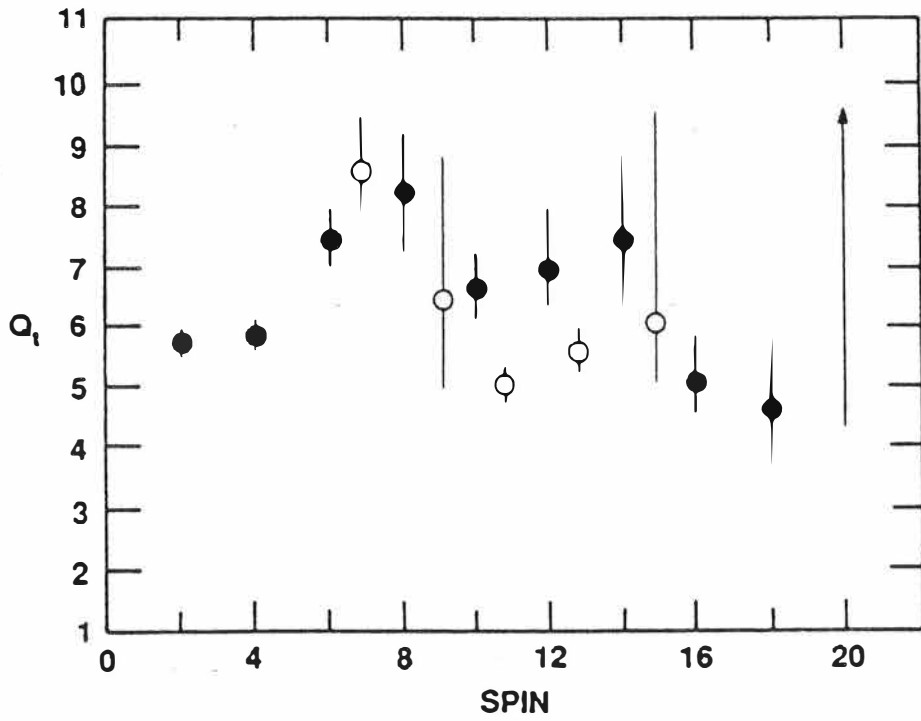
Figure 4.19: Transition quadrupole moment Q_t against spin value for the yrast($\bullet$) and $(-, 1)$ side band ($\circ$) transitions.
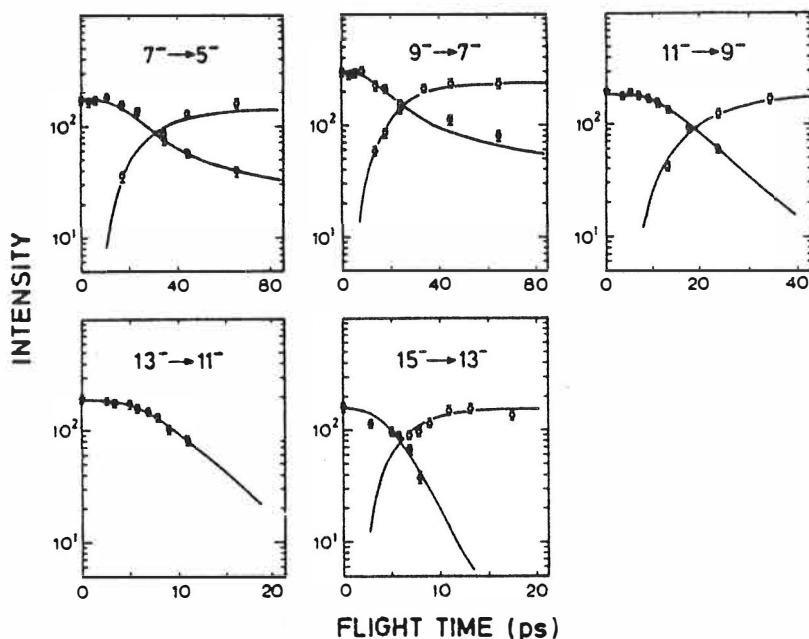
Figure 4.20: Decay curves for the $(-,1)$ side band transitions. The data is obtained from total projection spectra.

4.3.4 Results for the $(-,1)$ Side Band

The $(-,1)$ band was analyzed using the total projection data (TPD). Because of the long-lived side feeding component (>100 ps) and $\sim38\%$ feeding intensity to the 9^- state, the transitions $15^- \rightarrow 13^-$, $13^- \rightarrow 11^-$, $11^- \rightarrow 9^-$ and $9^- \rightarrow 7^-$, $7^- \rightarrow 5^-$ were fitted separately. The three uppermost transitions were fitted first and the results were used as starting values for the fit of the two lower ones. It is true that the best-fit side feeding time for the 9^- state is rather long, but starting from much shorter feeding times does not change significantly the inferred lifetime and the initial values of direct cascade feeding. A MINOS analysis was performed for both fits. In figure 4.20 decay curves of the $(-,1)$ sideband states are shown.

The results of the $(-,1)$ sideband transitions (lifetimes and Q_t values) as well as the sidefeeding times and intensities are given in table 4.6. Also, transition quadrupole moments have been plotted against spin values in figure 4.19 (open circles). Partial lifetimes and $B(E1)$ values of the transitions between this and yrast band are shown in table 4.7. For comparison, values extracted from TPD as well as from GBD are shown. In calculations the

Table 4.6: Lifetimes τ and transition quadrupole moments Q_t as well as side feeding times and intensities for the odd-spin negative parity $(-,1)$ band.

J_i^π	E_γ(keV)	τ(ps)	Q_t(eb)	$\tau_{feed}^{a)}$(ps)	$I_{feed}^{b)}$(%)
7^-	322.0	$9.2^{+1.7}_{-1.7}$	$8.6^{+0.9}_{-0.7}$	$c)$	-
9^-	396.2	$5.9^{+4.2}_{-2.9}$	$6.4^{+2.5}_{-1.5}$	106	38
11^-	391.2	$9.9^{+0.8}_{-0.8}$	$5.0^{+0.2}_{-0.2}$	24	<1
13^-	428.7	$4.9^{+0.9}_{-0.7}$	$5.6^{+0.4}_{-0.4}$	7	16
15^-	516.9	$1.7^{+0.8}_{-1.0}$	$6.0^{+3.5}_{-1.0}$	2	$100^{d)}$

$^{a)}$See footnote $^{b)}$ in table 4.5.
$^{b)}$See footnote $^{c)}$ in table 4.5.
$^{c)}$The program was unable to produce a satisfactory side feeding fit. The result obtained without side feeding (c.f. level scheme).
$^{d)}$Modelled by a 3-member rotational band (see the level scheme).

fitted branching ratios have been used. Reduced transition probabilities B(E1) were obtained by using the formula[51] (eq. (3.25))

$$\lambda(E1) = 1.589 \times 10^{29} E^3 B(E1) ps^{-1}, \qquad (4.4)$$

where $B(E1)$ is given in units of $e^2 b$.

For the transitions $5^- \rightarrow 6^+$ and $5^- \rightarrow 4^+$ it was only possible to get their relative B(E1) values determined from their branching ratios, i.e. the ratio $B(E1, 5^- \rightarrow 6^+)/B(E1, 5^- \rightarrow 4^+)$.

Table 4.7: The partial lifetimes $\tau_{part.}$ and calculated B(E1) values (in single particle units) for the interband transitions extracted from TPD and GBD.

$J_i^\pi \to J_f^\pi$	E_γ(keV)	TPD		GBD[a]	
		$\tau_{part.}$(ps)	B(E1)/B(E1)$_{s.p.}$	$\tau_{part.}$(ps)	B(E1)/B(E1)$_{s.p.}$
$9^- \to 10^+$	350.8	38 ± 24	1.9×10^{-4}	48 ± 30	1.5×10^{-4}
$7^- \to 8^+$	453.5	13 ± 2	2.7×10^{-4}	11 ± 2	3.1×10^{-4}
$7^- \to 6^+$	924.1	29 ± 10	1.4×10^{-5}	27 ± 9	1.5×10^{-5}
$5^- \to 6^+$	601.7		$\frac{B(E1,5^-\to 6^+)}{B(E1,5^-\to 4^+)}$		$\frac{B(E1,5^-\to 6^+)}{B(E1,5^-\to 4^+)}$
$5^- \to 4^+$	1049.8		$=7.4$[b]		$=7.3$[b]

[a] Determined from spectra gated by the sum of transitions 2^+ and 4^+.

[b] For these transitions it was only possible to get the ratio of B(E1) of $5^- \to 6^+$ to that of $5^- \to 4^+$ from their branching ratios.

Chapter 5

Discussion

5.1 Experimental Interpretations

5.1.1 Band-Crossings and Alignments

The experimental aligned angular momenta and Routhians for the five bands in ^{172}Os were calculated (eq.'s (2.47) and (2.46)) and are shown in figures 5.1a) and 5.1b), respectively [6]. The corresponding alignment plot for ^{173}Os is shown in figure 5.2. The plots are labeled by their signature quantum numbers (π, α). All values are deduced from the experimental data.

For the reference, eq. (2.44), the Harris parameters $\mathcal{J}_0^{(1)} = 15\hbar^2 MeV^{-1}$ and $\mathcal{J}_1^{(1)} = 90\hbar^4 MeV^{-3}$ were adopted. The convention for labelling the quasiparticles is given in table 2.1 in subsection 2.2.2. Note that the A, B, C and D designations are the lowest lying quasineutron orbitals from the $i_{13/2}$ shell and the E and F designations are the lowest lying quasineutron orbitals from the $h_{9/2}$ shell.

At low frequency, the yrast band is the zero quasiparticle vacuum configuration. From the composite structure of the yrast line in the frequency range of $\hbar\omega = 0.22$ to 0.28 MeV, one may conclude that there are probably strong interactions between crossing levels and that they involve multi-quasiparticle configurations. A discussion of the alignment processes occurring in the yrast sequence through this frequency range will be presented later. At a crossing frequency of 0.26 MeV an increase in alignment of about $10.5\hbar$ units can be seen. This is considerably more alignment than

---

[6]There, the more general definition i_x for i_1 is used
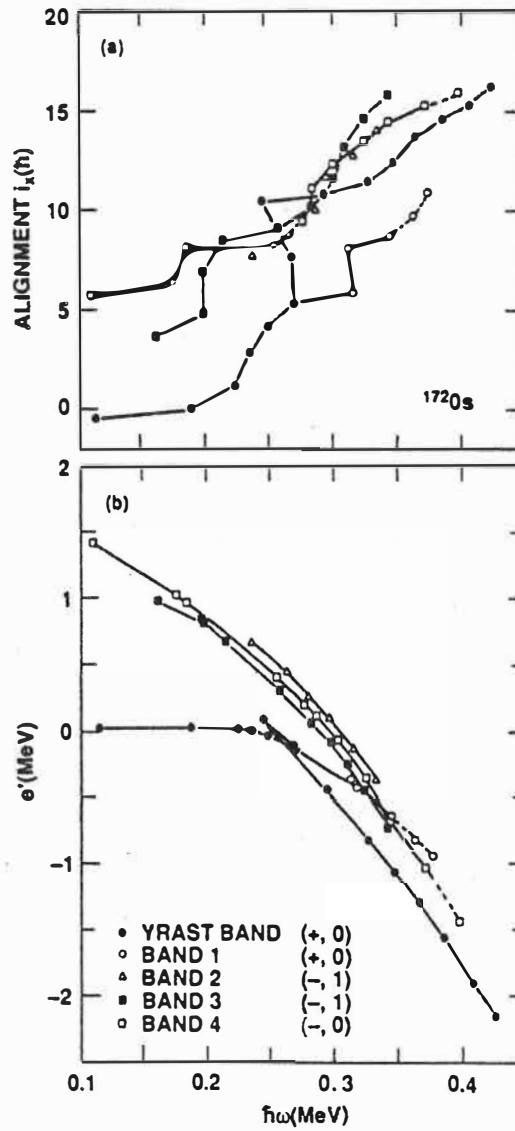
Figure 5.1: a) Aligned angular momenta (i_x) and b) Routhians for the bands in ^{172}Os.
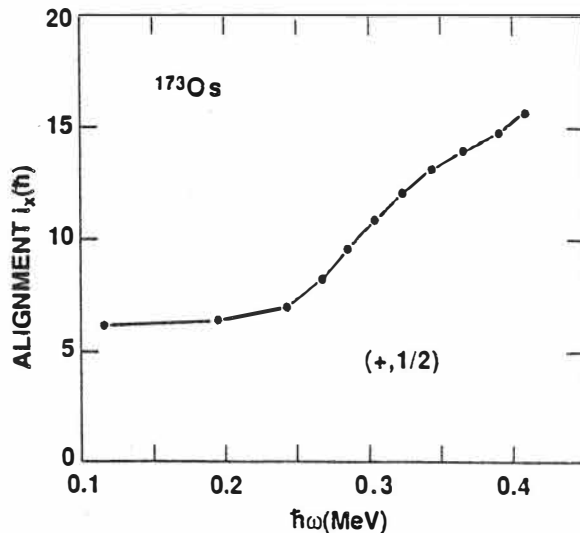
Figure 5.2: Aligned angular momentum (i_x) for the band in ^{173}Os.

is extracted from the experimental data for the AB crossing in the other isotones of ^{172}Os[65][66][67].

In figure 4.19 the plot of the transition quadrupole moment (Q_t) as a function of spin for the yrast members of ^{172}Os were shown. Noticeable features there are that the trend in the ground band shows indications of centrifugal stretching, that is increasing Q_t, proportional to β_2 in eq. (3.33), vs. increasing spin/frequency. This is not yet surprising since many of the light rare-earth nuclei are known to be "soft" to centrifugal distortion up to the first bandcrossing. But here, interestingly, one can see two separate low spin stretchings; an "anomalous" stretching at spins 6^+ and 8^+ and a "normal" stretching at spins 10^+, 12^+ and 14^+. Or, in other words, the normal stretching is disturbed by some strong interaction. Moreover, the high-spin states ($> 14^+$) have lower Q_t values than do the 2^+ and 4^+ states. It is pertinent to ask whether this is simply due to the alignment of quasiparticles or whether there are also some other processes operating. These questions will be discussed below.

Based on the experimental data and systematics, it is concluded that the low-frequency members of the negative parity bands are probably two-quasineutron configurations, with the $\alpha = 1$ band (band 3) having the AE

configuration and the $\alpha = 0$ band (band 4) having the AF configuration. One can see the signature splitting between the AE and AF configurations in figure 5.1b). At $\hbar\omega = 0.28$ MeV, both of these bands may be crossed by a four-quasineutron configuration in which the BC quasineutrons have aligned, giving the $\alpha = 1$ band the AEBC configuration and the $\alpha = 0$ band the AFBC configuration. In each case, about $7\hbar$ units of alignment gain is produced by the BC crossing, and this value agrees closely with that from the BC crossing of the AE configuration in ^{170}Os[10].

The data on band 2 were not of sufficient quality to provide spin assignments. However, from the observed decay pattern of this band and the known systematics, one could speculate that it is the continuation of the $(-, 1)$ octupole band above the point at which it is crossed by the AE band. The decay pattern is consistent with the assumption that the 2846 keV level has spin 11^-. Hence, whereas K values of 0 were assigned to all of the other bands, it is assumed that band 2 has K=2 for the plots in figure 5.1. The full alignment gain from this crossing cannot be assessed, but it appears to be greater than $5\hbar$.

A comparison of the aligned angular momentum shown for ^{173}Os in figure 5.2 with that for the $(\pi, \alpha) = (+, 1/2)$ bands in its neighboring odd-mass isotones reveals a somewhat larger alignment gain at high spin in ^{173}Os (c.f. e.g. [11]). One can speculate that this may result from alignment contributions from protons in the latter case.

5.2   Theoretical Interpretations

The high spin behaviour of the discussed osmium nuclei is expected to depend on shape evolution and possibly shape coexistence effects. For this reason, the first step in the theoretical analysis involved calculations of the total energy surfaces of the ^{172}Os for the four assigned parity signature combinations (figure 4.13) as a function of spin. These have been performed by using the generalized Strutinsky shell correction approach[68] (see also the reference [25] and references therein) with the deformed Woods-Saxon potential. The universal parameterization of this potential which, on the average, performs very well in the description of high spin phenomena was used (subsection 2.2.2 and *Appendix B*).

5.2.1   Shape Coexistence and Evolution

The richness of the shape phenomena in this mass region is illustrated in figures 5.3a) and b) where some of the total energy surfaces for ^{172}Os are shown. The coordinate system is that of the standard (β, γ) plane with the convention given in the subsection 3.3.3. Figure 5.3a) represents the total energy surfaces for selected spin values having total parity $\pi = +1$ and signature exponent $\alpha = 0$. This figure reveals that there are nine pronounced shape configurations predicted in ^{172}Os, ranging from moderately deformed ($\beta_2 \sim 0.2$) to the hyperdeformed[26] ($\beta_2 \sim 1.0$) minima. Included in these are: Two triaxial superdeformed minima with $\gamma \sim \pm 20^0$ and $\beta_2 \sim 0.5$; yet another pair superdeformed/hyperdeformed configurations with similar triaxialities at $\beta_2 \sim 0.8$; and finally, two axially symmetric hyperdeformed minima with well-deformed separation potential barriers at $\beta_2 \sim 1.0$ and $\beta_2 \sim 1.2$.

Here we limit our discussion only to the moderately deformed configurations, with β_2 varying between ~ 0.18 and 0.22, which are represented with the blue colors in the maps for spins I$^\pi$ = 6$^+$, ..., 40$^+$ (the white-edged "oval" in the black-and-white figure). The shape evolution related to these minima has interesting consequences for the comparison of theory and experiment, as discussed below. The most important shape change in the moderate-deformation regime corresponds to the switch from $\gamma \sim -16^0$ at spins below the backbending limit to increased γ-values, triaxiality decreased down to $\gamma \sim -6^0$, at spins above the backbending i.e. I $\sim 18\hbar$ and higher (in the black-and-white version this is seen as a small shift in the center of gravity of the "oval" towards the $\gamma = 0^0$-axis). This change is accompanied by a slight shrinking of the nucleus and, according to the calculations, is enforced by increasing alignment.
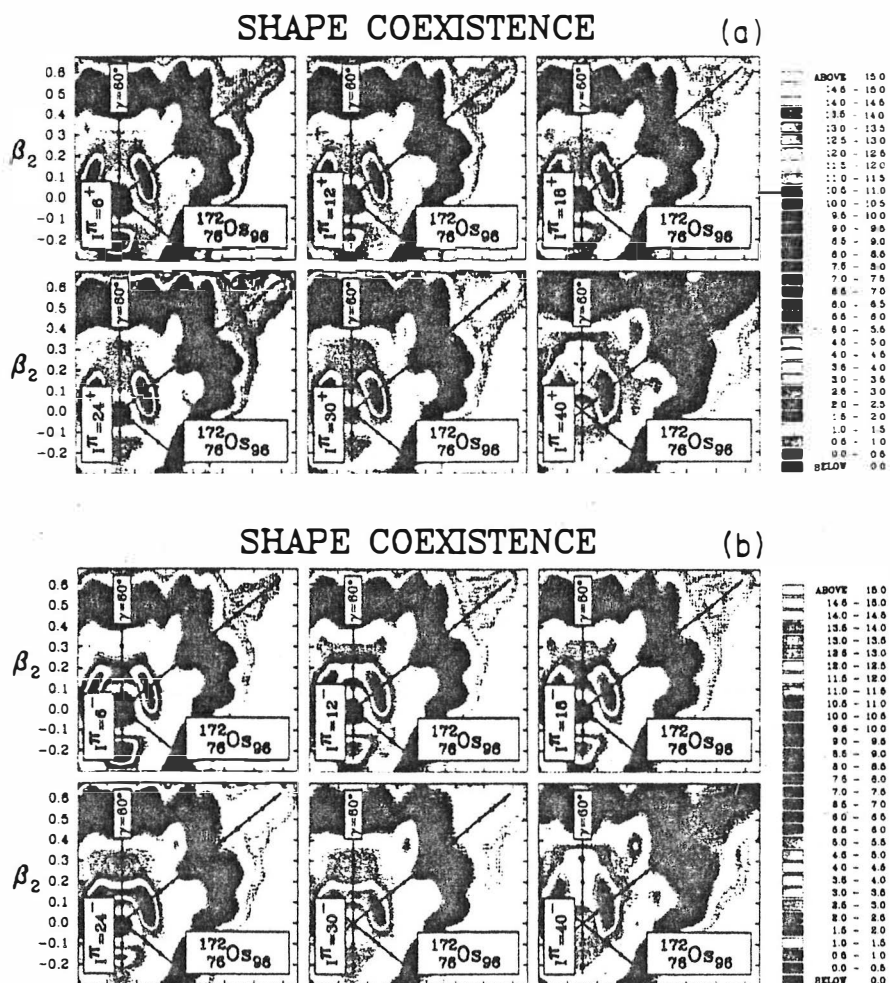
Figure 5.3: a) Total energy surfaces for positive parity configurations of ^{172}Os calculated with the extended Strutinsky method (see text). b) Similar to that in a), but for some negative parity configurations.

For comparison and for illustration of the typical configuration dependence of the discussed shape properties, the negative parity landscapes are shown in Figure 5.3b) for spins $I^\pi = 6^-$, 12^-, 18^-, 24^-, 30^- and 40^-. Two properties deserve noticing. First, the negative parity configurations with minima at $\beta_2 \sim 0.2$ do not undergo the shape change discussed above in the context of the positive parity states (the minima of the $\pi = -1$ states remain at $\gamma \sim -16^0$ to -20^0). Second, the multi-minima of the total-energy landscape are in some instances even more pronounced (some separating barriers even more elevated) than found in the positive parity case.

5.2.2   Microscopic Calculations

Having determined the potential energy surfaces (and their associated deformation parameter values) for ^{172}Os, it is next proceeded to examine the microscopic effects giving rise to the experimental observations. For this, Hartree-Fock-Bogoliubov Cranking (HFBC) calculations were carried out with a Woods-Saxon potential and both particle-number projection and the effects of pairing were incorporated (see subsection 2.2.3). Some of the specific questions one wished to answer are: 1) What are the quasineutron band crossings that give rise to the complex structure in the moment of inertia? 2) What role do the protons play below rotational frequencies of $\hbar\omega \sim 0.35$ MeV? 3) What are the interaction strengths in these band crossings? and 4) How much is the pairing diminished at these rotational frequencies and how does it affect the properties of ^{172}Os?

The single-particle neutron levels were extracted as a function of the quadrupole deformation (β_2) and these are shown in figure 5.4a). It illustrates the orbitals in the vicinity of N=96. The relevant low-level density areas are shaded. The calculated single-particle proton levels in the vicinity of Z=76 are shown in figure 5.4b). The projection quantum numbers K^π are also indicated. The positions of the three lowest, and also most important for the alignment properties, intruder $i_{13/2}$ orbitals are marked explicitly. These figures indicate that the structure of the total wave functions of the yrast and low-lying states in ^{172}Os is determined by two characteristic factors. First, with the neutron Fermi level λ_ν positioned in between the highly alignable orbitals labeled $i_{13/2}$, $K = 3/2$ and $i_{13/2}$, $K = 5/2$, there is a tendency for a strong interplay effect stimulated by the pairing forces (via the pairing occupation factors) of at least three $\nu i_{13/2}$-related configurations. (Note that an independent analysis in terms of the three-band mixing approximation can be found in references [4] and [10]). Second, particularly well-pronounced proton-deformed shell closures appear at Z=74, 76 and 78. This chain gives rise to the noticeably lowered single-particle

level density and tends to stabilize the deformation in Os (Z=76) at $\beta_2 \sim$ 0.18.

It is instructive to illustrate the influence of rotation on the shell effects and alignment effects in the case where pairing correlations are present and in that where they are absent. We begin with the neutron single-particle Routhians (no-pairing case) plotted as a function of rotational frequency in figure 5.5a). The dominating role of various members of the $\nu i_{13/2}$ orbital is stressed by the dark solid lines and by showing the associated orbital identification. The deformation parameters used in the calculations are: $\beta_2 = 0.185$, $\beta_4 = 0.010$ and $\gamma = 0$ and are also shown at the top of the figure. The signature-split orbitals are marked with the conventional symbol of $i_{13/2}$. The tendency for the strong Coriolis-mixing among several consecutive $\nu i_{13/2}$ orbitals can be inferred from the strong repulsion among the Routhians. The strong interaction (mixing) between the consecutive members of the intruder orbital is easy to see at the "crossing frequencies" which correspond roughly to $\hbar \omega_c \sim 0.07$ MeV ($K = 3/2$ with $K = 5/2$ orbital crossing), $\hbar \omega_c \sim 0.22$ MeV ($K = 5/2$ with $K = 7/2$ orbital crossing), $\hbar \omega_c \sim 0.35$ MeV ($K = 7/2$ with $K = 9/2$ orbital crossing), etc $\cdots$. According to the calculations with the universal parametrization of the Woods-Saxon potential, the proton orbital most active in the alignment process has the quantum labels $h_{9/2}$, $K = 1/2$ and crosses the Fermi level for Z=76 at $\hbar \omega \sim 0.4$ MeV in the zero-pairing illustrated Routhians of figure 5.5b). It arrives there after a number of crossings with the other negative parity levels visible in the figure. The two orbitals predicted to play a dominant role at rotational frequencies $\hbar \omega > 0.5$ MeV are indicated explicitly.

Illustration of the effect of the pairing coupling scheme is given in figure 5.6a) where the Routhians of the $i_{13/2}$ quasineutrons with K quantum numbers of 5/2, 3/2 and 1/2 are shown. A most striking feature of these Routhians is the strongly repulsive interaction between these low-Ω orbitals and the narrow frequency range over which this takes place. As noted in figure 5.6a), the AB crossing occurs first at $\hbar \omega_c \sim 0.25$ MeV, followed very closely by the BC and AD crossings at $\hbar \omega_c \sim 0.26$ MeV. One should remember that the symbols used here have only an asymptotic meaning: The K-quantum number becomes exact in the $\omega \rightarrow 0$ limit, while the shell model notations (e.g. $\nu i_{13/2}$ or $\pi h_{9/2}$ symbols) acquire an exact meaning in the limit where the deformation goes to zero. Also, in the triaxially-deformed nuclei the K-quantum number loses validity, even for non-rotating nuclei ($\omega = 0$). Further, the bottom frames of figure 5.6a) and b) show the properties of the pairing gap Δ calculated using the HFBC theory, but without particle number projection. In contrast to figure 5.6a), all the quasiparticle levels are illustrated for the protons in figure 5.6b). Again, one may note

Figure 5.4: a) Calcu-
lated   single
particle neutron spec-
trum. The three low-
est intruder orbitals
are marked explicitly.
b) Same for the pro-
tons.   The strongly
down sloping orbital
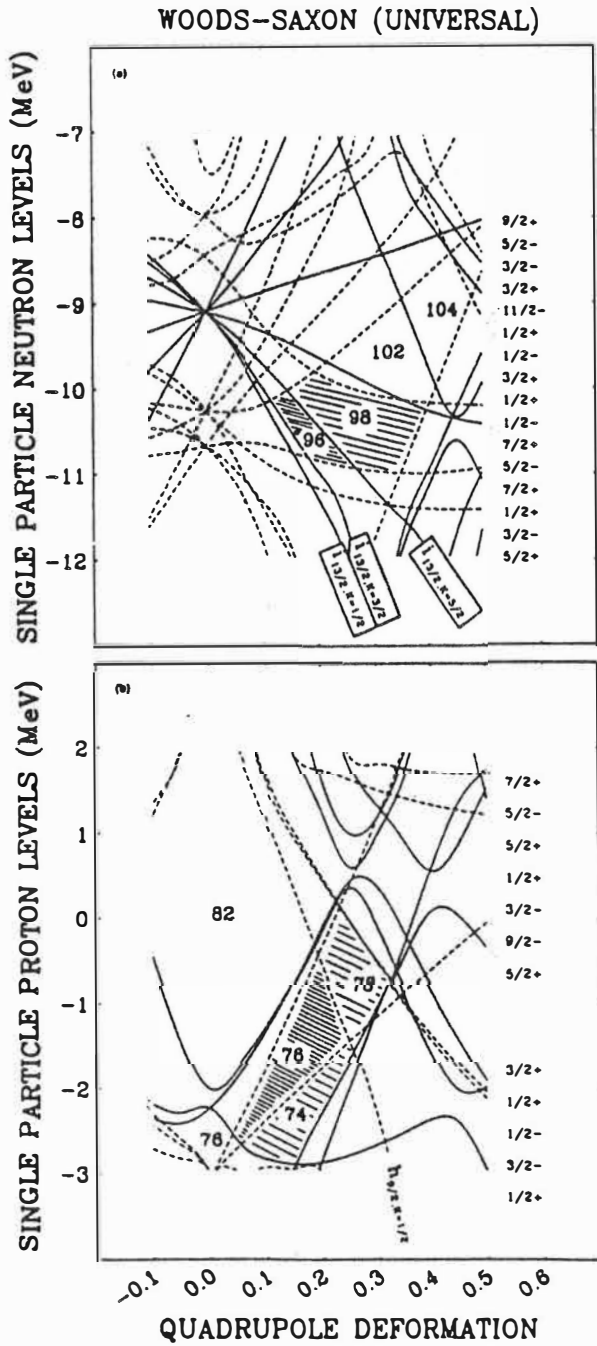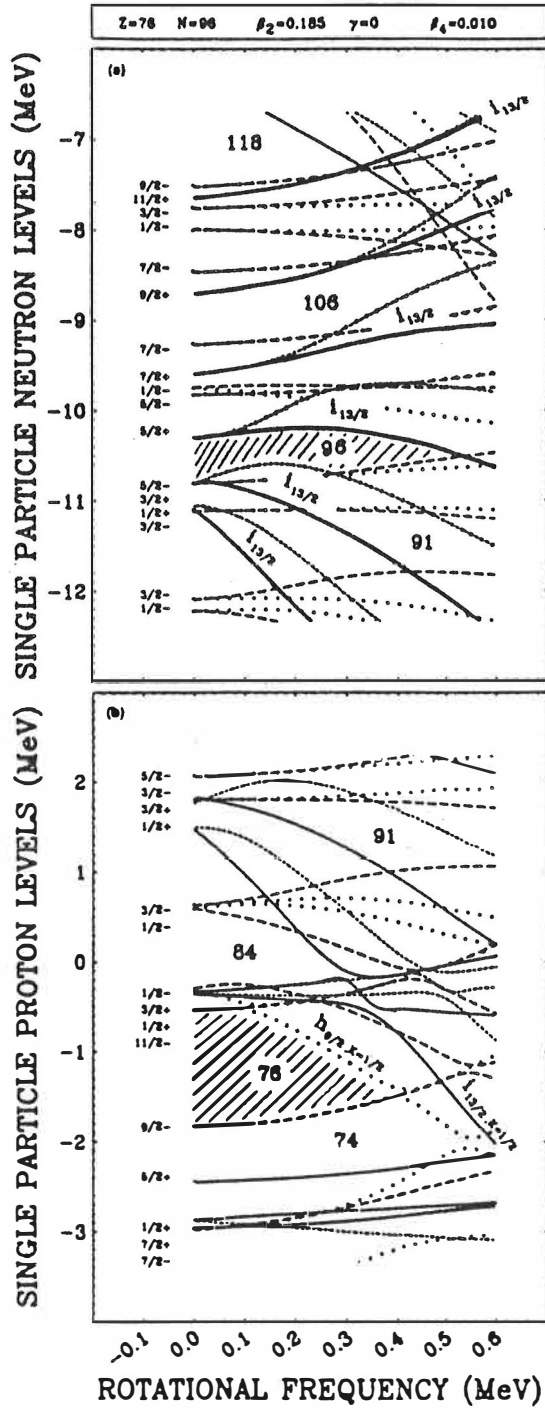is labeled explicitly.

WOODS–SAXON (UNIVERSAL)

Figure 5.5: a) Neutron single-particle Routhians as a function of the rotational frequency. b) Similar to that in a) but for the protons.

that the highly alignable negative-parity orbital has the structure of the one labeled $K^\pi = 1/2^-$ rather than $9/2^-$. This is because of the sequence of two level crossings at $\omega_{cr1} \sim 0.05$ MeV and $\omega_{cr2} \sim 0.4$ MeV. Based on this and on the figure 5.5, it must be concluded that it is unlikely that the $h_{9/2}$ quasiprotons play a significant role in the properties of the yrast sequence below $I \sim 20$.

Since the triaxialities involved in the following analysis are relatively moderate and since, as we deduced, the overall character of the quasiparticle diagram is not strongly influenced by replacing the moderately small γ values by $\gamma = 0^0$, for the qualitative illustration purposes the $\gamma = 0^0$ plots are used. In the quantitative analysis, however, the $\gamma \neq 0^0$ configurations are explicitly used.

While a unique cranking model interpretation of strongly interacting bands may sometimes be ambiguous, especially in the cases of shape coexistence and shape changes, the negative parity bands can relatively safely be attributed to the AE and AF configurations as illustrated in figure 5.7 where we show the calculated low-lying, negative-parity quasiparticle orbitals for ^{172}Os. This can be supported further by the very small signature splitting predicted by theory for these two bands, especially in the $\hbar\omega \sim 0.20$ MeV frequency range. Note the increase in signature splitting above this frequency, both in theory and experiment (c.f. figure 5.1). The deformation corresponds to the low-spin part of the yrast spectrum with $\beta_2 \sim 0.21$.

5.2.3   Decline of Pairing

It is an inherent part of the pairing self-consistent calculations to produce the prediction of the average pairing behaviour as a function of rotational frequency (and the configuration changes induced by rotation). According to the results in figures 5.6a) and b), the neutron pairing correlations are strongly diminished over the frequency range $\hbar\omega \sim 0.2$ to 0.3 MeV. This, according to the Hartree-Fock-Bogoliubov approach, is induced by increasing alignment of the consecutive configurations originating from $\nu i_{13/2}$, $K = 5/2$, $7/2$ and $9/2$ orbitals. The corresponding effect in the proton phase is predicted to occur at much higher frequencies ($\hbar\omega_c \sim 0.41$ MeV) as the result of the $\pi h_{9/2}$, $K = 1/2$ orbital alignment, followed at $\hbar\omega \sim 0.55$ MeV by the $\pi i_{13/2}$, $K = 1/2$ alignment.

The illustration of the pairing changes due to rotation is given in the bottom parts of figures 5.6a) and b) in terms of the so-called static pairing gaps Δ_ν, Δ_π. However, at high rotational frequencies, the usually applied HFBC approximation breaks down, and the only self-consistent solutions of the

Figure 5.6: a) The quasiparticle orbitals for the neutrons at N=96 when pairing effect has been included. b) Similar to that in a), but for the protons.
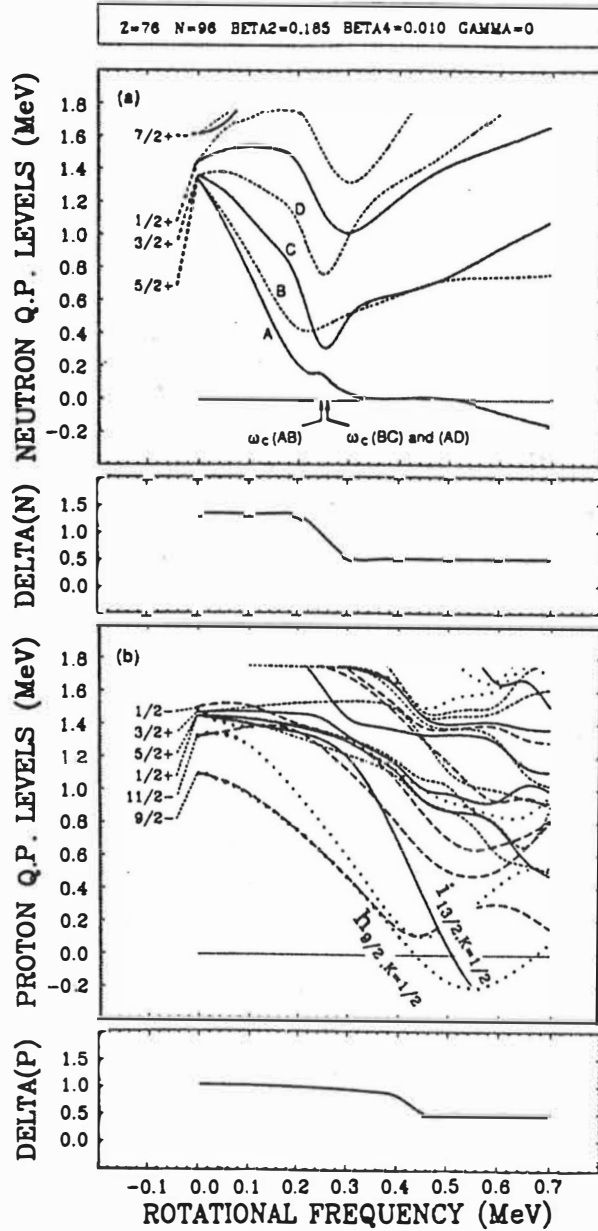
Figure 5.7: Neutron quasiparticle orbitals for the negative-parity bands. The low-lying negative-parity quasiparticle orbitals are labeled as E and F.

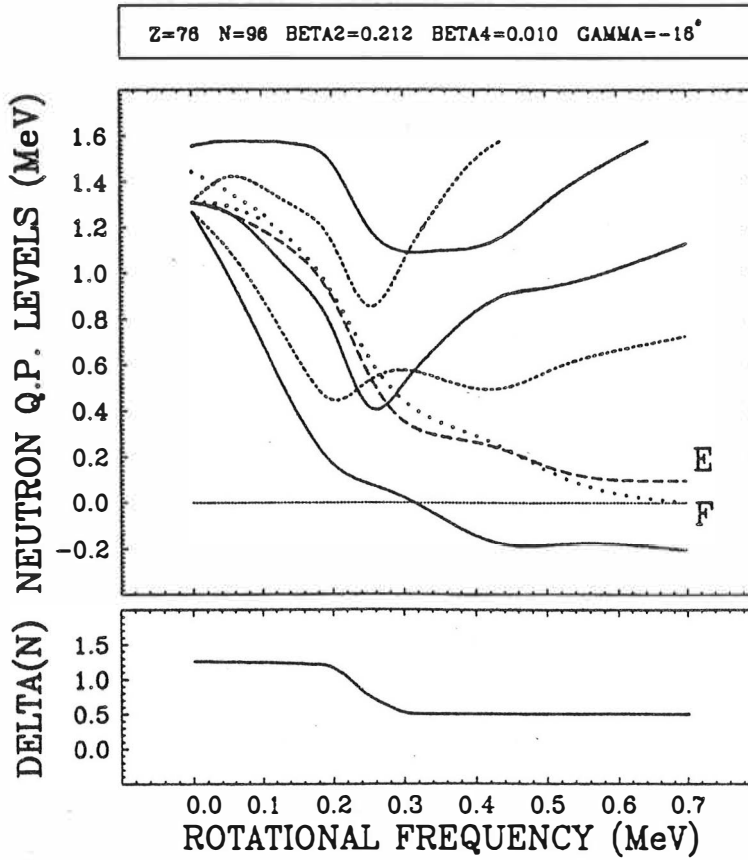HFBC equations are trivial (Δ=0). The alignment properties can still be well imitated in the high$-\omega$ regime if one of the HFBC equations, usually called the gap equation, is dropped (see reference [69]). Then the Fermi level is found by using an iterative procedure. This is done by solving only the so-called particle number equation at a constant Δ value, typically of the order of 300 to 500 keV. For this reason, in the results of figures 5.6a) and 5.6b), the high$-\omega$ limit corresponds to fixed Δ values. Thus, in the corresponding regime the quasiparticle diagrams may still be attributed a physical interpretation.

5.3 Systematical Features

An inspection of the figure 5.6a), which shows the positive-parity quasineutron Routhians, which are the active aligning orbitals at low spin in this mass region, reveals a rather complicated behaviour in the frequency range $\hbar\omega = 0.2$ to 0.3 MeV. These alignments originating from the levels labeled K=5/2, 3/2 and 1/2 are clearly strongly disturbed by mutually repulsive interactions. The first important two-quasiparticle excitations coupling to $(\pi,\alpha) = (+,0)$ are the AB, BC and AD crossings. In figure 5.6a) it can be seen that all of these crossings occur within a narrow frequency range $(\Delta\omega_{cr} \sim 0.04$ MeV).

Because of the strong mixing expected between these configurations, it may be somewhat difficult to give a unique interpretation to each of the nearly degenerate crossing frequencies. However, it is possible to get some idea about this complex situation for the $(+, 0)$ configurations in ^{172}Os by using the simple standard band-crossing picture. The explanation proposed in this section contains the essence required in understanding the two anomalies at low frequencies observed in the ^{172}Os moment of inertia.

5.3.1 The $\omega-$Systematics

In this mass region, the first crossing of the ground-state rotational band is by the most alignable pair of $i_{13/2}$ neutrons (denoted as the s or AB band). In most cases it has not been possible to observe the continuation of the ground band through this first crossing. In a few cases, however, this continuation has been followed (e.g. see references [70]$-$[73]). In these it was found that another crossing occurs soon after the first AB crossing and this was attributed to the BC and AD alignments. In ^{172}Os we have also observed the continuation of the ground band through the first crossing (AB) region (labeled band 1 in figure 4.13). In figure 5.1 the high alignment

gain seen in these states indicates that the BC (or BC and AD) alignments probably have already taken place and at a frequency very similar to the band crossings in the yrast sequence. In the negative-parity sidebands the BC crossing is seen at $\hbar\omega \sim 0.28$ MeV. It is interesting that the ground-BC (or BCAD) configuration changes occur at slightly lower frequency than the corresponding BC alignments in the negative-parity bands (e.g. AE→AEBC). This same situation was seen for ^{158}Er by Simpson et al. [71] and Riley (as referred to in [74]), where the frequency difference is $\Delta\hbar\omega \sim 0.03$ MeV.

Therefore, based on both the theoretical calculations and the experimental evidence, it is concluded that the first, second and third quasineutron alignments in ^{172}Os all occur very close together. Furthermore, the observed gradual gain in alignment with frequency of the negative parity bands implies that the BC alignment has an associated interaction strength which is large. As seen in figure 5.2, this is true also in ^{173}Os where a gradual gain in alignment through the frequency range of $\hbar\omega = 0.24$ MeV to 0.34 MeV has been observed. This behaviour, as in ^{172}Os, is attributed to the BC alignment. This large interaction strength is particularly important since it means that the "effective" band interaction region is spread over a wider frequency range. For example, in the case of ^{156}Dy below the AB crossing, it is seen that the curvature for the ground band and its continuation is quite smooth and similar to ^{172}Os. Riley et al. [70] attributed this behaviour to the strong interaction with the ground band from the BC(AD) crossing. Also, one may note that in the Dy, Er and Yb cases mentioned above, the BC interaction strength observed in the negative-parity side bands is of similar strength to that observed in the ground band continuation. It is quite interesting that Bengtsson [75] has just reported the results of his HFBC calculations for ^{180}Pt and reaches a somewhat similar conclusion for a possible interpretation of the behaviour in the low-frequency band crossing region for this nucleus. That is, he finds it possible to interpret the behaviour in the ^{180}Pt yrast sequence arising from neutrons only, with the four-quasiparticle configuration ABCD playing a significant role in the properties seen in the experimental data[76].

Yet one way to view this strong mixing region in ^{172}Os at $\hbar\omega \sim 0.2-0.3$ MeV is presented in figure 5.8. Here the excitation energy vs. I(I+1) is plotted for the ground band, for the s (or AB) band and for the continuation of the ground band. Straight line extrapolations are drawn through data points outside the strong-mixing region. Their close lying intersections with the ground band are consistent with our arguments above for multiple band crossings over a narrow frequency range. Note that the extrapolation of the so-called continuation of the ground band (which we term the BC(AD) band) comes very close and, in fact, crosses the s (AB) band at lower spin.
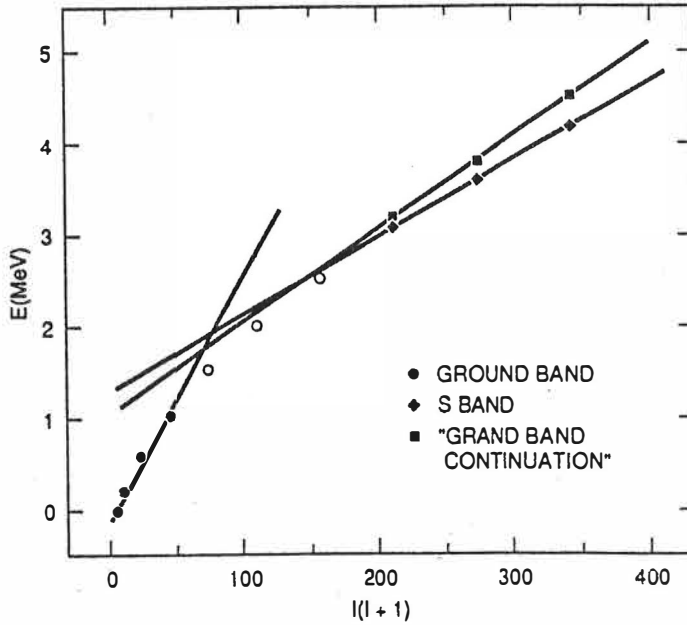
Figure 5.8: The energies of the three positive-parity bands of ^{172}Os as a function of I(I+1). The straight lines indicate the possible intersections of the non-interacting bands.

This does not happen in the Dy, Er and Yb cases.

This coming together of excited $(+, 0)$ quasiparticle bands at low spin and the observation of a strong interaction strength of the BC alignment leads to the following proposal for the explanation of the two low-spin anomalies in ^{172}Os. The first (AB), second (BC) and third (AD) band crossings occur at very similar frequencies ($\hbar\omega = 0.26 - 0.28$ MeV). However, because the interaction strength of the BC crossings is strong, the frequency range for the ground-BC(AD) crossing is smeared out sufficiently so as to perturb the ground band slightly below the AB-crossing region. This would explain the first anomaly in the yrast sequence at about spin 8 and $\hbar\omega = 0.24$ MeV. The second anomaly at $\hbar\omega = 0.26$ MeV is proposed to be the standard crossing by the s (AB) band.

Additional support for the above proposed band crossing picture is seen by examining the systematic tendencies in the evolution of the AB- and BC- band crossing frequencies as a function of neutron number for Hf, W and Os nuclei. This has been shown in figure 5.9. This comparison shows that the BC crossing frequency in the negative-parity bands decreases

markedly while the AB crossing frequency in the ground bands increases as the neutron number approaches N=98 and in addition to this there is a tendency of ω_{AB} approaching ω_{BC} at N~98. This pattern of crossings lends support to the calculated neutron quasiparticle diagrams in figures 5.6a) and 5.7. This merging of crossing frequencies is also correlated with an increase in interaction strength for the BC crossing. Therefore, one would expect that the unique extraction of quasiparticle alignments, particularly in the $(+, 0)$ sequences, becomes very difficult when several orbitals are aligning over a narrow frequency range. Results for the Os isotopes on either side of ^{172}Os support these proposals above. The fact that in ^{170}Os the BC crossing is higher in frequency[10] and has a smaller interaction strength is consistent with the lack of secondary anomaly in the yrast structure of that nucleus at low spin. However, in ^{174}Os one would expect a more complicated pattern, similar to ^{172}Os, but with the band crossings more smeared out. This is consistent with the experimental spectrum where the yrast band is observed[3] to have a gain in alignment over a very wide frequency range, $\hbar\omega = 0.2 - 0.4$ MeV. Contrary to the conclusions of Durell et al.[3] that there are no band crossing anomalies present in the ^{174}Os yrast band data, it can be shown in a plot of the second moment of inertia for this nucleus that there are, indeed, two anomalies present.[7]

In figure 5.10 an interesting comparison of the theoretical and experimental total aligned angular momentum along the yrast sequence of ^{172}Os is shown. The particle number projection variant of the HFBC approach has been used in the calculations (see ref.'s [69] and [78] and references therein). While the backbending region is never described well by the cranking method, outside this range the agreement appears very good. The low- and high-spin portions of the theoretical line correspond to the deformations calculated for the corresponding frequency ranges (see figure 5.3). The backbending region cannot be described by the cranking model and, therefore, the theoretical lines are interrupted in this region. Note that the structures in the experimental I vs. ω sequence are reproduced quantitatively by using a five percent adjustment in the neutron pairing gap (G=1.05) and a one percent adjustment in the proton pairing gap (G=1.01). Even the relatively detailed structures in the experimental curve find their analogues in theory as is shown in this figure. Note that this good agreement between experiment is achieved only when the full microscopic calculation including pairing and particle-number projection is utilized. In this respect, it is significant to recognize that the decrease in the neutron pairing gap in figure 5.6 occurs at a lower frequency than is found in most cases, and that the frequency region of this decrease is just that at which the unusually low

---

[7]Systematics of alignments and band crossing frequencies for the $^{176-180}$Os isotopes has been done by Garrett and Frauendorf[77]
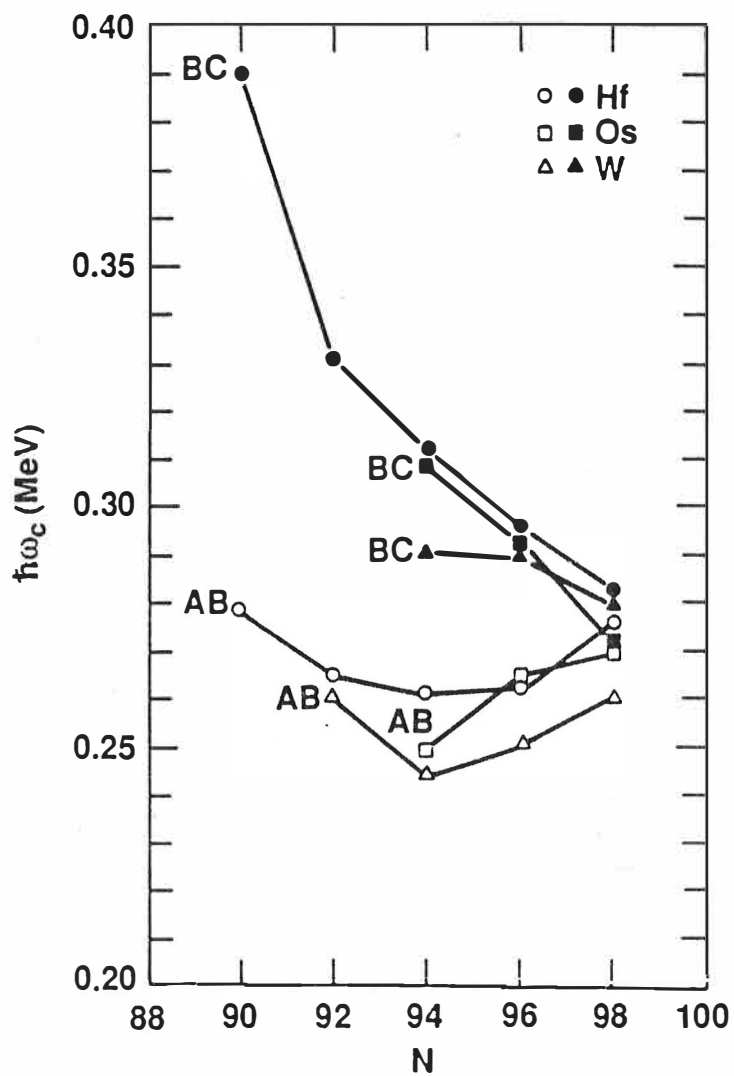
Figure 5.9: Systematics of the experimental AB and BC band crossing frequencies shown as a function of the neutron number N for the Hf, W and Os nuclei.
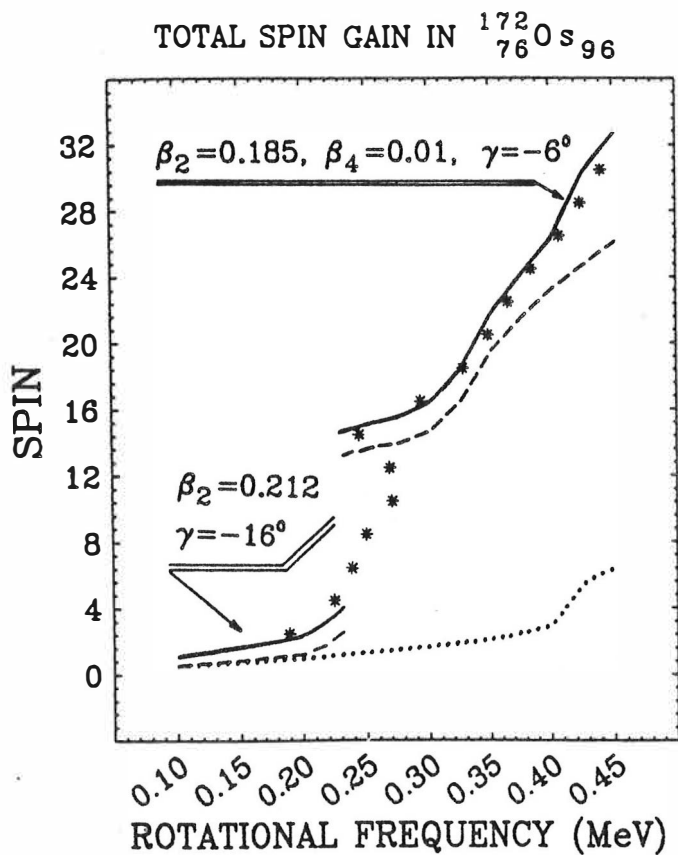
Figure 5.10: Comparison between the measured (asterisks) and calculated (full line) spin vs. rotational frequency. Dashed lines represent neutrons and the dotted lines show the contributions from the protons.

BC and AD band crossings take place.

5.3.2   The Q_t–Systematics

The picture given above is also supported by the comparison of the Q_t values of ^{158}Er and ^{172}Os: The values measured by Oshima et al.[79] and the results of this work are shown in figure 5.11. In some more strongly deformed nuclei, e.g. ^{232}Th[80], ^{162}Dy[81] and ^{160}Gd[82], it has been found that there can be a significant increase in the moment of inertia for higher members of the ground band, while at the same time there is no accompanying enhancement in the Q_t values. It has been suggested[80][81] that this

behaviour can be accounted for by reduction in the pairing correlations at the higher rotational frequencies (c.f. also the lower panel of figure 5.6), whereas the enhanced Q_t values must be associated with enhanced collectivity. This is the situation in ^{172}Os and in ^{158}Er, as can be seen from figure 5.11. In both nuclei the collectivity increases up to the backbending point (AB-crossing), after which a reduction in their Q_t values is seen. Theoretically this was combined to the reduction in quadrupole deformation as well as in triaxiality after the backbending (subsection 5.2.1 and figure 5.10). Hence, it is evident that the similarities in their alignment and crossing behaviours can be extended to their collective properties. Although the Q_t plots of these two nuclei are very similar the "double" stretching in ^{172}Os is visible and can be explained by the stronger as well as by the closer lying ground-BC interaction in this nucleus.

An opposite example is ^{174}Os, where the BC-crossing was supposed to be stronger than in ^{172}Os and the interaction strength was proposed to extend below the AB-crossing point. The Q_t values for the yrast sequence (filled circles) in ^{174}Os, measured by Gascon et al.[83], are shown in the lowest panel of figure 5.11. They concluded, by omitting the states 2^+ and 10^+, that the extracted Q_t's are essentially constant and fairly high up to spin 20^+, with a weighted average of 7.8 eb for the states 4^+ to 8^+ and 7.5 eb for the states 12^+ to 20^+. It may be fortuitous but it is interesting to note how nicely the Q_t values of the states 2^+ and 10^+ fit into our picture about the existence of two anomalies also in this nucleus. The "double" stretching is not so dramatic as in ^{172}Os but this, in fact, indicates stronger as well as wider frequency range interaction in this nucleus, in agreement with the predictions mentioned above. This is discussed in detail below.

The initial- and final states of a transition at the ground, $|g\rangle$, and Stockholm, $|s\rangle$, bandcrossing can be given as

$$|i\rangle = c_i^g|g\rangle + c_i^s|s\rangle$$

and

$$|f\rangle = c_f^s|s\rangle + c_f^g|g\rangle,$$

respectively. The behaviour of the Q_t in the crossing region can be illustrated by writing it as[8]

$$Q_t = c_i^g c_f^g \langle g|Q_{op}|g\rangle + c_i^s c_f^s \langle s|Q_{op}|s\rangle + c_i^s c_f^g \langle s|Q_{op}|g\rangle + c_i^g c_f^s \langle g|Q_{op}|s\rangle. \quad (5.1)$$

Here $c_{i,f}$ are the amplitudes of the $|g\rangle$- and $|s\rangle$ band components for the states $|i\rangle$ and $|f\rangle$ of the $E2$ transition. The mixed matrix elements of the

---

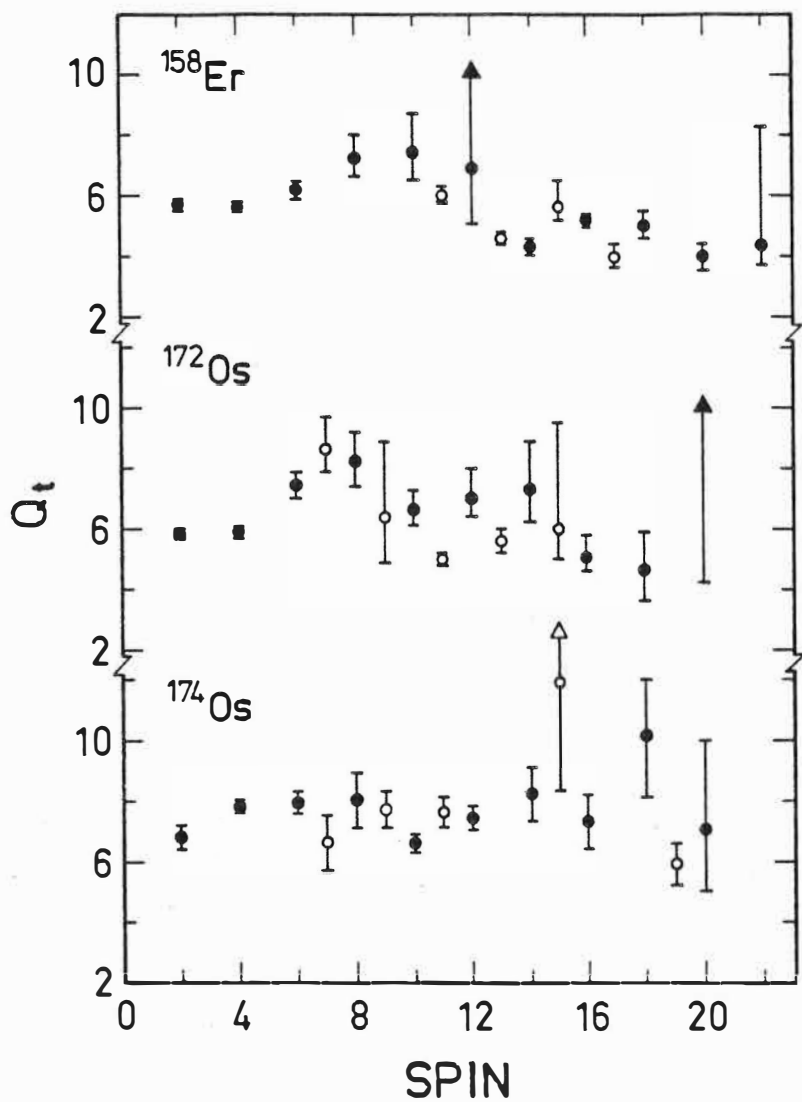[8]c.f. subsection 3.3.3 and eq.'s (3.23) and (3.24) there.

Figure 5.11: Transition quadrupole moments of yrast- (•) and odd-spin negative parity (○) states in ^{158}Er, in ^{172}Os and in ^{174}Os.

type $\langle s|E2|g\rangle$ are usually orders of magnitude smaller (c.f. $B(E2)$) than the collective ones, $\langle g|E2|g\rangle$ and $\langle s|E2|s\rangle$. In the vicinity of band crossing the terms in eq. (5.1) provide following contributions:

1 In the case of a sharp backbending (weak interaction or weakly mixed bands) the $c_i^s = c_f^g = 1$, $c_i^g = c_f^s = 0$ and, in the limiting case, the Q_t is reduced to the third term. A strong and a sudden reduction in Q_t-values is expected.

2 In the case of a vertical upbend (moderate interaction) the contribution to Q_t comes from the first three terms. Again, a reduction, but not so abrupt, in Q_t's is expected.

3 In the case of a gradual upbend (strong interaction/mixing) the first two terms are of importance only. A smooth change in Q_t's is expected.

In practice the terms in eq. (5.1) are mixed with different strengths over the crossing region. They are also strongly disturbed by the stretching as well as by the simultaneous crossings. However, some conclusions can be made: According to figure 5.11, followed by the "anomalous" stretching the Q_t values in both Os-isotopes decrease after spin 8^+. In ^{172}Os this corresponds to the frequency of $\hbar\omega = 0.24$ MeV and lies in the region of the first anomaly (see fig. 5.1). The "normal" stretching continues up to spin 14^+, after which the sudden drop takes place. It is interesting to note that these spin values, 10^+, 12^+ and 14^+, are the same found to be yrast in figure 5.8 before the AB-BC(AD) intersection point. The first drop represents preferably an intermediate, case **2**-type interaction (c.f the proposed BC-crossing), whereas the second one corresponds to the case **1**, a weakly interacting band crossing (AB-crossing), both being the properties supported by the spectroscopic studies. In ^{174}Os the BC-interaction starts much earlier; spin 8 in ^{174}Os corresponds to a frequency of $\hbar\omega \sim 0.20$ MeV. The decrease in Q_t after spin 8^+ is less than in ^{172}Os indicating the stronger interaction strength (c.f. case **3**). Also, this interaction smooths the AB-crossing region, supporting the "more simultaneous" AB/ground-BC crossing picture. These properties are consistent with the very wide frequency range alignment, $\hbar\omega = 0.2 - 0.4$ MeV, seen in this nucleus and discussed in the preceding subsection.

Below the backbending point the $c_i^g = c_f^g = 1$ and $c_i^s = c_f^s = 0$ and the first term in eq. (5.1) is dominating whereas the second term with $c_i^g = c_f^g = 0$ and $c_i^s = c_f^s = 1$ dominates above the backbending. The "theoretical" Q_t's with the parameter values given in figure 5.10, can be calculated according to eq. (3.33). Below the backbending region (term $\langle g|E2|g\rangle$) one gets

$Q_t = 6.1$ eb for the spins 2^+ and 4^+ and above the backbending (term $\langle s|E2|s \rangle$) $Q_t = 5.0$ eb for the spins $\geq 16^+$. These values are in accordance with the experimental values of $Q_t = 5.9$ eb for 4^+ and $Q_t = 5.0$ eb for 16^+ state of ^{172}Os given in table 4.5.

The Q_t's for odd-spin, negative-parity states in nuclei ^{158}Er, ^{172}Os and ^{174}Os are also shown in figure 5.11 (open circles). Generally, the "trend" of the negative-parity bands in all these nuclei follows to those of the yrast states, indicating their similar collective character. However, compared to the positive-parity states of the ground band in ^{172}Os the Q_t's of the negative-parity states are slightly lower, closer to the values of the s band, a phenomenon probably caused by their larger aligned particle contribution to the total spin. This assumption is also supported by the lifetimes of the negative-parity states, see table 4.6, which are longer compared to those of the ground band. On the other hand, the $B(E1)/B(E1)_{s.p.}$ ratios are far away from the single-particle ones. This is a common feature for all feeding transitions in ^{172}Os, measured and modelled, supporting an existence of the rotation aligned states also in these preyrast bands, γ proposed to be $\sim -16^0$ to -20^0 in subsection 5.2.1. However, it is interesting to note, that in potential energy landscape plots for the negative- as well as for the positive parity states in figure 5.3 it was also predicted a minimum for deformation aligned states at $\gamma \sim -120^0$. These two classes of states rarely mix but are, indeed, seen in heavier Os-isotopes, namely in $^{180-184}$Os[84][85][86], appearing as high K-isomers found in these nuclei. The existence of K-isomers as yrast or near yrast states is especially pronounced for nuclei with $102 \leq N \leq 108$ and $70 \leq Z \leq 76$, which is due to the occurrence of many high-Ω single particle orbitals near the Fermi surface for both protons and neutrons. As was mentioned, this is not seen in ^{172}Os.

Chapter 6

Summary and Conclusions

High spin data for the two osmium nuclei, ^{172}Os and ^{173}Os, obtained by utilizing heavy ion reaction and advanced multi-detector arrays are presented in this work. In the $\gamma - \gamma$ coincidence experiment a 4π array of 53 NaI- and 19 Compton-suppressed Ge-units was used. High spin state data in the yrast band of ^{172}Os were extended from spin $I^\pi = 24^+$ up to the $I^\pi = 30^+$ state. In addition to this, four new side bands were deduced. A band belonging to the previously unknown nucleus ^{173}Os was also identified. Experimental Routhians, alignments and band-crossing frequencies were also extracted. Based on these results and systematics, it was proposed that the main contributions in ^{172}Os come from the lowest lying positive- (designated by A, B, C and D) and negative-parity (E and F) orbitals of the $i_{13/2}$ and $h_{9/2}$ neutron shells, respectively. In addition to the s band (AB-band) it was concluded that the negative-parity bands have two quasineutron configurations, with the $\alpha = 1$ band having the AE configuration and the $\alpha = 0$ band having the AF configuration. At a higher frequency these bands are crossed by a four quasineutron configuration with the aligned BC quasineutrons, giving the $\alpha = 1$ band the AEBC configuration and the $\alpha = 0$ band the AFBC configuration.

Total energy surfaces of the ^{172}Os for the four assigned parity-signature combinations as a function of spin were calculated. For this, the generalized Strutinsky approach with the deformed Woods-Saxon potential and its universal parameterization was used. The most important shape change in the interesting low spin anomaly regime corresponded to the switch to decreased triaxiality after the backbend and was supposed to be caused by the increasing alignment. The microscopic effects with the Hartree-Fock-Bogoliubov Cranking calculations and Woods-Saxon potential were also performed and both particle-number projection and the effects of pairing were examined.

93

Lifetime information from both the yrast sequence and the lowest side band of the nucleus ^{172}Os was collected. This was done by utilizing the ORNL recoil-distance apparatus and an array of seven detectors. Measurements at 20 different distances were made in coincidence mode. This allowed an advanced analyzing method with versatile gating possibilities. Extracted quadrupole moments were compared to the results of ^{174}Os and ^{158}Er in which, separately, similarities to the low- and high spin behaviour of ^{172}Os through the bandcrossing region can be observed.

Finally, a summary of the conclusions from the experimental and theoretical results is given:

- The nuclei considered possess rather "unusual" alignment properties resulting from their characteristic structure in terms of excited quasi-particles. This structure is dominated by strong interactions in the neutron quasiparticle crossings (AB, BC and AD) and by the fact that these appear very close in terms of rotational frequencies. The first "anomaly" in the yrast line has been interpreted in terms of these nearly degenerate crossings.

- The proton induced alignment could not be identified in the present study. Theoretical arguments have been given to indicate its possible onset at $\hbar\omega \sim 0.45$ MeV.

- Calculations suggest a strong reduction in the neutron pairing gap over the frequency range $\hbar\omega \sim 0.22 - 0.28$ MeV. Only an indirect conclusion about pairing reduction could be made, based on the comparison of the experimental and theoretical values of I vs. ω. However, it is deemed significant that this reduction in the neutron pairing gap occurs in the same region as does the unusually low BC band crossing.

- The ground state band of ^{172}Os exhibits centrifugal stretching. The transition quadrupole moment values support the close lying multi-crossing picture. Even the effect of the long range BC crossing as a "double-stretching" below the AB-backbending point was recocnized. This also lends support to the explanation given to the first "anomaly".

- The shrinking of the ^{172}Os after the bandcrossings, proposed to be caused by a reduction in both quadrupole deformation and in triaxiality, was experimentally indicated. This demonstrates that the gain in moment of inertia after the backbend originates entirely from the aligned two particle nature. This conclusion can be done although there is an obvious need for additional lifetime data at higher spins.

Bibliography

[1] R. Bengtsson and S. Frauendorf, Nucl. Phys. **A314** (1979) 27

[2] R. Bengtsson and S. Frauendorf, Nucl. Phys. **A327** (1979) 139

[3] J. L. Durell, G. D. Dracoulis, C. Fahlander and A. P. Byrne, Phys. Lett. **115B** (1982) 367

[4] J. C. Wells, N. R. Johnson, C. Baktash, I. Y. Lee, F. K. McGowan, M. N. Rao, L. L. Riedinger, V. Janzen, W. C. Ma, Shuxian Wen, Ze-Min Chen, P. B. Semmes, G. A. Leander and Y. S. Chen, Phys. Rev. **C36** (1987) 431

[5] M. Oshima, N. R. Johnson, F. K. McGowan, C. Baktash, I. Y. Lee, Y. Schutz, R. V. Ribas and J. C. Wells, Phys. Rev. **C33** (1986) 1988

[6] M. P. Fewell, N. R. Johnson, F. K. McGowan, J. S. Hattula, I. Y. Lee, C. Baktash, Y. Schutz, J. C. Wells, L. L. Riedinger, M. W. Guidry and S. C. Pancholi, Phys. Rev. **C37** (1988) 101

[7] G. D. Dracoulis, A. E. Stuchbery, A. P. Byrne, A. R. Poletti, S. J. Poletti, J. Gerl and R. A. Bark, Nucl. Phys. **G12** (1986) 97

[8] R. Bengtsson, J.-y. Zhang, J. H. Hamilton and L. K. Peker, Nucl. Phys. **G12** (1986) 223

[9] M. N. Rao, N. R. Johnson, F. K. McGowan, I. Y. Lee, C. Baktash, M. Oshima, J. W. McConnell, J. C. Wells, A. Larabee, L. L. Riedinger, R. Bengtsson, Z. Xing, Y. S. Chen, P. B. Semmes and G. A. Leander, Phys. Rev. Lett. **57** (1986) 667

[10] G. D. Dracoulis, R. A. Bark, A. E. Stuchbery, A. P. Byrne, A. M. Baxter and F. Riess, Nucl. Phys. **A486**, (1988) 414

[11] H.F. Arciszewski, H.J. Aarts, R. Kamermans, C.J. Van Der Poel, R. Holzmann, M.A. Van Hove, J. Vernier, M. Huyse, G. Lhersonneau, R.V. Janssens and M.J.A. de Voigt, Nucl. Phys. **A401** (1983) 531

95

[12] S. T. Hsieh, M. M. King Yen and T. T. S. Kuo, J. Phys. **G14** (1988) L31

[13] S.M. Harris, Phys. Rev. **138** (1965) B509

[14] M.A.J. Mariscotti, G. Scharff-Goldhaber and B. Buck, Phys. Rev. **178** (1969) 1864

[15] R. Bengtsson, S. Frauendorf and F.R. May, Atomic Data and Nuclear Data Tables **35** (1986) 15

[16] S.G. Nilsson, Mat. Fys. Medd. Dan. Vid. Selsk. **29** (1955)

[17] S.G. Nilsson, C.F. Tsang, A. Sobiczewski, Z. Szymanski, S. Wycech, C. Gustafson, I.-L. Lamm, P. Möller and B. Nilsson, Nucl. Phys. **A131** (1969) 1

[18] G. Andersson, S.E. Larsson, G. Leander, P. Möller, S.G. Nilsson, I. Ragnarsson, S. Åberg, R. Bengtsson, J. Dudek, B. Nerlo-Pomorska, K. Pomorski and Z. Szymanski, Nucl. Phys. **A268** (1976)

[19] K. Neergård, H. Toki, M. Ploszajczak and A. Faessler, Nucl. Phys. **A287** (1977)

[20] R. Bengtsson, J. Dudek, W. Nazarewicz and P. Olanders, Phys. Scripta **39** (1989)

[21] J. Dudek and T. Werner, J. Phys. **G4** (1978)

[22] J. Dudek, A. Majhofer, J. Skalski, T. Werner, S. Cwiok and W. Nazarewicz, J. Phys. **G5** (1979)

[23] J. Dudek, Z. Szymanski and T. Werner, Phys. Rev. **C23** (1981)

[24] S. Cwiok, J. Dudek, W. Nazarewicz, J. Skalski and T. Werner, Comp. Phys. Comm. **46** (1987) 379

[25] M.J.A. de Voigt, J. Dudek and Z. Szymanski, Rev. Mod. Phys. **55** (1983) 949

[26] P. Ring and P. Schuck, *The Nuclear Many Body Problem*, New York 1980, Springer Verlag

[27] N.N. Bogolyubov, JETP **7** (1958)

[28] J.G. Valatin, Nuovo Cimento **7** (1958)

[29] A. Bohr, B. Mottelson and D. Pines, Phys. Rev. **110** (1958)

[30] J. Bardeen, L.N. Cooper and J.R. Schieffer, Phys. Rev. **108** (1957)

[31] J.-y. Zhang, L.L. Riedinger and J.D. Garrett, Phys. Rev. **C28** (1983)

[32] J.D. Garrett, Nucl. Phys. **A409** (1983)

[33] J.D. Garrett, Phys. Scripta **T5** (1983) 21

[34] P.J. Nolan and J.F. Sharpey-Schafer, Rep. Prog. Phys. **42** (1979) 1

[35] T.K. Alexander and J.S. Forster, *Advances in Nuclear Physics*, vol.10, ed. by M. Baranger and E. Vogt, Plenum Press, New York (1978)

[36] E.K. Warburton, J.W. Olness and A.R. Poletti, Phys. Rev. **160** (1967) 938

[37] K.W. Jones, A.Z. Schwarzschild, E.K. Warburton and D.B. Fossan, Phys. Rev. **178** (1969) 1773

[38] N. R. Johnson, R. J. Sturm, E. Eichler, M. W. Guidry, G. D. O'Kelley, R. O. Saycr, D. C. Hensley, N. C. Singhal and J. H. Hamilton, Phys. Rev. **12C** (1975) 1927

[39] D. B. Fossan and E. K. Warburton, *Nuclear Spectroscopy and Reactions*, 40C, ed. Joseph Cerny, Academic Press, New York and London (1974)

[40] T. Yamazaki, Nucl. Data Tables **3** (1967) 1

[41] R. J. Sturm and M. W. Guidry, Nucl. Instr. Meth. **138** (1976) 345

[42] A. Abragam and R.V. Pound, Phys. Rev. **92** (1953) 943

[43] L. C. Northcliffe and R. F. Schilling, Nucl. Data Tables **A7** (1970) 233

[44] H. H. Andersen and J. F. Ziegler, *Hydrogen Stopping Powers and Ranges in all Elements*, Pergamon, New York (1977)

[45] J. F. Ziegler, *Stopping Cross-Sections for Energetic Ions in all Elements*, Pergamon, New York (1980)

[46] H. Bateman, Proc. Cambridge Phil. Soc. **15** (1910) 423

[47] R. Evans, *The Atomic Nucleus*, McGraw-Hill, New York (1955)

[48] J. C. Wells, M. P. Fewell and N. R. Johnson, *LIFETIME: A Computer Program for Analyzing Doppler Shift Recoil Distance Nuclear Lifetime Data*, ORNL/TM9105 (1985)

[49] H. Emling, private communication

[50] F. James and M. Roos, Comput. Phys. Commun. **10** (1975) 343

[51] A. Bohr and B. Mottelson, *Nuclear Structure*, vol. 1, W.A. Benjamin Inc., New York, Amsterdam (1969)

[52] A. de Shalit and H. Feshbach, *Theoretical Nuclear Physics*, vol. 1: *Nuclear Structure*, John Wiley & Sons, Inc., New York, London, Sydney, Toronto (1974)

[53] A. de Shalit and J. Talmi, *Nuclear Shell Theory*, Academic Press, New York, London (1963)

[54] K.E.G. Löbner, M. Vetter and V. Hönig, Nuclear Data Tables **7** (1970) 495

[55] A. Bohr and B. Mottelson, *Nuclear Structure*, vol. 2, W.A. Benjamin Inc., New York, Amsterdam (1975)

[56] D.L. Hill and J.A. Wheeler, Phys. Rev. **89** (1953) 1102

[57] F.K. McGowan and P.H. Stelson, *Nuclear Spectroscopy and Reactions*, part C, ed. Joseph Cerny, Academic Press, New York London (1974)

[58] V.F. Weisskopf, Phys. Rev. **83** (1951) 1073

[59] Reaction Code Julian-PACE, unpublished

[60] M. Jääskeläinen, D.G. Sarantites, R. Woodward, F.A. Dilmanian, R. Jääskeläinen, M.L. Halbert, D.C. Hensley and J.H. Barker, Nucl. Instr. Meth. **204** (1983) 385

[61] K.S. Krane, R.M. Steffen and R.M. Wheeler, Nuclear Data Tables **11** (1973) 351

[62] N.R. Johnson, J.W. Johnson. I.Y. Lee, J.E. Weidley, D.R. Haenni and J.R. Tarrant, ORNL Physics Division Progress Report (Nov. 1981) ORNL-5787, p. 147

[63] J.C. Wells, N.R. Johnson, J. Hattula, M.P. Fewell, D.R. Haenni, I.Y. Lee, F.K. McGowan, J.W. Johnson and L.L. Riedinger, Phys. Rev. **C30** (1984) 1532

[64] T.K. Alexander and A. Bell, Nucl. Inst. Meth. **81** (1970) 22

[65] W. Walus, N. Roy, S. Jonsson, L. Carlén, H. Ryde, G.B. Hagemann, B. Herskind, J.D. Garrett, Y.S. Chen, J. Almberger and G. Leander, Physica Scripta **24** (1981) 324

[66] R. Chapman, J.C. Lisle, J.N. Mo, E. Paul, A. Simcock, J.C. Willmott, J.R. Leslie, H.G. Price, P.M. Walker, J.C. Bacelar, J.D. Garrett, G.B. Hagemann, B. Herskind, A. Holm and P.J. Nolan, Phys. Rev. Lett. **51** (1983) 2265

[67] J. Recht, Y.K. Agarwal, K.P. Blume, M. Guttormsen, H. Hubel, H. Kluge, K.H. Maier, A. Maj, N. Ray, D.J. Decman, J. Dudek and W. Nazarewicz, Nucl. Phys. **A440** (1985) 366

[68] V.M. Strutinsky, Nucl. Phys. **A95** (1967) 420

[69] J. Dudek, Proc. Winter Meeting on Nuclear Physics, Bormio, Italy, ed. I. Iori, Milan 1987

[70] M.A. Riley, J. Simpson, J.F. Sharpey-Schafer, J.R. Cresswell, H.W. Cranmer-Gordon, P.D. Forsyth, D. Howe, A.H. Nelson, P.J. Nolan, P.J. Smith, N.J. Ward, J.C. Lisle, E. Paul and P.M. Walker, Nucl. Phys. **A486** (1988) 456

[71] J. Simpson, P.A. Butler, P.D. Forsyth, J.F. Sharpey-Schafer, J.D. Garrett, G.B. Hagemann, B. Herskind and L.P. Ekström, J. Phys. G **10** (1984) 383

[72] J.Simpson, M.A. Riley, J.R. Cresswell, D.V. Elenkov, P.D. Forsyth, G.B. Hagemann, D. Howe, B.M. Nyako, S. Ogaza, J.C. Lisle and J.F. Sharpey-Schafer, J. Phys. G **13** (1987) 847

[73] S. Jonsson, N. Roy, H. Ryde, W. Walus, J. Kownacki, J.D. Garrett, G.B. Hagemann, B. Herskind, R. Bengtsson and S. Åberg, Nucl. Phys. **A449** (1986) 537

[74] J.D. Garrett, Nucl. Phys. **A421** (1984) 3130

[75] R. Bengtsson, Proc. International Conference on Contemporary Topics Nuclear Structure Physics, Cocoyoc 1988, Mexico, ed. R.F. Casten, A. Frank, M. Moshinsky and S. Pittel, World Scientific, Singapore, p.317

[76] M.J.A. de Voigt, private communication

[77] J.D. Garrett and S. Frauendorf, Phys. Lett. **108B** (1982) 77

[78] J. Dudek, T. Werner and L.L. Riedinger, Phys. Lett. **B211** (1988) 252

[79] M. Oshima, N.R. Johnson, F.K. McGowan, C. Baktash, I.Y. Lee, Y. Schutz, R.V Ribas and J.C. Wells, Phys. Rev. **C33** (1986) 1988

[80] M.W. Guidry, P.A. Butler, P. Colombani, I.Y. Lee, D. Ward, R.M. Diamond, F.S. Stephen, E. Eichler, N.R. Johnson and R. Sturm, Nucl. Phys. **A266** (1976) 228

[81] M.W. Guidry, I.Y. Lee, N.R. Johnson, P.A. Butler, D. Cline, P. Colombani, R.M. Diamond and F.S. Stephen, Phys. Rev. **C20** (1979) 1814

[82] I.Y. Lee, N.R. Johnson, T.T. Sugihara, M.W. Guidry, E.L. Robinson, R.M. Diamond and F.S. Stephen, ORNL Physics Division Progress report (Nov. 1981) ORNL-5787, p. 84

[83] J. Gascon, F. Banville, P. Taras, D. Ward, T.K. Alexander, H.R. Andrews, G.C. Ball, D. Horn, D.C. Radford, J.C. Waddington and A. Christie, TASCC progress report 1987

[84] R.M. Lieder, A. Neskakis, J. Skalski, G. Sletten, J.D. Garrett and J. Dudek, Nucl. Phys. **A476** (1988) 545

[85] P. Chowdhury, B. Fabricius, C. Christensen, F. Azgui, S. Björnholm, J. Borggreen, A. Holm, J. Pedersen, G. Sletten, M.A. Bentley, D. Howe, A.R. Mokhtar, J.D. Morrison, J.F. Sharpey-Schafer, P.M. Walker and R.M. Lieder, Nucl. Phys. **A485** (1988) 136

[86] A. Alderson, M. Bentley, C. Broude, A. Bruce, E. Dafni, P. Fallon, G. Goldring, M. Hass, J. Nyberg, J. Roberts, J. Sharpey-Schafer, G. Sletten and P. Twin, Phys. Lett. **B228** 463

[87] K.S. Krane, Nucl. Instr. Meth. **98** (1972) 205

[88] F. James, *Monte Carlo for Particle Physicists, Methods in Subnuclear Physics*, Vol. IV, part 3, ed. M. Nicolic, Gordon and Breach, New York, London and Paris (1970)

[89] F. James, Rep. Prog. Phys.**43** (1980) 1145

[90] J.A. Nelder and R. Mead, Comput. J. **7** (1965) 308

[91] R. Fletcher, Comput. J. **13** (1970) 317

Appendix A

Transformation into the Rotating Coordinate Frame. Classical Treatment

The two coordinate systems, laboratory and body-fixed, are related to each other by the transformation

$$
\begin{aligned}
x_1' &= x_1 \\
x_2' &= x_2 \cos \omega t + x_3 \sin \omega t \\
x_3' &= -x_2 \sin \omega t + x_3 \cos \omega t.
\end{aligned}
\tag{A.1}
$$

The primed coordinates (x_i') refer to the rotating coordinate system, X', and the others (x_i) to the laboratory coordinate system, X, the "1"-axis being the rotational axis.

The kinetig energy of a particle with mass m is

$$
\begin{aligned}
T &= \frac{m}{2}(\dot{x}_1^2 + \dot{x}_2^2 + \dot{x}_3^2) = \\
&= \frac{m}{2}[\dot{x}_1'^2 + \dot{x}_2'^2 + \dot{x}_3'^2 - 2\omega(\dot{x}_2' x_3' - \dot{x}_3' x_2') + \omega^2(\dot{x}_2'^2 + \dot{x}_3'^2)].
\end{aligned}
\tag{A.2}
$$

The Lagrange function for a particle moving in a potential $V(x_1', x_2', x_3')$, fixed in X', has the form

$$
L = T - V(x_1', x_2', x_3').
\tag{A.3}
$$

The Lagrange equations

$$
\frac{d}{dt}\frac{\partial L}{\partial \dot{x}_i'} - \frac{\partial L}{\partial x_i'} = 0
\tag{A.4}
$$

can be written out as

$$
\begin{aligned}
m\ddot{x}_1' &= -\frac{\partial V}{\partial x_1'} \\
m\ddot{x}_2' &= -\frac{\partial V}{\partial x_2'} + 2m\omega\dot{x}_3' + m\omega^2 x_2' \\
m\ddot{x}_3' &= -\frac{\partial V}{\partial x_3'} - 2m\omega\dot{x}_2' + m\omega^2 x_3'.
\end{aligned}
\tag{A.5}
$$

By defining $\bar{\omega} = \omega\hat{x}_1'$, where $\hat{x}_1'$ is the unit vector, equations (A.5) can be written in the condensed form

$$
m\ddot{\mathbf{r}}' = -\nabla V - 2m\bar{\omega} \times \dot{\mathbf{r}}' - m\bar{\omega} \times (\bar{\omega} \times \mathbf{r}'),
\tag{A.6}
$$

where the Coriolis ($2m\bar{\omega} \times \dot{\mathbf{r}}'$) and centrifugal ($m\bar{\omega} \times (\bar{\omega} \times \mathbf{r}')$) terms can be recognized.

The canonical momenta, defined by $p_i' = \partial L/\partial \dot{x}_i'$, now give

$$
\begin{aligned}
p_1'^2 &= m^2 \dot{x}_1'^2 \\
p_2'^2 &= m^2 \dot{x}_2'^2 - 2m^2\omega\dot{x}_2' x_3' + m^2\omega^2 x_3'^2 \\
p_3'^2 &= m^2 \dot{x}_3'^2 + 2m^2\omega\dot{x}_3' x_2' + m^2\omega^2 x_2'^2.
\end{aligned}
\tag{A.7}
$$

Then the Hamiltonian, H', in X' becomes

$$
H'(x_i', p_i') = \sum_i \dot{x}_i' \frac{\partial L}{\partial \dot{x}_i'} - L = \sum_i \frac{1}{2m} p_i'^2 + V(x_i') - \omega(x_2' p_3' - x_3' p_2').
\tag{A.8}
$$

At $\omega = 0$, this is the normal non-rotating Hamiltonian, expressed in the body-fixed coordinates:

$$
H_0(x_i', p_i') = \sum_i \frac{1}{2m} p_i'^2 + V(x_i').
\tag{A.9}
$$

The last term in (A.8) is the "1" component of the angular momentum $\mathbf{L}' = \mathbf{r}' \times \mathbf{p}'$

$$
\omega L_1' = \omega(x_2' p_3' - x_3' p_2').
\tag{A.10}
$$

Hence,

$$
H'(x_i', p_i') = H_0(x_i', p_i') - \omega L_1'.
\tag{A.11}
$$

Finally, by taking the nucleonic spin, $\mathbf{s}$, into consideration we must replace L_1' with $J_1' = L_1' + S_1'$. This gives us the equation

$$
H' = H_0 - \omega J_1',
\tag{A.12}
$$

which is the well known "cranking Hamiltonian".

Appendix B

The Woods-Saxon Potential

The central part of the Woods-Saxon potential was given in subsection 2.2.2 by eq. (2.33):

$$V_c(\mathbf{r}, \hat{\beta}) = \frac{V_0}{1 + exp[\mathbf{dist}(\mathbf{r}, \hat{\beta}, R_s)/a]}, \tag{B.1}$$

with the term $\mathbf{dist}(\mathbf{r}, \hat{\beta}, R_s)$ representing the distance from a point $\mathbf{r}$ to the nuclear surface. For axial shapes the nuclear surface R_s (c.f. eq. (3.34)) is defined by

$$R_s(t, \hat{\beta}) = C(\hat{\beta})R_0[1 + \sum_{\lambda \geq 2} \beta_\lambda Y_{\lambda 0}(t)], \tag{B.2}$$

where $t = \cos\theta$, the $\hat{\beta}$ representing the whole set of deformation parameters ($\lambda = 2, 3, 4, \cdots$). Very often only axially symmetric quadrupole (β_2) and hexadecapole (β_4) deformations are considered. The diffuseness parameter a is supposed to be constant, independent on the shape of the surface. This is because of the short-range characteristics of the nucleon-nucleon force. The R_0 is the radius of the spherical nucleus of identical volume and is assumed to follow the usual parameterization $R_0 = r_0 A^{1/3}$. Finally, V_0 represents the depth of the central potential at $r = 0$ and is parameterized as $V = V_0[1 \pm \kappa(N - Z)/(N + Z)]$ with the plus sign for protons and the minus sign for neutrons.

Also, the spin-orbit term has to be taken into account. It does not resemble the simple $\mathbf{l} \cdot \mathbf{s}$ term in the Nilsson model. However, Bohr and Mottelsson[51] (p.218) showed that it should be replaced with $\nabla V \times \mathbf{p} \cdot \mathbf{s}$. This leads to the following parametrization[24]:

$$V_{so}(\mathbf{r}, \hat{\beta}) = -\lambda_{so}(\frac{1}{2mc})^2 \nabla V_c^{so} \times \mathbf{p} \cdot \sigma, \tag{B.3}$$

where the form of the central potential V_c equals V_c^{so}, the superscript "so" indicating, that the parameters R_s and a in (B.1) must be replaced with the R_{so} and a_{so}, respectively. This origins from the fact that the spin-orbit potential may fluctuate with the filling of the shell, while the central potential is expected to change in a smooth monotonic way with increasing particle number. Also, m is the nucleonic mass as well as $\sigma = 2\mathbf{s}$ and $\mathbf{p}$ are the nucleonic spin and linear momentum, respectively.

The effective potential for protons includes also the Coulomb term V_{coul}. It is assumed to be that of the nuclear charge equal to $(Z-1)e$ and uniformly distributed inside the surface R_s of (B.2). Its computation is explained e.g. in reference[24]. In the systematic comparison between the Nilsson and Woods-Saxon deformed shell model potentials Bengtsson et al.[20] concluded that *"the proton single-particle orbitals show small but systematic differences both in the rare-earth and actinide region. The origin of these differencies can be traced back to the Coulomb interaction, which is not explicitly considered in the Nilsson potential".*

Finally, we summarize:

The Woods-Saxon potential in its general form is expressed as

$$V_{ws} = V_c(\mathbf{r}, \hat{\beta}) + V_{so}(\mathbf{r}, \hat{\beta}) + V_{coul}(\mathbf{r}, \hat{\beta}), \qquad (B.4)$$

with $V_c(\mathbf{r}, \hat{\beta})$ given by (B.1) and $V_{so}(\mathbf{r}, \hat{\beta})$. The shape parameterization is determined by the eq. (B.2) i.e. the $\beta_2, \beta_3, \beta_4, \cdots$ fixes the shape. To determine the Woods-Saxon potential 12 parameters should be given. For neutrons these are:

V_0 — depth parameter of the central potential,

r_0 — radius parameter of the central potential,

a — diffuseness parameter of the central potential,

λ_{so} — strength of the spin-orbit potential,

r_{so} — radius parameter of the spin-orbit potential,

a_{so} — diffuseness parameter of the spin-orbit potential,

and a similar set of parameters for the protons.

Appendix C

Subroutines in LIFETIME

The five most important subroutines in the analyzing program LIFETIME are MASTER, CORRECT, ANGDIS, VELCOMP and MINUIT:

MASTER The subroutine MASTER calculates the population of each level at a given time in terms of the initial populations of the levels and of the transition rates. It uses Bateman's equations considered in subsection 3.3.1. For a given set of initial conditions $P_i(0)$ the system of equations (3.21) can be solved analytically by making use of certain recursion relationships. We write equation (3.22) in the form

$$P_i(t) = \sum_{j=i+1}^{N} a_{ij}P_j(t) + b_i e^{-\Gamma_i t}. \qquad (C.1)$$

Here, $a_{ij} = \lambda_{ji}/(\Gamma_i - \Gamma_j)$, when $j = i+1$, and $a_{ij} = (\lambda_{ji} - \sum_{k=i+1}^{j-1} \lambda_{jk}a_{ik})/(\Gamma_i - \Gamma_j)$, when $j > i + 1$. Further, b_i is defined as $b_i = P_i(0) - \sum_{j=i+1}^{N} a_{ij}P_j(0)$. The assumptions for λ are: $\lambda_{ij} \geq 0$ if $i > j$ and $\lambda_{ij} = 0$ if $i \leq j$. Also, $\Gamma_i = \sum_{j=1}^{i-1} \lambda_{ij} \neq \Gamma_j$ if $i \neq j$.

The intensities of the shifted and unshifted components (S and U, respectively) of a transition from level i to level j are calculated by the expressions

$$S_{ij}(T) = \lambda_{ij} \int_0^T P_i(t)dt = \lambda_{ij}w_i(T), \qquad (C.2)$$

$$U_{ij}(T) = \lambda_{ij} \int_T^{\infty} P_i(t)dt = \lambda_{ij}v_i(T), \qquad (C.3)$$

where the definitions for w and v are

$$w_i(T) = \sum_{j=i+1}^{N} a_{ij}w_j(T) + \frac{b_i}{\Gamma_i}(1 - e^{-\Gamma_i T}),$$

and
$$v_i(T) = \sum_{j=i+1}^{N} a_{ij} v_j(T) + \frac{b_i}{\Gamma_i} e^{-\Gamma_i T}.$$
The total intensity I_i from the level i is given by $I_i = P_N(0)$, when $i = N$, or $I_i = P_i(0) + \sum_{j=i+1}^{N} \lambda_{ji} I_j / \Gamma_j$, when $i < N$.

The time independent coefficients a_{ij}, b_i and the total intensity I_i are calculated once and the populations $P_i(T)$, $S_{ij}(T)$ and $U_{ij}(T)$ are calculated for each flight time in turn.

CORRECT This subroutine calculates the corrections mentioned in section 3.2.

For the positional correction it integrates the eq. (3.13) along the flight path. The integral over the volyme of a coaxial semiconductor detector, using the method of K. S. Krane[87], is calculated by
$$J_k(E_\gamma) = \int P_k(\cos\theta)(1 - exp[-\mu(E_\gamma)X(\theta)])\sin\theta d\theta. \qquad (C.4)$$
There θ is the angle between a γ-ray and the detector axis, P_k is a Legendre polynomial, $\mu(E_\gamma)$ is the absorption coefficient of a γ-ray of energy E_γ in germanium and $X(\theta)$ is the path length through the detector at an angle θ. So J_0 is proportional to the absolute detector efficiency, J_1 gives the average $\cos\theta$, which is needed in calculating the recoil velocity and J_2/J_0 and J_4/J_0 are the solid angle correction factors for the angular distribution coefficients A_2 and A_4 in the eq. (3.17).

The integration limits can be seen from figure C.1 and are given by
$$\theta_1 = arctan[R_i/(D + L)]$$
$$\theta_2 = arctan(R_i/D)$$
$$\theta_3 = arctan[R_o/(D + L)]$$
$$\theta_4 = arctan(R_o/D).$$
The limits for the path lengths are obtained from figure C.1 in the same way.

For the velocity dependent integration the subroutine makes the relativistic angular transformation eq. (3.15). Alternatively, eq. (3.15) can be said by $cos\theta = (cos\theta_{CM} + \beta)/(1 + \beta\cos\theta_{CM})$. Now, (C.4) is
$$J_k(E_\gamma) = \sum_{n=1}^{3} \int_{\theta_{CM}(\theta_n)}^{\theta_{CM}(\theta_{n+1})} P_k(\cos\theta_{CM})[1 - exp(-\mu(E_\gamma)X(\theta(\theta_{CM})))]\sin\theta_{CM} d\theta_{CM}.$$
All the integrations are made using Simpson's rule, in which the even terms are doubled and the first and last term is halved. The number of terms may be changed at the user's option.
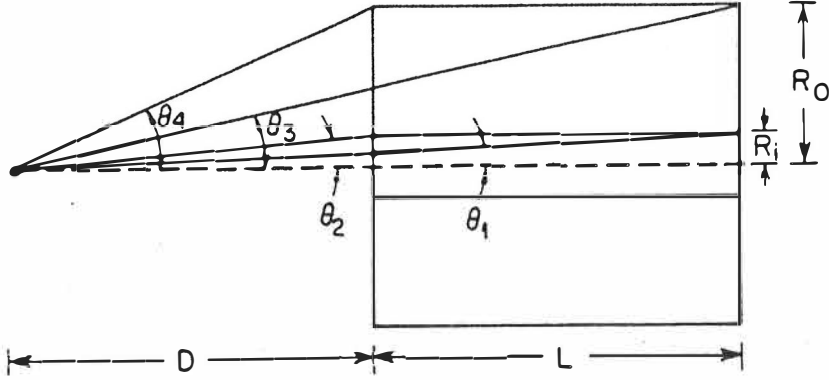
Figure C.1: Cross section of a Ge-detector for integration over the detector volume. R_o and R_i are the outer and inner radius of the detector, respectively. L is the detector length and D is the target-detector distance. The angles give the integration limits considered in the text.

For the hyperfine attenuation the subroutine uses the Abragam-Pound formalism according to eq. (3.18). The lineshape corrections are made as mentioned in subsection 3.2.4.

ANGDIS The angular distribution coefficients A_2 and A_4 are calculated starting from the completely aligned state with spin $J = 50$. It then de-excites into a lower state through a stretched E2-transition. If the spin change is less than two it assumes a pure E1 multipolarity. In the alculations the formalism of Yamazaki[40] is used.

In addition to this, ANGDIS calculates the reference values for the solid angle and alignment corrections. The reference solid angle is chosen for the nucleus at the target position. The reference angular distribution is that corresponding to the starting values of $A_2 = 0.368$ and of $A_4 = -0.112$. So, the distribution is $W = 1 + 0.368 P_2(1) - 0.112 P_4(1) = 1.256$.

VELCOMP From the centroids of the shifted and unshifted peaks the recoil velocities are calculated by the subroutine VELCOMP. If the angular distribution is omitted, the emission probability of a γ-ray at a time t is simply $\lambda P(t)$. Further, if the absorption probability of the detector is $p(\theta, t)$, according to eq. (3.9), one gets the quantity β as

$$\beta = \left(\frac{E_\gamma - E_\gamma^0}{E_\gamma^0}\right) \frac{\int_0^T \lambda P(t)(\int_0^{\phi(t)} p(\theta, t) \sin \theta \, d\theta) dt}{\int_0^T \lambda P(t)(\int_0^{\phi(t)} \cos \theta \, p(\theta, t) \sin \theta \, d\theta) dt}.$$

The integrations over θ correspond to the case J_1 in eq. (C.4). The integrations over t are calculated again using Simpson's rule.

MINUIT Subroutine FCN of the main program LIFETIME calculates the chi-square function analyzed by the subroutine MINUIT. The function is defined:

$$\chi^2 = \sum_{ijk} \frac{(U_{ij}^{exp}(T_k) - U_{ij}^{cal}(T_k))^2}{(\Delta U_{ij}(T_k))^2} + \frac{(S_{ij}^{exp}(T_k) - S_{ij}^{cal}(T_k))^2}{(\Delta S_{ij}(T_k))^2}, \qquad (C.5)$$

where U_{ij} and S_{ij} are the unshifted and shifted intensities between levels i and j, ΔU_{ij} and ΔS_{ij} are their uncertaintities and $T_k = D_k/v$ is the flight time of the "k'th" target-stopper distance (c.f. figure 3.1).

MINUIT minimizes the chi-square function (C.5). The theoretical intensities U_{ij}^{cal} and S_{ij}^{cal} are calculated by the subroutine MASTER using the equations (C.3) and (C.2), respectively. After the change of the unknown external parameters, given in the parameter file, into the internal parameters X, U_{ij}^{cal} 's and S_{ij}^{cal} 's can be presented in the form $F(X)$. The minimization is performed by evaluating $F(X)$ repeatedly at different points X, until some minimum value is attained.

MINUIT contains three minimization routines:

1) SEEK - a Monte Carlo searching subroutine. It can be used at the beginning of the fit to indicate a sensible starting point or to solve the problem of several minima. It performs a minimization of the FCN using the Monte Carlo techique described in the references [89] and [88].

2) SIMPLEX - a minimizing subroutine using a simplex method by Nelder and Mead[90] (A simplex is the smallest n-dimensional geometrical figure with n+1 corners, a triangle for n=2, a tetrahedron for n=3, etc.). It is "safe" and fast when far from the minimum. It does not compute the covariance matrix, sometimes called error matrix, but gives order of magnitude estimates of its diagonal elements (parameter errors).

3) MIGRAD - a minimization subroutine based on a variable metric method by Fletcher[91]. It is extremely fast near a minimum or in any nearly quadratic region but slower if the function is badly behaved. It performs a function minimization using a gradient calculated by a subroutine DERIVE. Contrary to the SIMPLEX, MIGRAD has the advantage of producing a full covariance matrix.

The parameter error analysis in MINUIT is produced by the subroutine MINOS. It finds the true errors by examining the behavior of the chi-square

function over the interval in question specified by the value of UP (default value of UP=1 corresponds to the one standard deviation confidence interval of 68%).

For more details about the subroutines above, see the references [50] and [48].